Stationary Fourier Transform Spectrometer
on a Silicon Nitride Photonic Integrated Circuit Platform

Stationaire fouriertransformatiespectrometer
op een fotonisch geïntegreerd circuit in siliciumnitride

Xiaomin Nie

Promotoren: prof. dr. ir. R. Baets, dr. ir. E. Ryckeboer
Proefschrift ingediend tot het behalen van de graad van
Doctor in de ingenieurswetenschappen: fotonica

UNIVERSITEIT
GENT

Vakgroep Informatietechnologie
Voorzitter: prof. dr. ir. B. Dhoedt
Faculteit Ingenieurswetenschappen en Architectuur
Academiejaar 2019 - 2020

ISBN 978-94-6355-321-6
NUR 950
Wettelijk depot: D/2019/10.500/129

Universiteit Gent
Faculteit Ingenieurswetenschappen en Architectuur
Vakgroep Informatietechnologie

Promotoren:
Prof. dr. ir. Roel Baets
Dr. ir. Eva Ryckeboer

Examencommissie:

Prof. dr. ir. Filip De Turck (voorzitter)	Universiteit Gent
Prof. dr. ir. Roel Baets (promotor)	Universiteit Gent
Dr. ir. Eva Ryckeboer (promotor)	Universiteit Gent
Prof. dr. ir. Wim Bogaerts (secretaris)	Universiteit Gent
Prof. dr. ir. Dries Van Thourhout	Universiteit Gent
Prof. dr. Dirk Poelman	Universiteit Gent
Prof. dr. ir. Jeremy Witzens	RWTH Aachen University
Dr. ir. Hilde Jan	Imec

Universiteit Gent
Faculteit Ingenieurswetenschappen en Architectuur

Vakgroep Informatietechnologie
Technologiepark Zwijnaarde 126 iGent, B-9050 Gent, België

Proefschrift tot het behalen van de graad van
Doctor in de ingenieurswetenschappen:
fotonica
Academiejaar 2019-2020

Acknowledgements

Starting the first line on this page is more difficult than I expected. When I put my fingers on the keyboard, a storm of memories and feelings arouses within me. I don't know which word is suitable to describe the journey of my Ph.D. life. Wonderful? Arduous? Joyful? I still remember the pride and curiosity when I first stepped into this journey. I would not deny the pressure and frustrations when, later on, there seem to be so many muddy puddles and bumpy patches. Neither would I say the fruits of success from all the hard work around the clock are not palatable. In the end, when I look back on the whole journey, I sincerely think this is an experience that will benefit my life. And most importantly, I want to express my heartfelt gratitude to everyone who has helped me in this 4.25-year-long journey.

First of all, I would like to thank my promoter, Roel Baets. He is the one who provides me the position, trusts me, and believes that I can do the job. When I get lost and don't know how to proceed, he spends time with me, discussing all the tough questions and guiding me towards the right track. All his great enthusiasm, patience and confidence encourage me to walk through the difficulties. Without his guidance, it is impossible for me to reach so far.

Secondly, I would like to thank my co-promoter, Eva Ryckeboer. She is always so kind and enthusiastic and ready to offer help whenever I get stuck. Especially in the early stage of my Ph.D., she gives me lots of detailed guidance that helps flatten the learning curve, which might otherwise be much steeper. Without her attentive help, it would take me much longer to dive into the field, to write my first IPKISS code, and to build the first measurement setup.

Many thanks to the Raman "community". While I am not working exactly on the Raman stuff, it's so nice that I have a "community"to go. The Raman

meetings play an important role throughout my Ph.D., and I am so glad that I can meet with and build connections to all the Raman members: Stephane, Nicolas, Haolan, Ali, Nina, Kristof, Yang, Zuyang, Ashim, Frederic, and Pieter. It's such a great experience not only to discuss all those bizarre problems but also to share the first-hand news of breakthroughs with them. Ph.D. students come and go, but I wish that our Raman "community"will last.

I also want to thank my office mates for making the working hours so colorful. Mahmoud, finally, I managed to run away before you :). I will miss the way you pronounce certain words and your "see you tomorrow". Alejandro, thank you for all the vibrations of the air, the nickname, and the joyful atmosphere. Soren, I have to tell you that you are really good at mimicking. It's so funny. Wish you all the best in America. Nicolas, Comment ça va? Still working around your white hole? Javad, you demonstrated how to be a gentleman. Good luck with your lasers. Haolan, you should come earlier so that I can bother you more with all kinds of questions. Irfan, good choice of moving out.

The joyful parts of the Ph.D. are to work together with many talented colleagues. It's my pleasure to be a teammate with them in Mircophotonics team, Megachip team and PIX4LIFE team. I would like to express my gratitude to all my teammates: Clemens Kruckel, Frederic Peyskens, Emmanuel Gooskens, Jeroen Goyvaerts, Khannan Rajendran, Hong Deng, Xiaoning Jia, Soren Dhoore, Alejanhdro Diaz Tormo, Alessio Lugnan, Sulakshna Kumari, Koen Alexander, Aditya Malik, Herbert D'herr and Andreas De Groote.

It is undoubtful that a good research group comes with excellent support staff. I sincerely appreciate their efforts in helping us solve all the technical issues. Many thanks to the technical supports in the measurement labs, Michael Vanslembrouck, Jasper Jans, and Peter Guns. Great thanks also go to the administrative staff, Ilse Van Royen, Kristien De Meulder, Ilse Meersman, Mike Van Puyenbroeck, and Bert Coryn. And also, I would like to thank the technical support in the cleanroom, Liesbet Van Landschoot, Steven Verstuyft and Muhammad Muneeb.

Special thanks go to all the Chinese friends in this group. They are more than colleagues and friends to me. I think it's not too exaggerated to say that we are more like a family. There are so many interesting and funny stories that I could write a separate book about them. Here, my gratitude goes to Haolan, Ang, Yufei, Yunpeng, Weiqiang, Chen, Ruijun, Bin, Yanlu,

Zhechao, Yuxin, Xiaoning, Yuting, Jing, Ye, Guanyun, Keqi, Qiangsheng, Yingchen, Jinghao, Qiang, Chonghuai, Zhenzhou, Mi, Yang, Naidi, Xiangfeng, Hong, Zuyang, Chupao, Zheng, Zhongtao and Chao. I wish everyone a bright career and a happy life!

My deepest gratitude goes to my girlfriend, Yixin. It's my greatest fortune to meet you, to walk close to you, to hold your hand, and to be able to spend the rest of my life with you. Without your supporting, comforting and encouraging, I could never manage this. Thank you for coming to my life and bringing me all the happiness. 借此机会, 我也要由衷地感谢我的父母。谢谢你们把我带到这个世界，谢谢你们抚养我长大，一直以来你们对我的支持与理解都是我前进的助力，我爱你们。

Gent, December 2019
Xiaomin Nie

Table of Contents

List of Figures

List of Tables

List of Acronyms

A

BOX	Buried Oxide

C

CMOS	Complementary Metal–Oxide–Semiconductor
CW	Continuous Wave
CVD	Chemical Vapor Deposition
CCD	Charge-Coupled Device

D

DFT	Discrete Fourier Transform
DBR	Distributed Bragg reflector

F

FTS	Fourier Transform Spectrometer

FSR	Free Spectral Range
FTIRs	Fourier Transform Infrared spectrometers
FFT	Fast Fourier Transform infrared spectrometers
FWHM	Full Width Half Maximum

G

GACDC	Grating-Assisted Contra-Directional Coupler
GC	Grating Coupler

H

HDP	High-Density Plasma

L

LPCVD	Low Pressure Chemical Vapour Deposition
LHS	Left Hand Side
LF	Lensed Fiber

M

MI	Michelson Interferometer
MEMs	Micro-Electro-Mechanical system
MZI	Mach-Zehnder Interferometer
MWIR	Mid-Wave Infrared
MMI	Multi-Mode Interference

MFD	Mode Field Diameter
MRR	Micro Ring Resonator
MPW	Multi-Project Wafer

N

NIR	Near-Infrared
NA	Numerical Aperture

O

OPD	Optical Path Difference
OSA	Optical Spectrum Analyzer

P

PIC	Photonics Integrated Circuit
PECVD	Plasma Enhanced Chemical Vapour Deposition
PML	Perfect Matching Layers
PC	Polarization Controller

R

RHS	Right Hand Side

S

SNR	Signal-to-Noise Ratio
SHS	Spatial Heterodyne Spectrometer
SWIFTs	Stationary Wave Integrated Fourier Transform spectrometer
SiN	Silicon Nitride
SOI	Silicon-On-Insulator
SWIR	Short-Wave Infrared
SSC	Spot Size Converters

T

TE	Transverse Electric
TM	Transverse Magnetic

Nederlandse samenvatting –Summary in Dutch–

Optische spectrometers staan al lang bekend als de onmisbare instrumenten op verschillende gebieden die optische spectrumanalyse vereisen. Vergeleken met de verschillende soorten moderne spectrometers biedt de Fourier transformatiespectrometer (FTS) belangrijke voordelen, [1–3]. Bijgevolg heeft de FTS vele toepassingen gevonden in de biologische wetenschappen, moleculaire wetenschappen, atmosferische wetenschappen en astronomie [4–7]. De conventionele FTS is echter een groot en duur toestel. Daarom is het interessant om een FTS die geïntegreerd is op een fotonische chip te onderzoeken, zeker gezien de toenemende vraag en groeiende voorkeur voor draagbare en robuuste FTS-apparaten. Om een chip-gebaseerde FTS te gebruiken in een geïntegreerd optisch spectroscopisch systeem, moeten we typisch ook andere chip-componenten ontwikkelen. In het geval dat we een op chip geïntegreerde FTS willen gebruiken als spectrale analyzer voor chip-gebaseerde Raman spectroscopie [8], moeten we de FTS combineren met een geïntegreerde filter voor het sterke excitatielicht (met een verzwakkingsfactor door de filter van ongeveer 100 dB). Deze filter is nodig om het sterke excitatielicht te verwijderen en zo de zwakke Raman signalen te onthullen. Bovendien is het meestal nodig dat de spectrometer, voor een nauwkeurige spectroscopische analyse, die stabiel is bij een verandering van de omgevingsparameters. Temperatuur is een van de kritische omgevingsfactoren. Door het thermo-optische effect [9] en het thermische uitzettingseffect, kunnen temperatuurschommelingen resulteren in spectrale drift voor geïntegreerde fotonische apparaten. Het ontwikkelen van een geïntegreerde temperatuur-ongevoelige filter is noodzakelijk omdat dit calibraties van de chip-gebaseerde FTS mogelijk maakt met een of meer spectrale referenties die niet verschuiven bij temperatuurschommelingen.

Dit doctoraatsproject bestrijkt de drie bovenstaande onderwerpen. We stelden een nieuw type FTS voor op geïntegreerde stationaire FTS, een geïnte-

greerde filter voor sterk excitatielicht met een ultra-hoge dempingsfactor en een temperatuur-ongevoelige filter. De eerste twee worden gerealiseerd op een siliciumnitride (SiN) golfgeleiderplatform. Voor deze twee onderwerpen zullen we eerst de verschillende ontwerpaspecten doornemen en de experimentele resultaten presenteren. Vervolgens zullen we de temperatuur-ongevoelige filter introduceren, waarvan het ontwerp werd gemaakt door voormalige postdoctorale onderzoekers in onze groep. Het prototype werd gerealiseerd op een silicium-op-isolator (SOI) golfgeleiderplatform. In het werk van de temperatuur-ongevoelige filter zijn we vooral betrokken bij de experimentele karakterisering. We hebben veel werk verricht om het prototype te testen en de resultaten te analyseren. Dit werk leidde tot vele bruikbare inzichten, die gebruikt kunnen worden ter verbetering van het voorgestelde concept.

On-chip co-propagatief stationair FTS

Verschillende types FTS kunnen worden onderscheiden door de manier waarop ze het interferogram genereren. Het kan een scanmethode zijn, zoals in de traditionele FTS, waarbij een bewegende spiegel wordt gebruikt om een optisch padverschil (OPD) te creëren en om het interferogram te genereren. Het kan ook een stationaire FTS zijn die geen bewegende component nodig heeft [10–12]. In dit werk stellen we een nieuw type geïntegreerde stationaire FTS voor, waarbij het interferogram bestaat uit een intensiteitsverdeling die ruimtelijk varieert maar constant is in het tijdsdomein. Deze FTS wordt de chip-gebaseerde co-propagatieve stationaire FTS genoemd omdat het interferogram wordt gegenereerd door de interferentie van twee co-propagerende golfgeleidermodi die verschillende fasesnelheden hebben.

Wij stelden twee concepten voor om de co-propagatieve stationaire FTS te implementeren. In het op ‘evanescente-verstrooiing’ gebaseerde concept gebruiken we het interferogram dat wordt gegenereerd door de evanescente velden van de twee geleide modi in het gebied tussen de twee golfgeleiders. In het op ‘zijdelingse lekkage’ gebaseerde concept, maken we gebruik van het laterale lekverschijnsel en de twee modi interfereren in een slab, ver weg van de twee golfgeleiders. In het eerste geval, zoals weergegeven in figuur 1, wordt het licht opgesplitst in twee parallelle golfgeleiders die verschillende breedtes hebben. Terwijl ze zich voortbewegen langs de parallelle golfgeleiders, zullen de twee golfgeleidermodi verschillende optische ver-

tragingen ervaren omdat ze verschillende fase snelheden hebben. De OPD tussen de twee modi zal daarom toenemen met de propagatieafstand. Aangezien de twee golfgeleiders dicht bij elkaar liggen, kunnen de evanescente staarten van de twee golfgeleidermodi licht overlappen en interfereren. Zo kan een interferogram gegenereerd worden in het gebied tussen de twee parallelle golfgeleiders, waar we een goed ontworpen rooster plaatsen om het interferogram naar een detectiesysteem te koppelen.

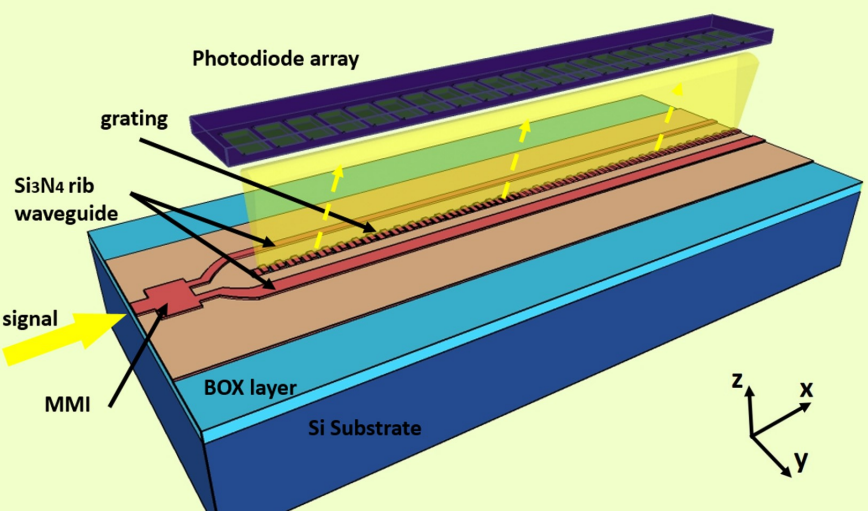

Figuur 1: Een conceptuele tekening van de op evanescente-verstrooiing gebaseerde co-propagatieve stationaire FTS. De figuur is herdrukt uit Ref. [13].

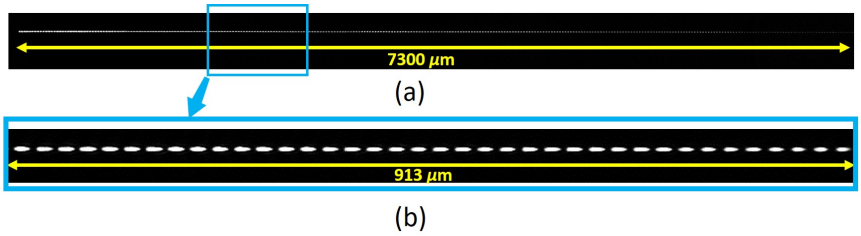

Figuur 2: (a) Het interferogram wordt gereconstrueerd door acht foto's te combineren die door het beeldvormende scansysteem zijn gemaakt. (b) Een van de momentopnamen met een lengte van 913 μm, beperkt door het gezichtsveld van de camera. De figuur is aangepast van Ref. [14].

De prototypes werden gefabriceerd op een SiN ribgolfgeleiderplatform. Experimenteel ontwikkelden we twee benaderingen om de gefabriceerde

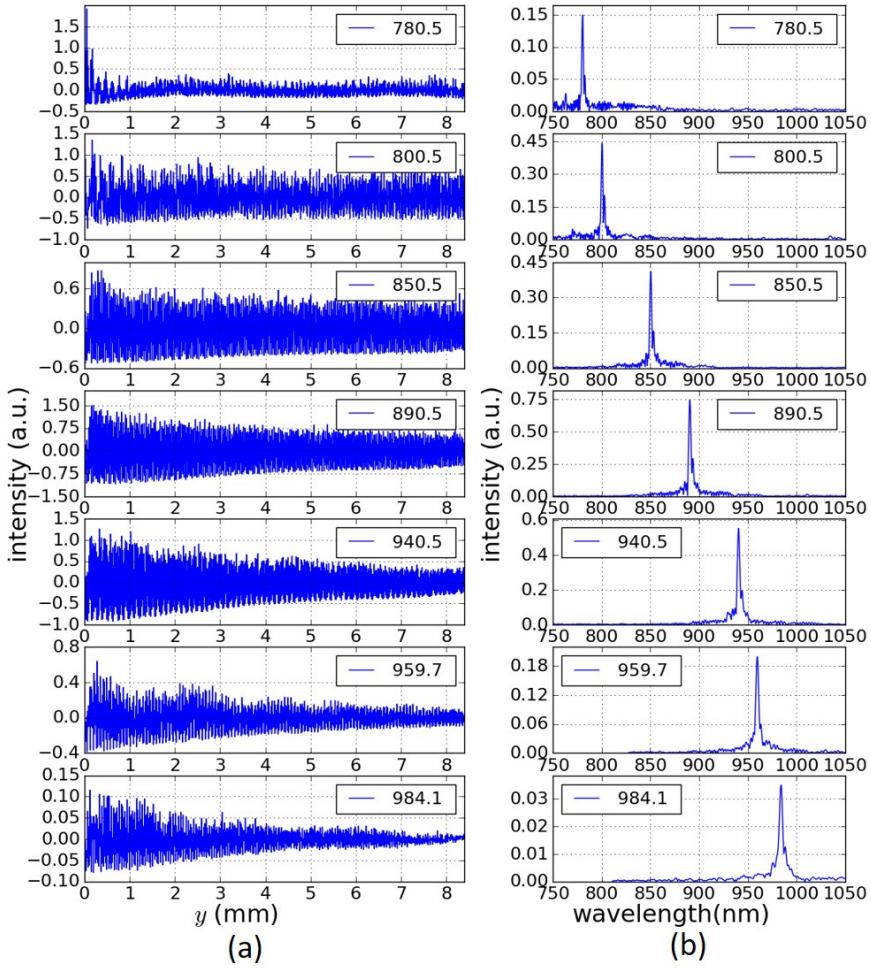

Figuur 3: (a) Interferogrammen die worden gegenereerd door het monochromatische signaal voor verschillende golflengtes, gemeten met de op evanescenet-verstrooiing gebaseerde stationaire FTS. (b) De overeenkomstige spectra, berekend uit de opgemeten interferogrammen.

spectrometers te karakteriseren. In de eerste benadering gebruiken we een scanbeeldvormingssysteem om het interferogram te projecteren en te meten in het verre veld. Met deze benadering zijn we erin geslaagd om het interferogram te observeren zoals weergegeven in figuur 2, rekening houdend met een monochromatisch signaal. De voorlopige experimentele resultaten hebben de haalbaarheid van dit concept aangetoond. Later introduceerden

we het vezelscansysteem, waarmee we het interferogram in het nabije veld (enkele micrometers boven de fotonische chip) kunnen onderzoeken. Met deze opstelling konden we de breedbandwerking aantonen, rekening houdend met zowel monochromatische als polychromatische signalen. Bijvoorbeeld, zoals getoond in figuur 3, zijn we erin geslaagd om een spectraallijn te reconstrueren in een breed golflengtebereik (780-984 nm) met een FWHM-resolutie tot 2 nm met de op evanescente-verstrooiing gebaseerde stationaire FTS.

Tot slot, we hebben een nieuw type van een geïntegreerde stationaire FTS voorgesteld, gerealiseerd en gekarakteriseerd. De resultaten van de experimenten tonen aan dat onze stationaire FTS werkt en nuttig kan zijn voor chip-gebaseerde toepassingen die spectrale metingen vereisen met een matig hoge resolutie in een breed golflengte-bereik. Dit onderzoek gaf ook inzicht in hoe verbeteringen kunnen worden aangebracht in de toekomstige versies van deze FTS.

Geïntegreerde filter voor excitatielicht

De voorgestelde filter voor de afzwakking van excitatielicht is gebaseerd op een specifieke lichtkoppelingsstructuur (GACDC) die bestaat uit een smalle en een brede ribgolfgeleider met een rooster ertussenin. In zo'n golfgeleidersysteem kan contra-directionele koppeling tussen de voorwaartse en achterwaartse propagatiemodi gebeuren met behulp van het rooster [15], zoals weergegeven in figuur 4. Wanneer licht wordt geïnjecteerd in de ene golfgeleider, zal het transmissiespectrum, gemeten aan het andere uiteinde van de golfgeleider, twee stopbanden hebben, namelijk de zelfreflectieband en de kruisreflectieband. Het GACDC filter is geschikt voor het afzwakken van excitatielicht voor Raman-spectroscopie. De voordelen zijn dat het een onbeperkte FSR heeft in het golflengtegebied waar de Raman stokessignalen zitten en dat het gefilterde licht efficiënt afgezonderd kan worden. Een ander belangrijk voordeel is dat het GACDC-filter efficiënt kan worden gecascadeerd om een hoge dempingsfactor te bereiken. Deze dempingsfactor is hoger dan het vaak gerapporteerde verzadigingsniveau (vaak rond de 40 dB) dat beperkt wordt door fabricagefouten [16–18].

We hebben de voorgestelde filters gefabriceerd op een SiN ribgolfgeleiderplatform met e-beam lithografie voor snelle prototyping. Experimenteel toonden we aan dat voor de enkelvoudige GACDC filter, de dempingsfactor

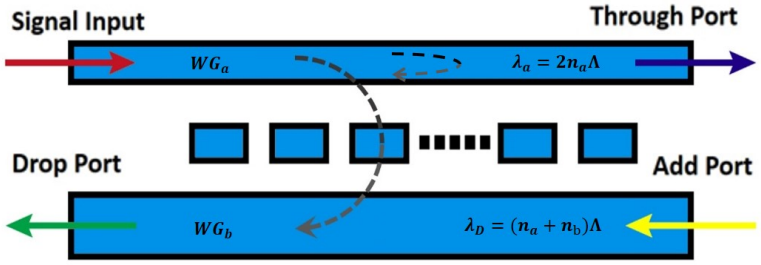

Figuur 4: Schematisch bovenaanzicht van de filter.

verzadigd tot minder dan 40 dB, vanaf een filterlengte van 2000 μm. Met de trapsgewijze GACDC filter kunnen we dit verzadigingsniveau overtreffen. Zo hebben we een ultra-hoge dempingsfactor van 68,5 dB opgemeten bij een centrale golflengte van 783,6 nm voor een 16-traps GACDC filter met een totale filterlengte van 2000 μm.

Tot slot, hoewel er nog ruimte voor verbetering is, hebben we experimenteel aangetoond dat onze voorgestelde trapsgewijze GACDC-filters veelbelovend zijn. Ze kunnen immers een veel hogere extinctieratio bereiken in vergelijking met de eentrapsversie. Met de andere unieke voordelen zoals hierboven vermeld, geloven we dat de filter zijn nut kan bewijzen bij chip-gebaseerde Raman spectroscopie voor het filteren van het sterke excitatielicht.

Geïntegreerde temperatuur-ongevoelige filter

Zoals geschetst in figuur 5, kan het voorgestelde temperatuurongevoelige filter op de chip worden gezien als een filter op basis van een rooster in de vrije ruimte dat in wezen temperatuurongevoelig kan zijn. Het heeft twee essentiële componenten: een Littrow rooster op de chip en een spiegel die parallel aan de chip wordt gehouden op een vaste, ontworpen hoogte. De werking is als volgt: het licht koppelt via de eerste roosterkoppelaar naar de chip en verspreidt zich in een golfgeleider tot het door een tweede roosterkoppelaar onder een specifieke uit-koppelingshoek de chip verlaat. Nadat de uitgekoppelde lichtbundel door de spiegel wordt gereflecteerd, landt deze op het Littrow rooster. Voor een vooraf bepaalde golflengte kan het Littrow rooster de lichtstraal langs de invalrichting weerkaatsen, waardoor het mogelijk is terug te keren naar de tweede roosterkoppeling die

het licht weer in de golfgeleider koppelt. Voor een chip-gebaseerde component, kunnen temperatuurschommelingen spectrale afwijkingen veroorzaken door het thermo-optisch effect en het thermische uitzettingseffect. Beide effecten kunnen met dit ontwerp vermeden worden.

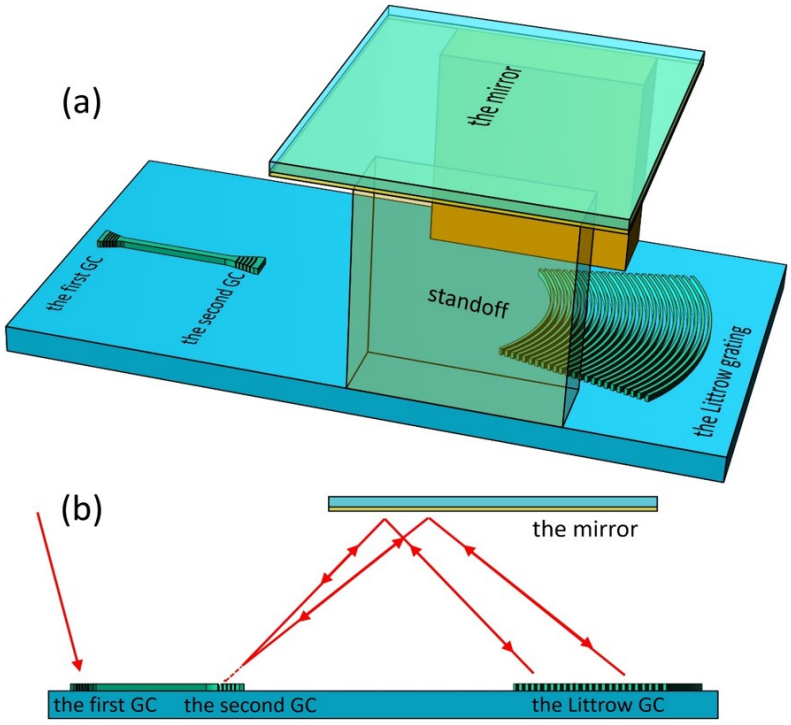

Figuur 5: (a) Een 3D-schets van de voorgestelde temperatuurongevoelige filter. (b) Een zijaanzicht van de component dat de weg van het licht met de ontwerpgolflengte toont. Het licht kan worden gereflecteerd en opnieuw worden gericht op de tweede roosterkoppeling na meerdere reflecties.

In de eerste experimenten hebben we een negatieve spectrale drift van meer dan -100 pm/K gemeten. Deze ongewenste resultaten konden verklaard worden door de niet-geoptimaliseerde spiegelpositie. Dit geeft aan dat het van cruciaal belang is om de spiegel perfect parallel aan de fotonische chip op de juiste hoogte te houden. Verder hebben we experimenten uitgevoerd met een spiegel “brug” waarvan de leggers de gewenste thermische uitzettingscoefficiënt hebben, en de spiegelpositie quasi optimaal is. In deze experimenten merkten we dat er een andere temperatuurgevoeligheid ontstaat door de spiegel “ brug” zachtjes te bewegen. Het beste resultaat is een

spectrale drift van -4 pm/K.

Samengevat, hebben we een doorlaatfilter voorgesteld die in belangrijke mate temperatuur ongevoelig kan zijn. Experimenteel hebben we aangetoond dat met de voorgestelde filter de spectrale drift ten gevolge van temperatuurschommelingen aanzienlijk kan worden verminderd. Hoewel de reproduceerbaarheid van het beste resultaat onvoldoende is met het huidige prototype, zijn wij van mening dat, met enkele verdere verbeteringen, de voorgestelde temperatuur-ongevoelige filter stabiel zou moeten werken. De filter is dan nuttig voor het verstrekken van een athermische on-chip golflengte referentie voor chip-gebaseerde spectroscopische toepassingen.

Referenties

[1] PB Fellgett. *On the ultimate sensitivity and practical performance of radiation detectors*. JOSA, 39(11):970–976, 1949.

[2] Pierre Jacquinot. *New developments in interference spectroscopy*. Reports on progress in physics, 23(1):267, 1960.

[3] Pierre Connes. *Astronomical fourier spectroscopy*. Annual Review of Astronomy and Astrophysics, 8(1):209–230, 1970.

[4] Joshua Manor, Esther S Feldblum, Martin T Zanni, and Isaiah T Arkin. *Environment polarity in proteins mapped noninvasively by FTIR spectroscopy*. The journal of physical chemistry letters, 3(7):939–944, 2012.

[5] Alan G Marshall, Christopher L Hendrickson, and George S Jackson. *Fourier transform ion cyclotron resonance mass spectrometry: a primer*. Mass spectrometry reviews, 17(1):1–35, 1998.

[6] Pradip Gatkine, Sylvain Veilleux, and Mario Dagenais. *Astrophotonic Spectrographs*. Applied Sciences, 9(2):290, 2019.

[7] Chris D Boone, Ray Nassar, Kaley A Walker, Yves Rochon, Sean D McLeod, Curtis P Rinsland, and Peter F Bernath. *Retrievals for the atmospheric chemistry experiment Fourier-transform spectrometer*. Applied Optics, 44(33):7218–7231, 2005.

[8] Ashim Dhakal, Ananth Z Subramanian, Pieter Wuytens, Frédéric Peyskens, Nicolas Le Thomas, and Roel Baets. *Evanescent excitation and collection of spontaneous Raman spectra using silicon nitride nanophotonic waveguides*. Optics letters, 39(13):4025–4028, 2014.

[9] Hiroshi Nishihara, Masamitsu Haruna, and Toshiaki Suhara. *Optical integrated circuits*. New York, pages 7–8, 1989.

[10] Etienne Le Coarer, Sylvain Blaize, Pierre Benech, Ilan Stefanon, Alain Morand, Gilles Lérondel, Grégory Leblond, Pierre Kern, Jean Marc Fedeli, and Pascal Royer. *Wavelength-scale stationary-wave integrated Fourier-transform spectrometry*. Nature Photonics, 1(8):473, 2007.

[11] Mirosław Florjańczyk, Pavel Cheben, Siegfried Janz, Alan Scott, Brian Solheim, and Dan-Xia Xu. *Planar waveguide spatial heterodyne spectrometer*. In Photonics North 2007, volume 6796, page 67963J. International Society for Optics and Photonics, 2007.

[12] Derek M Kita, Brando Miranda, David Favela, David Bono, Jérôme Michon, Hongtao Lin, Tian Gu, and Juejun Hu. *High-performance and scalable on-chip digital Fourier transform spectroscopy*. Nature communications, 9(1):4405, 2018.

[13] Xiaomin Nie, Eva Ryckeboer, Günther Roelkens, and Roel Baets. *Novel concept for a broadband co-propagative stationary Fourier transform spectrometer integrated on a Si3N4 waveguide platform*. In CLEO: Applications and Technology, pages JW2A–120. Optical Society of America, 2016.

[14] Xiaomin Nie, Eva Ryckeboer, Günther Roelkens, and Roel Baets. *CMOS-compatible broadband co-propagative stationary Fourier transform spectrometer integrated on a silicon nitride photonics platform*. Optics express, 25(8):A409–A418, 2017.

[15] Min Qiu, Mikael Mulot, Marcin Swillo, Srinivasan Anand, Bozena Jaskorzynska, Anders Karlsson, Martin Kamp, and Alfred Forchel. *Photonic crystal optical filter based on contra-directional waveguide coupling*. Applied Physics Letters, 83(25):5121–5123, 2003.

[16] J Wang, I Glesk, and LR Chen. *Subwavelength grating Bragg grating filters in silicon-on-insulator*. Electronics Letters, 51(9):712–714, 2015.

[17] Diego Pérez-Galacho, Carlos Alonso-Ramos, Florent Mazeas, Xavier Le Roux, Dorian Oser, Weiwei Zhang, Delphine Marris-Morini, Laurent Labonté, Sébastien Tanzilli, Eric Cassan, et al. *Optical pump-rejection filter based on silicon sub-wavelength engineered photonic structures*. Optics letters, 42(8):1468–1471, 2017.

[18] Xu Wang, Wei Shi, Raha Vafaei, Nicolas AF Jaeger, and Lukas Chrostowski. *Uniform and sampled Bragg gratings in SOI strip waveguides with sidewall corrugations*. IEEE Photonics Technology Letters, 23(5):290–292, 2011.

English summary

Optical spectrometers have long been known as indispensable tools in various fields that require optical spectrum analysis. Among different types of modern spectrometers, a Fourier transform spectrometer (FTS) offer important advantages [1–3]. Consequently, the FTS has found many applications in the field of biological sciences, molecular sciences, atmospheric sciences, and astronomy [4–7]. However, a conventional FTS is bulky and expensive. Therefore, it is interesting to explore the on-chip integrated FTS, given the increasing demand and the growing preference for portable and robust FTS devices. Moreover, to make an on-chip FTS ready to work in an integrated optical spectroscopic system, we need to develop other on-chip components. In the case where we want to use an on-chip integrated FTS as the spectral analyzer for on-chip Raman spectroscopy [8], we need to integrate an on-chip pump rejection filter (with an extinction ratio of around 100 dB) in front of the on-chip FTS. The on-chip pump rejection filter with an ultra-high extinction ratio could help to remove the strong pump light and thus reveal weak Raman signals. Furthermore, it is often required that, for an accurate spectroscopic analysis, the spectrometer should give spectral readings that are stable to a change of environmental parameters. Temperature is one of the factors. Through the thermo-optical effect [9] and the thermal expansion effect, temperature variations can result in spectral drift for the integrated photonic devices. Developing an on-chip integrated temperature-insensitive filter becomes necessary as it allows for calibrations of the on-chip spectrometer with one or more on-chip spectral references that do not shift under temperature variations.

This Ph.D. project covers the three topics introduced above. We proposed a new type for an on-chip stationary FTS, an on-chip pump rejection filter with ultra-high extinction ratio and an on-chip temperature-insensitive filter. The first two are realized on a silicon nitride (SiN) waveguide platform. For these two topics, we firstly will go through the design details and present the experimental results. Next, we will introduce the on-chip

temperature-insensitive filter, of which the design is made by former post-doctoral researchers in our group, and the prototype is realized on a silicon-on-insulator (SOI) waveguide platform. In the work on the temperature-insensitive filter, we are mainly involved in the experimental characterization. We made many efforts to test the prototype device and to analyze the results, which lead to useful insights into the proposed concept.

On-chip co-propagative stationary FTS

Different types of FTS can be differentiated by how they generate the interferogram. It can be a scanning manner as in the traditional FTS where a moving mirror is used to create an optical path difference (OPD) and to generate the interferogram. It can also be a stationary one which requires no moving component [10–12]. In this work, we propose a new type of integrated stationary FTS, where the interferogram is generated as the intensity distribution that is spatially varying but temporally stationary. It is named on-chip co-propagative stationary FTS as the interferogram is generated from the interference between two co-propagative waveguide modes that have different phase velocities.

We proposed two approaches to implement the co-propagative stationary FTS. In the evanescent-scattering-based approach, we use the interferogram generated by the evanescent fields of the two guided modes in the region between the two waveguides, while in the lateral-leakage-based approach, we leverage the lateral leakage phenomenon and let the two modes interfere in the slab far away from the two waveguides. In the former case, as shown in figure 6, the light is split into two parallel waveguides that have different widths. While propagating along the parallel waveguides, the two waveguide modes will experience different optical delays as they have different phase velocities. The OPD between the two modes will, therefore, increase with the propagation distance. Since the two waveguides sit close to each other, the evanescent tails of the two waveguide modes can overlap slightly and interfere with each other. As such, a spatially varying interferogram can be generated in the region between the two parallel waveguides, where we position a well-designed grating to scatter the interferogram to a detection system.

The prototype devices are fabricated on a SiN rib waveguide platform. Experimentally, we developed two approaches to characterize the fabricated

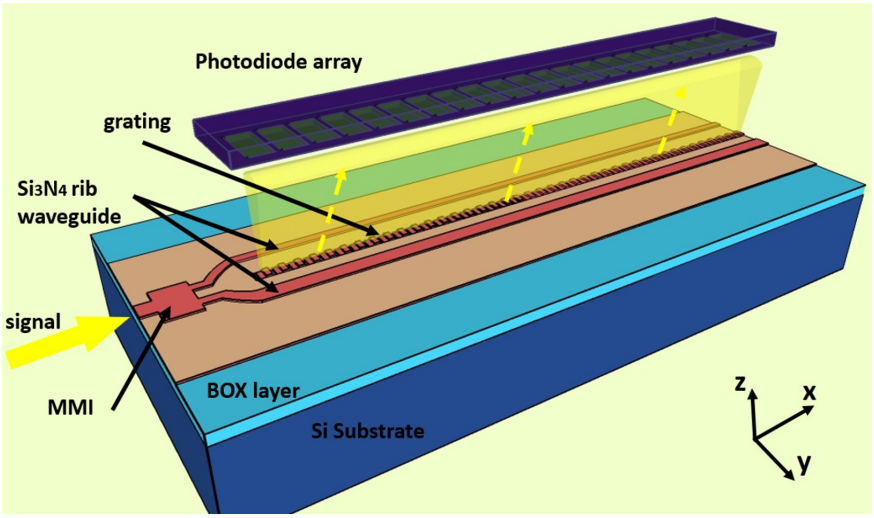

Figure 6: A conceptual drawing of the evanescent-scattering-based co-propagative stationary FTS. The figure is reprinted from Ref. [13].

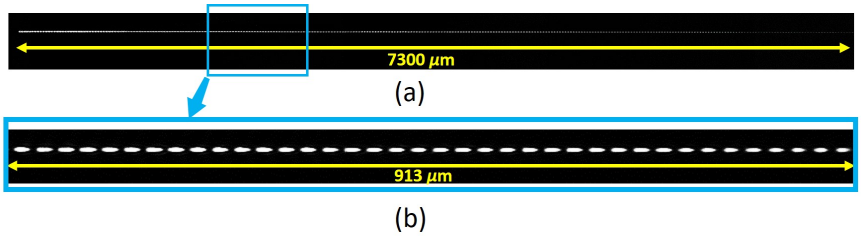

Figure 7: (a) The interferogram reconstructed by stitching eight snapshots taken by the scanning imaging system. (b) One of the snapshots covering a length of 913 μm as limited by the field of view. The figure is adapted from Ref. [14].

devices. In the first approach, we use a scanning imaging system to project the interferogram and measure it in the far-field. With this approach, we managed to observe the interferogram as shown in figure 7 considering a monochromatic signal. The preliminary experimental results proved the feasibility of the concept. Later, we introduced the fiber scanning system, which allows us to probe the interferogram in the near-field (several micrometers above the photonic chip). With this setup, we were able to demonstrate the broadband operation considering both monochromatic and polychromatic signals. For example, as shown in figure 8, we managed to reconstruct the spectral line in a wide wavelength range (780-984 nm) with

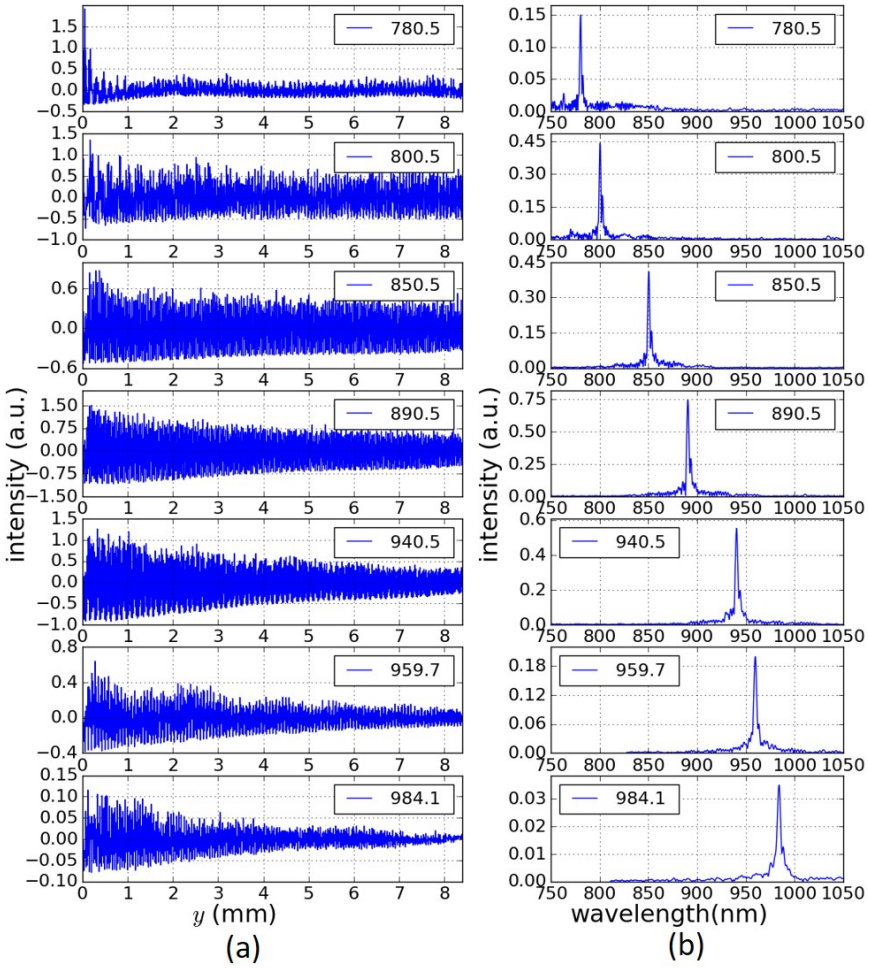

Figure 8: (a) Interferograms generated by the monochromatic signal for different wavelength measured with the evanescent-scattering-based on-chip stationary FTS. (b) the corresponding spectra calculated with the measured interferograms.

the FWHM resolution down to 2 nm with the evanescent-scattering-based on-chip stationary FTS.

To conclude, we proposed, realized, and characterized a new type of on-chip stationary FTS. The results obtained from the experiments indicate that our on-chip stationary FTS works and can be useful for on-chip applications that require spectral measurement with a moderately high resolution

in a broad bandwidth. Further investigations also gave insights into how to make improvements in future versions of the on-chip FTS.

On-chip pump-rejection filter

The proposed on-chip pump-rejection filter is based on the grating-assisted contra-directional coupler (GACDC) which consists of a narrow and a wide rib waveguide and a grating in between. In such a waveguides system, the contra-directional coupling could happen between the forward and backward propagating modes with the assistance of the grating [15]. It could be the intra-waveguide Bragg reflection in one waveguide, or the inter-waveguide contra-directional coupling that happens between the two waveguides, as shown in figure 9. Correspondingly, when light is injected in one waveguide, the transmission spectrum measured at the other end of the waveguide will have two stops bands, i.e., the self-reflection band and cross-reflection band. The GACDC filter is suitable for pump rejection for on-chip Raman spectroscopy. The advantages are that it is FSR-free in the wavelength region where the Raman stokes signals sit and that the rejected light could be coupled out through the bus waveguide instead of going back to the input port. Another important advantage is that the GACDC filter can be efficiently cascaded to achieve a high extinction ratio that is beyond the often-reported saturation level (often around 40 dB) set by the fabrication imperfections [16–18].

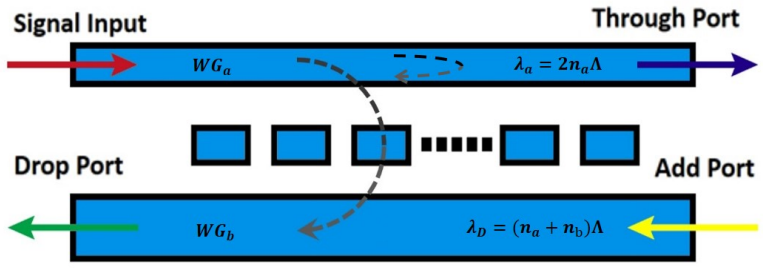

Figure 9: Schematic top view of the proposed grating assisted contra-directional coupler.

We fabricated the proposed filters on a SiN rib waveguide platform with e-beam lithography for fast prototyping. Experimentally, we showed that for the single-stage GACDC filter, the extinction ratio saturates to less

than 40 dB, starting from the filter length of 2000 μm. With the cascaded GACDC filter, we can surpass this saturation level. In fact, we measured an ultra-high extinction ration of 68.5 dB at the center wavelength of 783.6 nm from a 16-stage cascaded GACDC filter with a total filter length of 2000 μm.

In conclusion, while there is still room for improvement, we experimentally demonstrated that our proposed cascaded on-chip GACDC filters are promising as it can achieve much higher extinction ration as compared to the single stage version. With the other unique advantages as mentioned above, we believe it can be useful for pump rejection in applications such as on-chip Raman spectroscopy.

On-chip temperature-insensitive filter

As sketched in figure 10, the proposed on-chip temperature-insensitive filter can be seen as a free-space grating-based filter that can be substantially temperature insensitive. It has two essential components: an on-chip Littrow grating and a mirror that is held in parallel to the chip by a standoff with a designed height. In operation, the light is coupled into the chip through the first grating coupler and propagates in a wire waveguide until being coupled out by a second grating coupler into the air under a specific out-coupling angle. After being redirected by the mirror, the light beam propagates back to the chip and lands on the Littrow grating. For a predetermined wavelength, the Littrow grating is an easy-to-design component that can reflect the light beam back along the incidence direction, allowing for returning to the second grating coupler which couples the light back into the waveguide. For an on-chip device, temperature variations could induce spectral drifts through the thermo-optic effect and the thermal expansion effect. The former is compensated for as we are using a free-space approach (with the propagating medium being air) to filter the light. Furthermore, by selecting a material with the desired thermal expansion coefficient (TEC) for the standoff, the latter could also be compensated.

In the preliminary experiments, we measured a negative drift rate of more than -100 pm/K. The undesired results come from the non-optimized mirror position which indicates that it is critical to have the mirror in parallel to the photonic chip at the correct height. We further performed experiments with a mirror “bridge” of which the position is close to optimum, and the

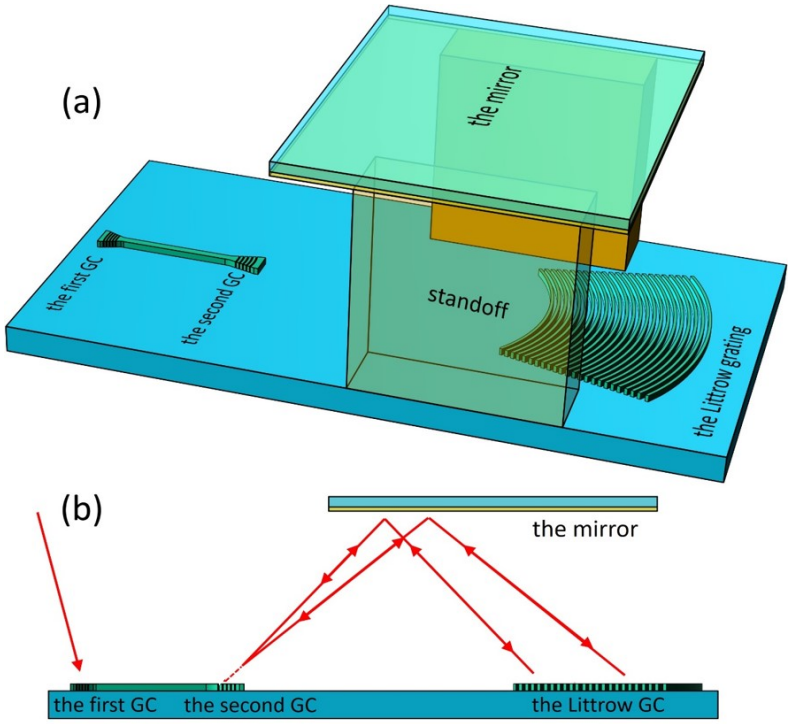

Figure 10: (a) A 3D sketch of the proposed temperature-insensitive filter. (b) A side view of the device (the standoff is not drawn) showing the path of the light with a proper wavelength. The light can be reflected and refocused to the second grating coupler after multiple reflections.

standoff has the desired TEC. In these experiments, we noticed different temperature sensitivities could be obtained by slightly moving the mirror "bridge". The best result we demonstrated is a drift rate of -4 pm/K.

To summarize, we proposed an on-chip passband filter that could be substantially temperature-insensitive. Experimentally, we demonstrated that with the proposed filter, the thermal drift could be significantly reduced. While the reproducibility of the best result is inadequate for the current prototype, we believe that, with some further improvements, the proposed temperature-insensitive filter should work stably and could be useful for providing an athermal on-chip wavelength reference for on-chip spectroscopic applications.

References

[1] PB Fellgett. *On the ultimate sensitivity and practical performance of radiation detectors*. JOSA, 39(11):970–976, 1949.

[2] Pierre Jacquinot. *New developments in interference spectroscopy*. Reports on progress in physics, 23(1):267, 1960.

[3] Pierre Connes. *Astronomical fourier spectroscopy*. Annual Review of Astronomy and Astrophysics, 8(1):209–230, 1970.

[4] Joshua Manor, Esther S Feldblum, Martin T Zanni, and Isaiah T Arkin. *Environment polarity in proteins mapped noninvasively by FTIR spectroscopy*. The journal of physical chemistry letters, 3(7):939–944, 2012.

[5] Alan G Marshall, Christopher L Hendrickson, and George S Jackson. *Fourier transform ion cyclotron resonance mass spectrometry: a primer*. Mass spectrometry reviews, 17(1):1–35, 1998.

[6] Pradip Gatkine, Sylvain Veilleux, and Mario Dagenais. *Astrophotonic Spectrographs*. Applied Sciences, 9(2):290, 2019.

[7] Chris D Boone, Ray Nassar, Kaley A Walker, Yves Rochon, Sean D McLeod, Curtis P Rinsland, and Peter F Bernath. *Retrievals for the atmospheric chemistry experiment Fourier-transform spectrometer*. Applied Optics, 44(33):7218–7231, 2005.

[8] Ashim Dhakal, Ananth Z Subramanian, Pieter Wuytens, Frédéric Peyskens, Nicolas Le Thomas, and Roel Baets. *Evanescent excitation and collection of spontaneous Raman spectra using silicon nitride nanophotonic waveguides*. Optics letters, 39(13):4025–4028, 2014.

[9] Hiroshi Nishihara, Masamitsu Haruna, and Toshiaki Suhara. *Optical integrated circuits*. New York, pages 7–8, 1989.

[10] Etienne Le Coarer, Sylvain Blaize, Pierre Benech, Ilan Stefanon, Alain Morand, Gilles Lérondel, Grégory Leblond, Pierre Kern, Jean Marc Fedeli, and Pascal Royer. *Wavelength-scale stationary-wave integrated Fourier-transform spectrometry*. Nature Photonics, 1(8):473, 2007.

[11] Mirosław Florjańczyk, Pavel Cheben, Siegfried Janz, Alan Scott, Brian Solheim, and Dan-Xia Xu. *Planar waveguide spatial heterodyne spectrometer*. In Photonics North 2007, volume 6796, page 67963J. International Society for Optics and Photonics, 2007.

[12] Derek M Kita, Brando Miranda, David Favela, David Bono, Jérôme Michon, Hongtao Lin, Tian Gu, and Juejun Hu. *High-performance and scalable on-chip digital Fourier transform spectroscopy*. Nature communications, 9(1):4405, 2018.

[13] Xiaomin Nie, Eva Ryckeboer, Günther Roelkens, and Roel Baets. *Novel concept for a broadband co-propagative stationary Fourier transform spectrometer integrated on a Si3N4 waveguide platform*. In CLEO: Applications and Technology, pages JW2A–120. Optical Society of America, 2016.

[14] Xiaomin Nie, Eva Ryckeboer, Günther Roelkens, and Roel Baets. *CMOS-compatible broadband co-propagative stationary Fourier transform spectrometer integrated on a silicon nitride photonics platform*. Optics express, 25(8):A409–A418, 2017.

[15] Min Qiu, Mikael Mulot, Marcin Swillo, Srinivasan Anand, Bozena Jaskorzynska, Anders Karlsson, Martin Kamp, and Alfred Forchel. *Photonic crystal optical filter based on contra-directional waveguide coupling*. Applied Physics Letters, 83(25):5121–5123, 2003.

[16] J Wang, I Glesk, and LR Chen. *Subwavelength grating Bragg grating filters in silicon-on-insulator*. Electronics Letters, 51(9):712–714, 2015.

[17] Diego Pérez-Galacho, Carlos Alonso-Ramos, Florent Mazeas, Xavier Le Roux, Dorian Oser, Weiwei Zhang, Delphine Marris-Morini, Laurent Labonté, Sébastien Tanzilli, Eric Cassan, et al. *Optical pump-rejection filter based on silicon sub-wavelength engineered photonic structures*. Optics letters, 42(8):1468–1471, 2017.

[18] Xu Wang, Wei Shi, Raha Vafaei, Nicolas AF Jaeger, and Lukas Chrostowski. *Uniform and sampled Bragg gratings in SOI strip waveguides with sidewall corrugations*. IEEE Photonics Technology Letters, 23(5):290–292, 2011.

1 Introduction

An optical spectrometer is an indispensable tool in various fields that require optical spectrum analysis. Among all types of modern spectrometers, the Fourier transform spectrometer offers important advantages. The high demand for the Fourier transform spectrometers, and the growing preference for portable and robust devices have together created a trend towards the miniaturization and integration of the Fourier transform spectrometer, motivating the work of this Ph.D. project.

Contents

1.1 Fourier transform spectrometer

A Fourier transform spectrometer (FTS) can be classified as a time-domain spectrometer to be differentiated from its frequency-domain competitor, the dispersive spectrometer [1, 2]. A typical dispersive spectrometer spatially separates the different frequency components of the light field either with a dispersive element, such as a grating or a prism and detects the light by scanning it onto a single detector or by measuring with multi-channel detectors. Differently, the conventional FTS measures the interference pattern (or interferogram) created by the light field and its delayed version in the time-domain. The spectral contents of the light field are encoded in the interferogram and can be decoded by applying a mathematical process, i.e., a Fourier transform (FT). Typically, an FTS uses a Michelson interferometer (MI) to generate the interferogram [3].

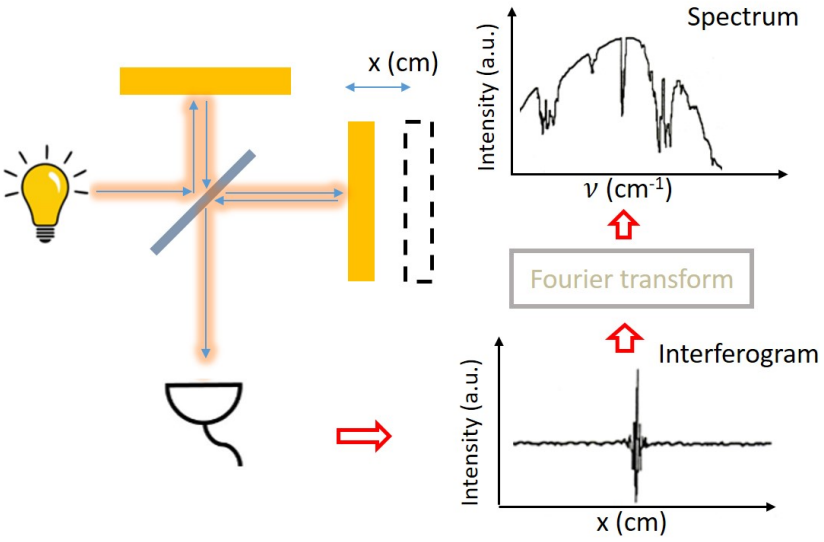

Figure 1.1: An illustrative sketch of the FTS that uses an MI as the interferometer.

As shown in 1.1, in its simplest form, an MI uses a beam splitter to split the light into two replicas that have the same amplitude. One of the replicas goes to a stationary mirror, while the other goes to a moving mirror. After being reflected by the mirrors, both replicas propagate back, get combined at the splitter and go to a detector. As the moving mirror moves, the two replicas will go through different optical path length and therefore generating an optical path difference (OPD) that scales with the movement of the

mirror. An interferogram describes how the detected light power varies as a function of OPD, which after applying a Fourier transform, will give the spectrum of the light. As a widely used example, a monochromatic light signal creates a sinusoidal interferogram, which can be mathematically explained by the FT-relation between the δ function and the sinusoidal function. More examples of how the interferogram should look like for light with different spectral contents are shown in figure 1.2.

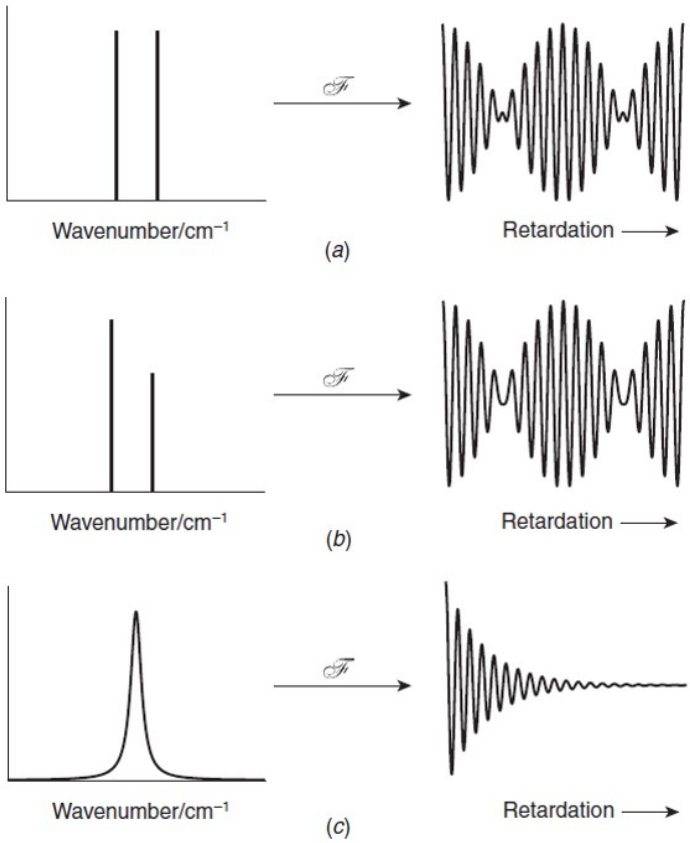

Figure 1.2: Examples of the interferogram generated by light with different spectral contents: (A) two monochromatic lines with equal intensity, (B) two monochromatic lines of unequal intensity. (C) a broad Lorentzian line. $\mathscr{F}$ denotes the Fourier transform. Adapted from [1].

1.1.1 Resolution of FTS

As implied by the famous uncertainty principle, functions that are localized in the time domain have Fourier transforms that are spread out across the frequency domain and vice versa. This means, to have a high resolution, an FTS should allow the measurement of a long interferogram. For a maximal measurable OPD in the unit of cm, the spectral resolution could be expressed as the difference in wavenumber, typically denoted by $\delta\tilde{\nu}$ in the unit of cm^{-1}. From the wavenumber resolution, we can calculate and the frequency resolution δf as $c{\cdot}\delta\tilde{\nu}$ with c the speed of light and the wavelength resolution $\delta\lambda$ as $\lambda^2 \cdot \delta\tilde{\nu}$ for the center wavelength of λ. As an example, a maximal OPD of 0.25 cm as in some cheap FTS instruments could give a wavenumber resolution of 4 cm^{-1}, which corresponds to a frequency resolution of 125 GHz or a wavelength resolution around 1 nm at the center wavelength of 1550 nm. Although obtaining a long interferogram is not always easy, the FTS has evolved from its early lab version as the one built by Connes in 1966 that can measure spectra of Venus and Mars with about 1 cm^{-1} resolution [4] to the modern high resolution (0.001 cm^{-1}) version that is now commercially available.

1.1.2 Sampling the interferogram

Another important aspect of FTS is the sampling of the interferogram. According to Fourier transform theory [1], to compute the complete spectrum extending from 0 to ∞ cm^{-1}, one needs to sample the interferogram with infinitely high sample rate, or in other words, infinitely small sample step-length. In practice, the digitization of the interferogram is always done with a finite sample step-length. This will lead to a specific maximum frequency that can be calculated with a Discrete Fourier Transform (DFT) [5]. According to Nyquist-Shannon's sampling theorem, the reciprocal of twice of the sample step-length determines the largest wavenumber $\tilde{\nu}_{max}$. Again, one can calculate the maximum frequency

$$f_{max} = c \cdot \tilde{\nu}_{max}, \tag{1.1}$$

where c the speed of light, and the minimum wavelength

$$\lambda_{min} = 1/\tilde{\nu}_{max}. \tag{1.2}$$

The sampling theorem tells that if a function contains no spatial frequencies higher than $\tilde{\nu}_{max}$ in the unit of the inverse centimeter, it is completely determined by giving its values at a set of points that are equally spaced

$1/(2\tilde{\nu}_{max})$ centimeters apart. In the case the sampling theorem is not fulfilled, the spectral content with higher spatial frequencies will create a so-called alias folded into the range (from 0 to $\tilde{\nu}_{max}$) when a sampling spatial frequency of $2\tilde{\nu}_{max}$ is concerned.

1.1.3 Aliasing and Subsampling

To further illustrate the alias, we can look at an example. Three spectral features (R, S and T) are located in the wavelength range 0 to F, F to $2F$ and $2F$ to $3F$, respectively. Assuming a sampling frequency of $2F$, DFT will only calculate the spectrum up to frequency F. Feature R can be determined unambiguously as it is sampled sufficiently according to the Nyquist criterion. Therefore, it exists in the range (0 to F) as shown in the schematic spectrum in figure 1.3. However, the high frequency features S, and T will also appear in this range in the form of alias as T'' and S'. In fact, without additional information, it is impossible to distinguish which of the features is real and which is an alias. In such a situation, the interferogram is subsampled as the sample rate is not enough to unambiguously determine the spectral contents. For an FTS with a sampling frequency of $2F$, subsampling will not forbid one from measuring the spectral features with frequency higher than F. It gives the possibility to look into the window of F to $2F$ or $2F$ to $3F$ due to aliasing. However, one needs to make sure there is no spectral content outside the interested window. In short, subsampling limits the operational bandwidth of an FTS.

1.1.4 Advantages of FTS

Fourier transform spectrometers, or sometimes called Fourier transform infrared spectrometers (FTIRs), are widely used to work in the infrared spectral range for applications in the field of biological sciences [6–8], molecular sciences [9, 10], astronomy [11, 12] as well as atmospheric sciences [13, 14]. The following advantages lead to its popularity.

- **Felgett's advantage** This advantage, also known as the multiplex advantage, originates from the fact that all wavelengths are collected simultaneously [15]. For a system that is limited by a fixed detector noise, which is often the case in the infrared wavelength range [16], this leads to a higher Signal-to-Noise Ratio (SNR). For instance, for a spectrum with m resolution elements, the SNR will be improved by a factor of the square root of m. Nevertheless, in the visible range

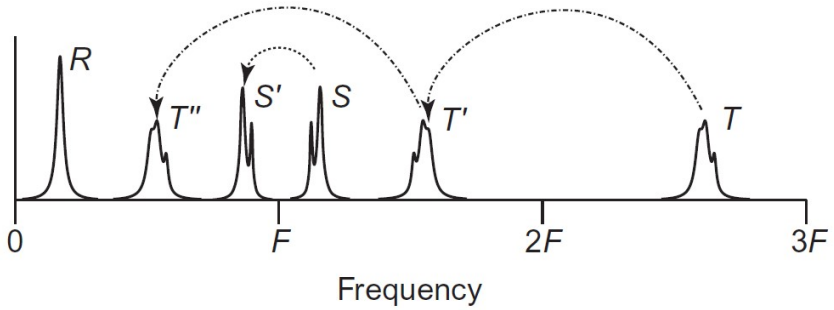

Figure 1.3: A schematic spectrum with three spectral features: R, S, and T. R is within the appropriate bandwidth for sampling, 0 to F, and it is not folded. S falls in the bandwidth above F and below $2F$. Due to subsampling, it is folded to S'. T is in the frequency range from $2F$ to $3F$. Similarly, it is folded to T' in the region F to $2F$ and then mirrored to T'' in the 0 to F region. Reprinted from Ref. [1].

where low-cost multiplex detectors are available, and the system is usually limited by the shot noise of the light [17], this advantage disappears and makes FTS less attractive in this aspect.

- **Jacquinot's advantage** Also known as the throughput advantage, it says that higher throughput can be obtained with a standard FTS when compared with dispersive spectrometers [18]. For a dispersive spectrometer, to obtain a high resolution, the entrance slit needs to be small, which reduces the throughput. A high-resolution FTS does not require such a small slit. Instead, it uses a Jacquinot stop to restrict the convergence of the collimated beam. As reported, for the same resolving power, by replacing the slit with the Jacquinot stop, an FTS can provide a throughput of $\sim$60 times higher than that of the dispersive spectrometer [19]. The result is a significantly improved SNR if the detector noise is dominant.

- **Connes' advantage** In a typical FTS, there is a built-in calibration system which uses a laser of known wavelength to measure the moving distance of the movable mirror. This interference-based calibration often offers a more stable and accurate absolute wavelength scale than that in the dispersive spectrometers.

Other than the advantages mentioned above, FTS is also advantageous in obtaining a high resolution and, at the same time, a broad operational band-

width due to the advancement of modern motion control technologies. Consequently, it is motivated to extend FTS also to the visible or even ultraviolet (UV) wavelength ranges.

1.2 Miniaturized and Integrated Fourier transform spectrometer

As an essential measuring instrument, the FTS attracts researchers to invent modern versions that are portable, robust, and have high performance and low cost. Recently we witness many efforts spent to miniaturize and even to integrate the FTS.

1.2.1 Miniaturized FTS with a moving component

There are various miniaturized Fourier transform spectrometers that still involve moving components such as the optical Micro-Electro-Mechanical System (MEMS) [20–22] and the movable birefringent wedges [23].

1.2.1.1 MEMS-based FTS

A compact MEMS-based FTS module assembled on silicon optical bench is shown in figure 1.4 (a), consisting of a MEMS mirror, a fixed mirror, and a beam splitter with the size of 1 cm^3. The key component of this miniaturized FTS is the electrothermal MEMS mirror, as shown in the scanning electron microscope (SEM) picture in figure 1.4 (b). It is reported, by utilizing the MEMS mirror, such a miniaturized FTS with a footprint of 2 cm $\times$ 2 cm can achieve a linear scan range of optical path difference (OPD) up to 450 μm (with only 6 Vdc) [22]. Such a scan range corresponding to a spectral resolution of 40 cm^{-1}, or 1.1 nm at 532 nm, which is comparable to some commercialized portable spectrometers.

1.2.1.2 Birefringent-wedge-based FTS

Figure 1.5 shows a schematic setup of a miniaturized FTS based on the birefringent wedges. As shown in the schematic, the input light beam is split equally into two perpendicularly polarized components propagating collinearly along the fast and slow axes of the birefringent material. After

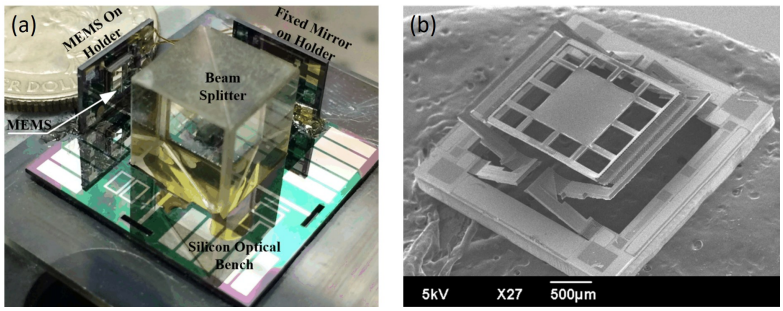

Figure 1.4: (a) The assembled compact FTS module on a silicon optical bench. (b) SEM pitcure of an electrothermal MEMS mirror. Reprinted from [22].

the first piece of birefringent material, the linearly polarized light becomes circularly or elliptically polarized. A changeable optical delay is generated by precisely varying the thickness of the second piece of birefringent material, i.e., moving the wedge along the direction indicated by the double-sided arrow. After that, the two delayed replicas go to a Wollaston prism (WP), where they are projected to the common polarization directions. The two light beams created by the WP can be detected by a balanced silicon detector of which the balanced output signal is an interferogram with double amplitude and zero offset. The reported resolution is 2.5 nm at the center wavelength of 633 nm.

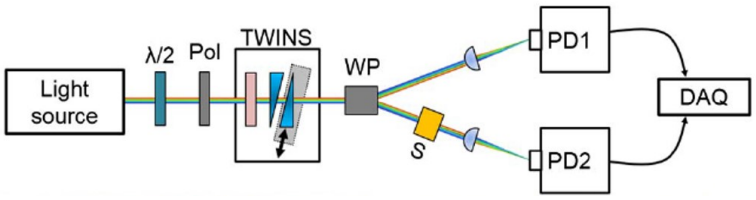

Figure 1.5: Schematic of the birefringent-wedge-based FTS: λ/2, half-wave plate; Pol, polarizer at 45^o with respect to the optical axis of the birefringent material; WP, Wollaston prism; S, sample; PD1 and PD2, photodiodes; DAQ, data acquisition card. Reprinted from [23].

1.2.2 Integrated stationary FTS

Nevertheless, sometimes, it is more attractive to have an FTS without any moving components. Such a stationary FTS should provide better reliabil-

ity and stability. In literature, there are several types of integrated stationary FTS, including the spatial heterodyne spectrometer (SHS) [24–26], the MZI-based FTS that requires the active tuning [27–29], and the stationary wave integrated FTS (SWIFTs) [30, 31].

1.2.2.1 Spatial heterodyne spectrometer

As shown in the scheme in figure 1.6 (a), a typical SHS has an array of channels, each containing an unbalanced Mach-Zehnder interferometer (MZI) that allows light to interfere with its delayed version. As shown in the figure, the OPD increases from channel one to channels N with a fixed increment. The signals measured at the output ports then form a spatially varying stationary interference pattern. As the output ports of the MZI array are located in a line, one can use a photodiode array to record the interferogram.

In this approach, in order to increase the resolution for a given spectral bandwidth, one needs a larger number of channels. This implies a rapidly growing size of the device when scaling the spectral resolution [24]. However, for applications that have fewer constraints on the footprint, SHS can be particularly suitable since the underlying principle allows SHS to achieve high resolution in a narrow spectral band without degrading the signal to noise ratio. As an example, figure 1.6 (b) show a picture of an 8-channel SHS with the size of 8×4 mm^2 fabricated on silicon nitride platform that provides resolution of 0.023 nm in a wavelength range of 0.184 nm centered at 1550 nm [25].

Other than the unbalanced MZI, a waveguide-based Fabry-Pérot (FP) cavity can also work as the interferometer. A waveguide-based FP cavity can be constructed by placing two reflecting metal mirror on the two sides of a waveguide segment. Such a cavity allows for the interference between the forward and backward propagating light. As the OPD equals to twice of the optical length of the cavity, the light with a certain wavelength can have different intensity when coupled out from the FP cavities with different lengths.

Recently, IMEC demonstrated FP-interferometer-based spatial heterodyne spectrometers in their newly developed handheld Raman spectrometer, as shown in figure 1.7.

The patented spatial heterodyne spectrometer has hundreds of FP interferometers placed next to each other [26]. Each interferometer has a little smaller cavity length than the previous one so that an interferogram can be

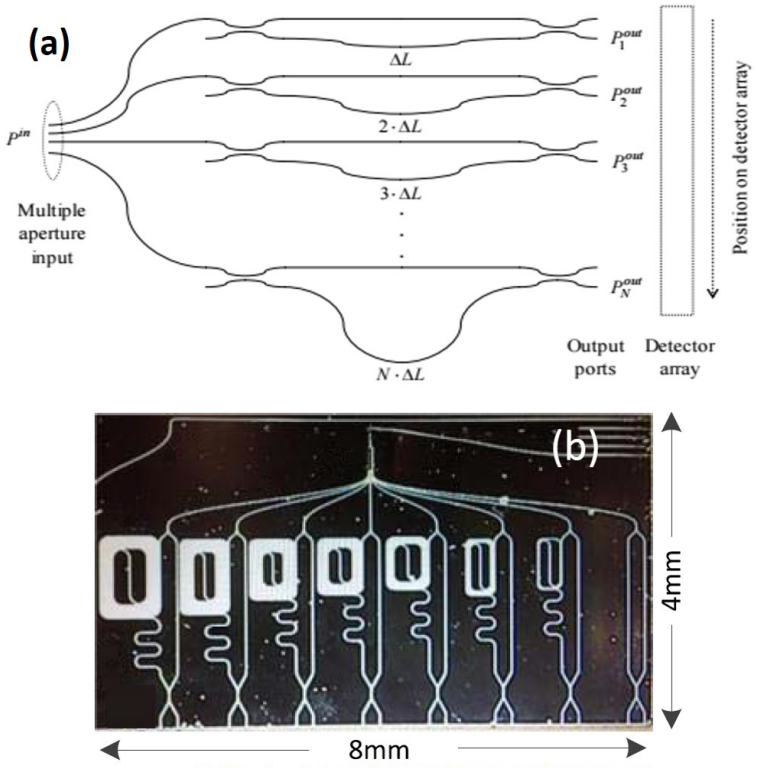

Figure 1.6: (a) A sketch of the SHS constructed with an array of waveguide MZIs. The outputs are spatially distributed to be monitored by a detector array, reprinted from [24]. (b) The picture of a fabricated 8-channel SHS with size of 8 $\times$ 4 mm^2, adapted from [25].

sampled at different OPDs, which can then be used to reconstruct the spectrum. The FP interferometer features extremely small footprint. As a result, it is possible to make massive parallelization (up to a million interferometers on one chip), which allows for eténdue matching in the Raman application. Furthermore, it is reported that the interferometers can be monolithically integrated on top of a CMOS image sensor [32]. By aligning the outputs of the interferometers to the pixels of the integrated CMOS image sensor, all the interferograms can be captured simultaneously by the sensor chip that is wire-bonded to a PCB and connected to a read-out board. The data is then transferred to a computing device for spectrum reconstruction and visualization.

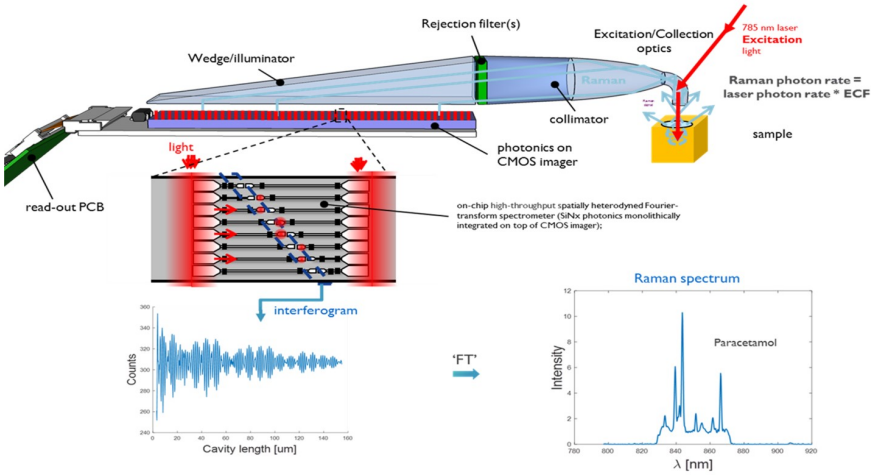

Figure 1.7: conceptual drawing of the handheld Raman spectrometer using a million FP interferometers integrated on top of a CMOS image sensor. The extreme miniaturization and the massive parallelization allow for a large eténdue. Reproduced from [32].

1.2.2.2 MZI-based FTS that requires active tuning

Different from the SHS, one can replace the array of interferometers with a special interferometer that can change its OPD. This could be an MZI with a tunable unbalance a reconfigurable MZI that is enabled by the on-chip optical switches. The former could be a thermally tuned silicon-based integrated FTS. As shown in 1.8, the arms of the MZI are coiled into spirals and covered by independently actuated nichrome microheaters. One can heat the individual arm to introduce different unbalance and thus to obtain a varying interference signal at the output. While it has a small footprint and requires only one detector, its operation requires active tuning and a good handle on the side-effects including the mode dispersion, the thermo-optic non-linearity, and the thermal expansion [27].

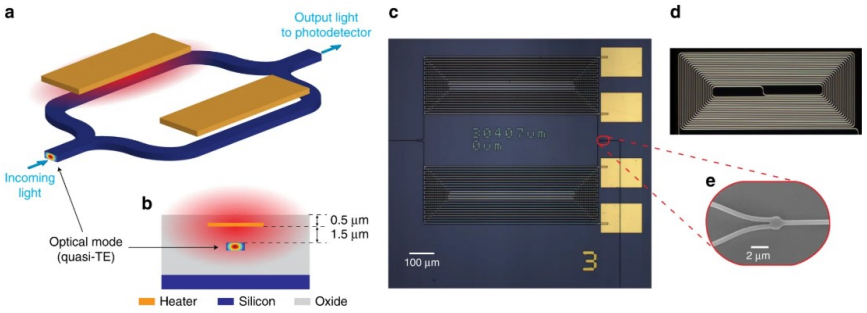

Figure 1.8: Thermal tuning on-chip FTS. (a) Schematic of the tunable MZI. (b) Cross-section showing the waveguide mode and the energy distribution of the heater. (c) Layout of the device. (d) Picture of the MZI arm underneath the heater. (e) SEM picture of broadband power splitter. Reprinted from [27].

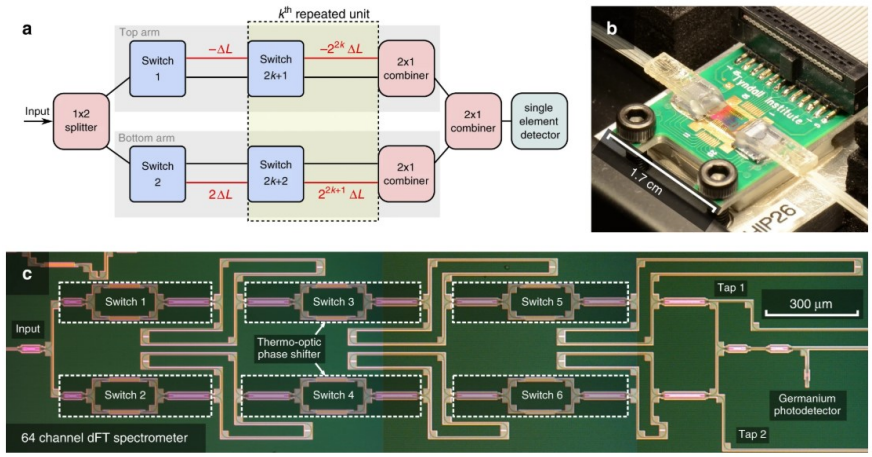

Figure 1.9: Switch-based on-chip FTS. (a) Block diagram of the generic structure of the dFT spectrometer. (b) Picture of fully packaged dFT spectrometer. (c) Layout of the 64-channel dFT spectrometer showing the switches and the detector. Reprinted from [28].

The latter makes use of the reconfigurable MZI as in the example shown in figure 1.9. In this approach, six thermo-optic switches are used to generate 64 permutations, each corresponding to an MZI with a different unbalance. As such, one can sample an interferogram at 64 points with different OPDs. Therefore, the device is referred to as a digital Fourier transform (dFT) spectrometer. It has been demonstrated that with active tuning, such dFT spectrometer could reconstruct the spectra for both sparse and broadband

input signals using a specially designed machine learning regularization algorithm [28, 29].

1.2.2.3 Stationary wave integrated FTS

There is also an on-chip FTS that is implemented in the SWIFTs configuration, which is capable of achieving high resolution within a small footprint. As shown in figure 1.10, in the SWIFTs, the interferogram is generated by two counter-propagating beams inside a waveguide in the form of a standing wave pattern. There are two ways to implement. In the Lippmann configuration, one can put a mirror on one side of the waveguide and injecting a light beam from the other side of the waveguide. In a counterpropagative configuration, light is split into two replicas which are injected into the waveguide from two sides.

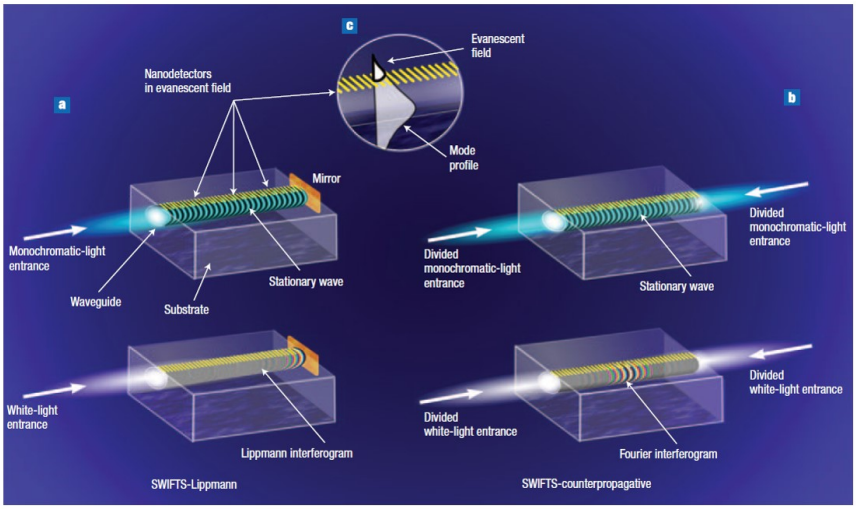

Figure 1.10: An illustration of the principle of the SWIFTs. (a) In the Lippmann configuration, the forward propagating light beam interferes with the backward propagating version generated by the mirror positioned at the end of the waveguides. (b) In the counterpropagative configuration, the light is divided into two copies and injected into a waveguide from two sides, propagating towards each other. (c) A schematic of the near-field detection where the light is scattered from the guided modes to the collection of nano-detectors. Reprinted from [30].

The generated interferogram is sampled by the nano-scatters that are carefully positioned on top of the waveguide. These nano-scatters can scatter the light to a detector array. This type of integrated stationary FTS has the

advantage in that the resolution scales with the length of the waveguide. Therefore, a high resolution does not require a large device size. Nevertheless, the SWIFTs also has its limitation. As introduced in the work of Etienne le Coarer et al. [30], the pitch of the interference pattern (assuming a monochromatic input signal with a wavelength of λ) is expressed as

$$\Lambda = \frac{\lambda}{2n_{eff}} \tag{1.3}$$

where n_{eff} is the effective refractive index of the light propagating in the waveguide. Considering λ of 1550 nm and n_{eff} of 2.3, we can calculate the pitch to be 336 nm, which is much smaller than the pitch size of state-of-the-art photodiode arrays. Therefore, the interferogram has to be subsampled. As introduced in section 1.1.3, the consequence is a limited spectral bandwidth of the FTS.

1.3 Towards on-chip spectroscopic system

An optical spectrometer, such as the Fourier transform spectrometer, is an indispensable instrument for optical spectroscopic systems. Generally speaking, optical spectroscopy is an essential technology that is widely used to study the interaction between light and atoms or molecules in various application fields. Spectroscopic techniques typically have better selectivity as they rely on the detection of the unique spectral ”fingerprint”, while other types of sensor usually measure the chemical affinity of the analytes to a functionalized surface. Based on different underlying principles, spectroscopic techniques, such the absorption spectroscopy, fluorescence spectroscopy, and Raman spectroscopy can provide complementary information which may be used to identify the unknown analytes, to study the structure of nanomaterials and to measure the concentration of a particular chemical. However, modern spectroscopic instruments are often bulky and expensive. This drives the research interests towards the miniaturization and the integration of the spectroscopic system in the form of a chip, which can be massively produced with low cost and provide the possibility for high degree parallelism and multiplexing [33, 34].

One of the most promising integrating technologies is the silicon photonics technology which utilizes the technology of an advanced Complementary Metal–Oxide–Semiconductor (CMOS) fab to fabricate photonic integrated circuits (PICs). As the silicon photonics technology grows in maturity, more and more demonstrations emerge to realize the concepts of different types of on-chip spectroscopic systems [35–37]. Research shows that

the use of photonic chips for the implementation of the integrated spectroscopic system is advantageous not only from the concerns of cost and reliability but also from the concerns of performance [38].

The work of this Ph.D. is also an effort towards the on-chip integrated spectroscopic system. The on-chip integrated FTS, as the main topic of this thesis, functions as the spectrum analyzer and can be useful for various on-chip spectroscopic systems. Other than the on-chip integrated FTS, we also developed some other components that are valuable to the on-chip spectroscopic systems.

1.3.1 On-chip co-propagative stationary FTS

The main topic of this Ph.D. work is to explore a new solution for the on-chip stationary FTS. Our approaches can be classified into the category of stationary-wave integrated FTS as they are inspired initially by the SWIFTs concept. Nevertheless, our approaches differ from the SWIFTs in that we generate the interferogram in a co-propagative manner, where the two light beams interfere with each while propagating in the same direction. As will be discussed in Chapter 2 and 3, this co-propagative configuration allows us to create interferogram that is spatially stretched so that the pitch of the interferogram can be as large as tens of micrometers. As a result, we can sufficiently sample the interferogram with the commercially available photodiode arrays. As the subsampling is avoided, we can obtain a considerably widened operational bandwidth when compared to the original SWIFTs concept. Furthermore, the on-chip stationary FTS we proposed could be realized with CMOS compatible fabrication techniques. This allows it to be integrated onto a CMOS sensor wafer so as to create a fully integrated solution [32]. The original plan was to develop a proof-of-concept demonstration for this approach under the Pix4Life project [39]. While several delays within the Pix4Life project have made the experimental demonstration of the fully integrated approach impossible within the time frame of this Ph.D., we did develop other characterisation methods to show the proof-of-principle demonstration.

1.3.2 On-chip integrated pump-rejection filter

Typically, in the absorption or emission spectroscopy, the signal to be detected is often extremely weak when compared to the light emitted from the source. Particularly in the case of emission spectroscopy, before going

to the spectrometer, light must go through one or more high-performance filters that reject the pump light. For instance, to use an on-chip integrated FTS as the spectral analyzer for on-chip Raman spectroscopy, one can place an on-chip integrated pump rejection filter (often requires around 100 dB extinction ratio) before the on-chip integrated FTS, as shown in figure 1.11. This will help remove the strong pump light, which can otherwise easily saturate the spectrometer and make it difficult to detect the weak Raman signal.

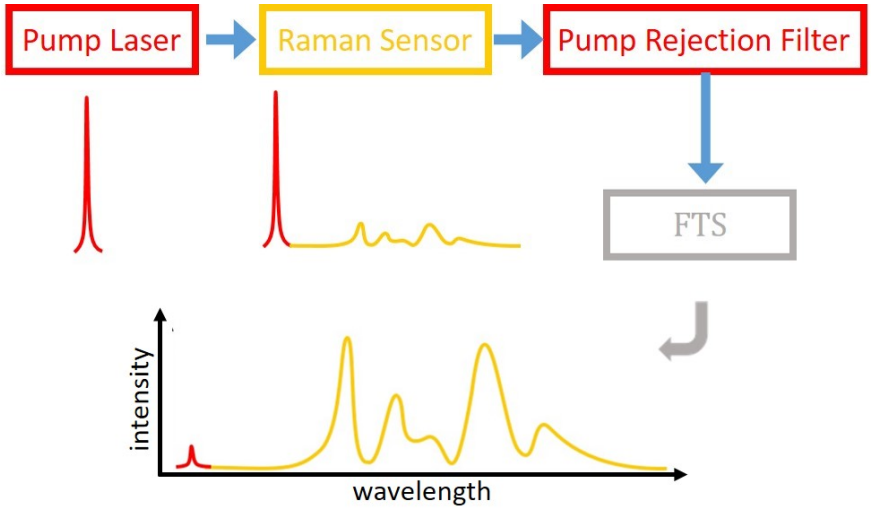

Figure 1.11: A sketch to illustrate the need for an on-chip pump rejection filter in the on-chip Raman system with on-chip FTS as the spectrum analyzer. The pump (red) is usually more than 100 dB stronger than the Raman signals (yellow).

As part of the work in this Ph.D. project, an on-chip integrated filter based on the grating-assisted contra-directional coupler (GACDC) is developed. As will be introduced later, the GACDC filter can be efficiently cascaded to provide a very high extinction ratio at the desired wavelength. Another advantage of the GACDC filter is the capability of coupling the rejected light contra-directionally into a bus waveguide. This prevents the rejected light from going back to the input, which can degrade the performance of the on-chip laser unless one can also integrate an on-chip circulator. Moreover, the GACDC filter is advantageous in that it has an unlimited Free Spectral Range (FSR) on the long-wavelength side of the stop/pass band. It is essential that, for applications such as the on-chip Raman spectroscopic systems, the pump rejection filter should have not only an extremely high extinction ratio at the pump wavelength but also a flat spectral response in the wave-

length range where the Raman Stokes signals are generated. In chapter 4, we will discuss this filter in detail.

1.3.3 On-chip temperature-insensitive filter

As an essential component of the on-chip spectroscopic system, the on-chip integrated spectrometer is often required to be spectrally stable to the change of environmental parameters such as pressure, temperature, humidity, etc. The environmental parameter, in most of the case the temperature, can impact the waveguides by changing the effective indices of the guided modes, leading to an unwanted shift in the spectral response of the waveguide-based spectrometer. It is therefore necessary to calibrate the spectrometer with one or more spectral references that do not shift with temperature variation. This can be done with the integrated temperature-insensitive filters.

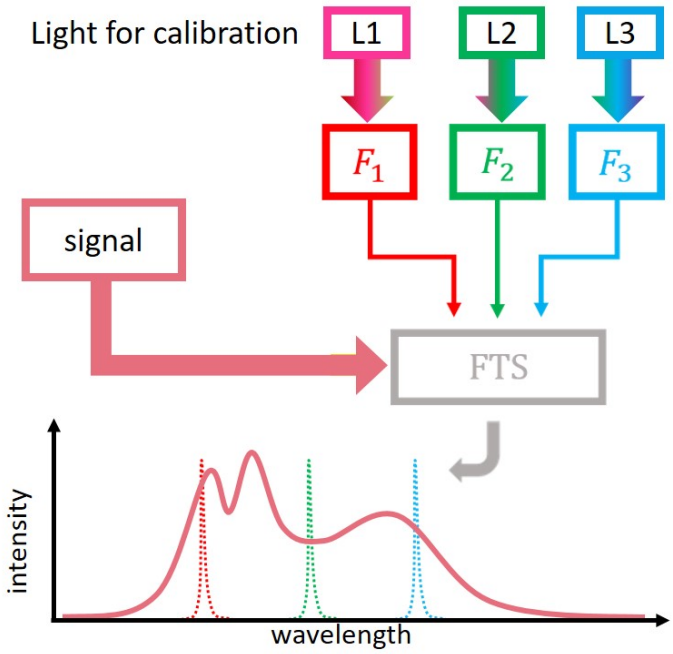

Figure 1.12: A sketch to illustrate the need for an on-chip temperature-insensitive filters in the operation of an on-chip spectrometer. As an example, three athermal filters (F_1, F_2 and F_3) together with three on-chip light source (L_1, L_2 and L_3) are used to provide three fixed reference wavelengths which allow the wavelength calibration of the on-chip FTS under different environmental temperature.

In calibration, we feed several fixed reference wavelengths to the on-chip FTS. While the readings from the waveguides-based spectrometer are still temperature dependent, we can find the correct mapping factors that allow us to match the wavelength readings to the known reference wavelengths. In some cases, the mapping factor could vary with wavelength even in a nonlinear manner (as discussed in section 2.2.3). Therefore, it is preferable to have at least three such athermal wavelength references, as shown in figure 1.12 for example. After calibration, we can then measure the signal, and use the same mapping factors to correctly determine the spectral contents of the signal. In this Ph.D. thesis, we explored a novel approach to implement an on-chip temperature-insensitive filter, where both the thermo-optic effect and thermal expansion effect are carefully compensated. Chapter 5 is dedicated to the work related to this on-chip temperature-insensitive filter.

1.4 Silicon nitride platform for near infrared biosensing applications

For most of the work in this Ph.D. project, we consider a silicon nitride (SiN) platform. Recently, It has become a prominent platform for integrated on-chip spectroscopic systems that utilize miniaturized photonic circuits and components [40–42]. Like the well-established silicon-on-insulator (SOI) technology, SiN nanophotonics is also a CMOS-compatible technology that leverages the already existing CMOS facilities for large-scale, cost-effective fabrication of photonic integrated circuits. Several promising characteristics of SiN platform as listed below attract more and more attention from both the academic field and the industrial field, leading to its booming in various applications [43–45].

- **Transparency below 1** μm The fact that SiN is transparent below 1 μm makes it applicable for spectroscopic systems that operate in the near infrared (NIR, 0.7-1.0 μm) [46]. Compared to the short-wave infrared (SWIR, 1.0-3.0 μm) wavelengths or the mid-wave infrared (MWIR, 3.0-5.0 μm) wavelengths, NIR range is suitable for biosensing applications as there are minimal photo-damage to the cells or bio-tissues, negligible water absorption and abundance of light source as well as detectors with high performance and low cost.
- **Various deposition possibilities** SiN can be deposited on silicon oxide by Low-Pressure Chemical Vapour Deposition (LPCVD) at high temperature ($>$700 °C) or by Plasma Enhanced Chemical Vapour

Deposition (PECVD) at low temperature (<400 °C) [40]. Although LPCVD SiN suffers from large internal tensile stress [47], it has the advantage of good homogeneity of material index and thickness since the silicon nitride is approximately stoichiometric. LPCVD SiN, after annealed at high temperature, is often used in the telecommunication band around 1.55 μm to avoid the absorption induced by N-H and Si-H bonds [48]. On the other hand, depending on the different deposition conditions, PECVD-based nitride can either by Si-rich (higher refractive index) or nitrogen-rich (lower refractive index). This low-temperature process creates more possibilities when SiN waveguides need to be combined with other photonic structures. For instance, to increase the coupling efficiency of a SiN grating coupler (GC), one can deposit the waveguide layer on top of a DBR-mirror or a metal mirror [49, 50].

- **Moderately high index contrast** SiN has material refractive index of around 2, as shown in figure 1.13 for different deposition techniques. As a result, SiN can provide moderately high index contrast between the waveguide core and cladding. It is, however, lower than that of an SOI platform. The consequence is that the waveguide effective refractive index varies relatively little for a given dimensional variation due to fabrication imperfections. This helps reduce the propagation loss and phase noise. For instance, in a SiN rib waveguide, losses lower than 1 dB/cm can be regularly achieved [50]. A decreased phase noise typically leads to a lower channel cross-talk and a better SNR for the integrated dispersive spectrometer. Moreover, a reduced index contrast also helps reduce the magnitude of the spurious reflections that come from an abrupt index mismatch due to varying waveguide dimensions. This can also improve the performance of integrated spectrometers.

- **Small thermo-optic coefficient** SiN possesses a thermo-optic coefficient (TOC) that is almost one order of magnitude lower than that of silicon. For example, at a wavelength of 1550 nm, the TOC is around 2.45×10^{-5} K^{-1} for LPCVD SiN or around 2.51×10^{-5} K^{-1} for PECVD type, whereas the silicon has a TOC of around 1.86×10^{-4} K^{-1} [46, 51]. As a result, a lower spectral drift can be expected under a given variation in the temperature.

In this thesis, most of the work is done on the SiN waveguide platform that is deposited with PECVD. Also, as we are interested in the spectroscopic devices for bio-sensing related applications, the majority of the designs, as

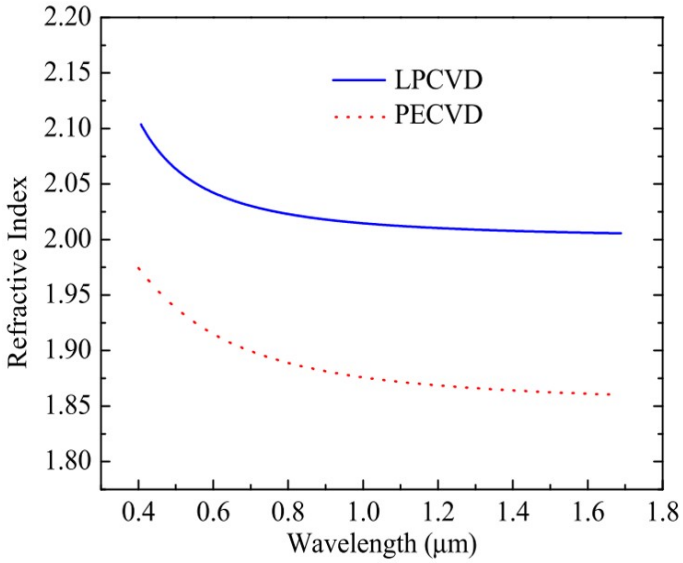

Figure 1.13: Refractive index plotted as a function of wavelength for typical LPCVD and PECVD SiN, reproduced from [46].

will be introduced in the following chapters, are focused on the operation in the NIR wavelength range.

1.5 Outline of the thesis

The thesis is organized as follows. The theory behind the proposed new type of on-chip integrated stationary FTS is introduced in Chapter 2, together with the design concerns and details. In Chapter 3, we will present the characterization methods and discuss the corresponding experimental results. After that, we will talk about the work related to the on-chip pump rejection filter in Chapter 4, introducing the underlying principle, discussing the design details, and presenting the experimental results. Chapter 5 is dedicated to the work done for the on-chip temperature-insensitive filter. Finally, conclusions and perspectives are given in Chapter 6.

1.6 Publications

1.6.1 Publications in international journals

1. **X. Nie**, N. Turk, Y. Li, Z. Liu, R. Baets, "High extinction ratio on-chip pump-rejection filter based on cascaded grating-assisted contra-directional couplers in silicon nitride rib waveguides", Optics Letters, 44(9), p. 2310-2313 (2019).

2. **X. Nie**, E. M. P. Ryckeboer, G. Roelkens, R. Baets, "CMOS compatible broadband co-propagative stationary Fourier transform spectrometer integrated on a silicon nitride photonics platform", Optics Express, 25 (8), p. A409-A418 (2017).

1.6.2 Patents

1. R. Baets, E. Ryckeboer, A. Rahim, A. Vasiliev, **X. Nie**, "Temperature insensitive filter", WO/2019/129798 (A1) (2019).

2. R. Baets, G. Roelkens, E. Ryckeboer, **X. Nie**, "Stationary wave integrated FTS with broadband operation using lateral leakage", (*patent in filing*).

1.6.3 Publications in international conferences

1. **X. Nie**, N. Turk, Z. Liu, R. Baets, "Grating assisted contra-directional filters with high rejection ratio in silicon nitride rib waveguides", European Conference on Integrated Optics (ECIO 2019), Belgium, p.T.Po2.11 (2019).

2. E. M. P. Ryckeboer, **X. Nie**, A. Dhakal, D. Martens, P. Bienstman, G. Roelkens, R. Baets, "Spectroscopic sensing and applications in Silicon Photonics", International Conference on Group IV Photonics (invited), Germany, p.81-82 (2017).

3. **X. Nie**, E. M. P. Ryckeboer, R. Baets, "Broadband stationary fourier transform spectrometer integrated on a silicon nitride photonics platform", OSA topical meetings: Light, Energy and the Environment Congress (invited), Germany, p.paper FTh2C1 (2016).

4. **X. Nie**, E. M. P. Ryckeboer, G. Roelkens, R. Baets, "Novel Concept for a Broadband Co-propagative Stationary Fourier Transform Spectrometer Integrated on a Si3N4 Waveguide Platform", Conference on Lasers and Electro-Optics (CLEO) 2016, United States, (2016).

5. E. M. P. Ryckeboer, **X. Nie**, A. Subramanian, D. Martens, P. Bienstman, S. Clemmen, S. Severi, R. Jansen, G. Roelkens, R. Baets, "CMOS-compatible silicon nitride spectrometers for lab-on-a-chip spectral sensing", Photonics Europe 2016, Proc. SPIE 9891, Silicon Photonics and Photonic Integrated Circuits V, 98911K (invited), Belgium, (2016).

1.6.4 Publications in national conferences

1. P. C. Wuytens, A. Raza, H. Zhao, N. Turk, F. Peyskens, **X. Nie**, A. Dhakal, E.M.P. Ryckeboer, S. Clemmen, N. Le Thomas, R. Baets, "On-chip Raman Spectroscopy", FEA Research Syposium 2017, Belgium, (2017).

References

[1] Peter R Griffiths and James A De Haseth. *Fourier transform infrared spectrometry*, volume 171. John Wiley & Sons, 2007.

[2] Sumner P Davis, Mark C Abrams, and James W Brault. *Fourier transform spectrometry*. Elsevier, 2001.

[3] MJ Persky. *A review of spaceborne infrared Fourier transform spectrometers for remote sensing*. Review of Scientific Instruments, 66(10):4763–4797, 1995.

[4] Janine Connes and Pierre Connes. *Near-infrared planetary spectra by Fourier spectroscopy. I. Instruments and results*. JOSA, 56(7):896–910, 1966.

[5] John G Proakis. *Digital signal processing: principles algorithms and applications*. Pearson Education India, 2001.

[6] D Helm, H Labischinski, Gisela Schallehn, and D Naumann. *Classification and identification of bacteria by Fourier-transform infrared spectroscopy*. Microbiology, 137(1):69–79, 1991.

[7] Joshua Manor, Esther S Feldblum, Martin T Zanni, and Isaiah T Arkin. *Environment polarity in proteins mapped noninvasively by FTIR spectroscopy*. The journal of physical chemistry letters, 3(7):939–944, 2012.

[8] Zanyar Movasaghi, Shazza Rehman, and Dr Ihtesham ur Rehman. *Fourier transform infrared (FTIR) spectroscopy of biological tissues*. Applied Spectroscopy Reviews, 43(2):134–179, 2008.

[9] Richard R Ernst and Weston A Anderson. *Application of Fourier transform spectroscopy to magnetic resonance*. Review of Scientific Instruments, 37(1):93–102, 1966.

[10] Alan G Marshall, Christopher L Hendrickson, and George S Jackson. *Fourier transform ion cyclotron resonance mass spectrometry: a primer*. Mass spectrometry reviews, 17(1):1–35, 1998.

[11] Pierre Connes. *Astronomical fourier spectroscopy*. Annual Review of Astronomy and Astrophysics, 8(1):209–230, 1970.

[12] Pradip Gatkine, Sylvain Veilleux, and Mario Dagenais. *Astrophotonic Spectrographs*. Applied Sciences, 9(2):290, 2019.

[13] V Formisano, F Angrilli, G Arnold, S Atreya, G Bianchini, D Biondi, A Blanco, MI Blecka, A Coradini, L Colangeli, et al. *The planetary Fourier spectrometer (PFS) onboard the European Mars Express mission*. Planetary and Space Science, 53(10):963–974, 2005.

[14] Chris D Boone, Ray Nassar, Kaley A Walker, Yves Rochon, Sean D McLeod, Curtis P Rinsland, and Peter F Bernath. *Retrievals for the atmospheric chemistry experiment Fourier-transform spectrometer*. Applied Optics, 44(33):7218–7231, 2005.

[15] PB Fellgett. *On the ultimate sensitivity and practical performance of radiation detectors*. JOSA, 39(11):970–976, 1949.

[16] PY Han, M Tani, M Usami, S Kono, R Kersting, and X-C Zhang. *A direct comparison between terahertz time-domain spectroscopy and far-infrared Fourier transform spectroscopy*. Journal of Applied Physics, 89(4):2357–2359, 2001.

[17] Johannes F De Boer, Barry Cense, B Hyle Park, Mark C Pierce, Guillermo J Tearney, and Brett E Bouma. *Improved signal-to-noise ratio in spectral-domain compared with time-domain optical coherence tomography*. Optics letters, 28(21):2067–2069, 2003.

[18] Pierre Jacquinot. *New developments in interference spectroscopy*. Reports on progress in physics, 23(1):267, 1960.

[19] Vidi Saptari. *Fourier transform spectroscopy instrumentation engineering*, volume 61. SPIE press, 2004.

[20] Thilo Sandner, Andreas Kenda, Christian Drabe, Harald Schenk, and Werner Scherf. *Miniaturized FTIR-spectrometer based on optical MEMS translatory actuator*. In MOEMS and miniaturized systems VI, volume 6466, page 646602. International Society for Optics and Photonics, 2007.

[21] Omar Manzardo, Hans Peter Herzig, Cornel R Marxer, and Nico F de Rooij. *Miniaturized time-scanning Fourier transform spectrometer based on silicon technology*. Optics letters, 24(23):1705–1707, 1999.

[22] Wei Wang, Jiapin Chen, Aleksandar S Zivkovic, Quentin AA Tanguy, and Huikai Xie. *A compact Fourier transform spectrometer on a silicon optical bench with an electrothermal MEMS mirror*. Journal of Microelectromechanical Systems, 25(2):347–355, 2016.

[23] Aurelio Oriana, Julien Réhault, Fabrizio Preda, Dario Polli, and Giulio Cerullo. *Scanning Fourier transform spectrometer in the visible range based on birefringent wedges*. JOSA A, 33(7):1415–1420, 2016.

[24] Mirosław Florjańczyk, Pavel Cheben, Siegfried Janz, Alan Scott, Brian Solheim, and Dan-Xia Xu. *Planar waveguide spatial heterodyne spectrometer*. In Photonics North 2007, volume 6796, page 67963J. International Society for Optics and Photonics, 2007.

[25] Yu Li, Hongchen Yu, Le An, Qiang Guo, Minghua Chen, Hongwei Chen, Sigang Yang, and Shizhong Xie. *CMOS-Compatible High Resolution Spatial Heterodyne Spectrometer Based on Si 3 N 4/SiO 2 Waveguide*. IEEE Photonics Technology Letters, 28(23):2712–2715, 2016.

[26] Pol Van Dorpe and Peter Peumans. *Optical spectrometer with matched étendue*, March 6 2018. US Patent 9,909,992.

[27] Mario CMM Souza, Andrew Grieco, Newton C Frateschi, and Yeshaiahu Fainman. *Fourier transform spectrometer on silicon with thermo-optic non-linearity and dispersion correction*. Nature communications, 9(1):665, 2018.

[28] Derek M Kita, Brando Miranda, David Favela, David Bono, Jérôme Michon, Hongtao Lin, Tian Gu, and Juejun Hu. *High-performance and scalable on-chip digital Fourier transform spectroscopy*. Nature communications, 9(1):4405, 2018.

[29] Fabio Pavanello, Anton Vasiliev, Muhammad Muneeb, and Günther Roelkens. *Broadband Digital Fourier Transform Spectrometer for On-Chip Wavelength Monitoring in the 2.3-μ m Wavelength Range*. IEEE Photonics Journal, 11(3):1–9, 2019.

[30] Etienne Le Coarer, Sylvain Blaize, Pierre Benech, Ilan Stefanon, Alain Morand, Gilles Lérondel, Grégory Leblond, Pierre Kern, Jean Marc Fedeli, and Pascal Royer. *Wavelength-scale stationary-wave integrated Fourier-transform spectrometry*. Nature Photonics, 1(8):473, 2007.

[31] E Le Coarer, LG Venancio, P Kern, J Ferrand, P Puget, M Ayraud, C Bonneville, B Demonte, A Morand, J Boussey, et al. *Swifts: On-chip very high spectral resolution spectrometer*. In International Conference on Space Optics—ICSO 2010, volume 10565, page 105651B. International Society for Optics and Photonics, 2017.

[32] *How to shrink a Raman spectroscope and analyze complex samples on-the-go*. https://www.imec-int.com/en/imec-magazine/imec-magazine-june-2019/how-to-shrink-a-raman-spectroscope-and-analyze-complex-samples-on-the-go. Accessed: 2019-09-09.

[33] Babak Momeni, Siva Yegnanarayanan, Mohammad Soltani, Ali Asghar Eftekhar, Ehsan Shah Hosseini, and Ali Adibi. *Silicon nanophotonic devices for integrated sensing*. Journal of Nanophotonics, 3(1):031001, 2009.

[34] Jorg Hubner, Anders Michael Jorgensen, Thomas A Anhoj, and Dan A Zauner. *Integrated optical systems for lab-on-a-chip applications*. In Integrated Optics: Devices, Materials, and Technologies IX, volume 5728, pages 269–278. International Society for Optics and Photonics, 2005.

[35] Arthur Nitkowski, Long Chen, and Michal Lipson. *Cavity-enhanced on-chip absorption spectroscopy using microring resonators*. Optics express, 16(16):11930–11936, 2008.

[36] Lionel Tombez, EJ Zhang, JS Orcutt, Swetha Kamlapurkar, and WMJ Green. *Methane absorption spectroscopy on a silicon photonic chip*. Optica, 4(11):1322–1325, 2017.

[37] Eva Ryckeboer, Ronny Bockstaele, Michaël Vanslembrouck, and Roel Baets. *Glucose sensing by waveguide-based absorption spectroscopy on a silicon chip*. Biomedical optics express, 5(5):1636–1648, 2014.

[38] Roel Baets, Ananth Z Subramanian, Ashim Dhakal, Shankar K Selvaraja, Katarzyna Komorowska, Frédéric Peyskens, Eva Ryckeboer, Nebiyu Yebo, Günther Roelkens, and Nicolas Le Thomas. *Spectroscopy-on-chip applications of silicon photonics*. In Integrated optics: Devices, materials, and technologies XVII, volume 8627, page 86270I. International Society for Optics and Photonics, 2013.

[39] Pix4Life. *European Pilot line for supporting life science and biomedical applications on silicon nitride-based photonic integrated platforms*. https://www.pix4life.eu/. Accessed: 2019-09-09.

[40] AZ Subramanian, Pieter Neutens, Ashim Dhakal, Roelof Jansen, Tom Claes, Xavier Rottenberg, Frédéric Peyskens, Shankar Selvaraja,

Philippe Helin, Bert Du Bois, et al. *Low-loss singlemode PECVD silicon nitride photonic wire waveguides for 532–900 nm wavelength window fabricated within a CMOS pilot line*. IEEE Photonics Journal, 5(6):2202809–2202809, 2013.

[41] X Sun, MZ Alam, JS Aitchison, and M Mojahedi. *Compact and broadband polarization beam splitter based on a silicon nitride augmented low-index guiding structure*. Optics letters, 41(1):163–166, 2016.

[42] Daoxin Dai, Zhi Wang, Jared F Bauters, M-C Tien, Martijn JR Heck, Daniel J Blumenthal, and John E Bowers. *Low-loss Si3N4 arrayed-waveguide grating (de) multiplexer using nano-core optical waveguides*. Optics express, 19(15):14130–14136, 2011.

[43] Ashim Dhakal, Ananth Z Subramanian, Pieter Wuytens, Frédéric Peyskens, Nicolas Le Thomas, and Roel Baets. *Evanescent excitation and collection of spontaneous Raman spectra using silicon nitride nanophotonic waveguides*. Optics letters, 39(13):4025–4028, 2014.

[44] Yoav Zuta, Ilya Goykhman, Boris Desiatov, and Uriel Levy. *On-chip switching of a silicon nitride micro-ring resonator based on digital microfluidics platform*. Optics Express, 18(24):24762–24769, 2010.

[45] Sven Ramelow, Alessandro Farsi, Stéphane Clemmen, Daniel Orquiza, Kevin Luke, Michal Lipson, and Alexander L Gaeta. *Silicon-nitride platform for narrowband entangled photon generation*. arXiv preprint arXiv:1508.04358, 2015.

[46] Abdul Rahim, Eva Ryckeboer, Ananth Z Subramanian, Stéphane Clemmen, Bart Kuyken, Ashim Dhakal, Ali Raza, Artur Hermans, Muhammad Muneeb, Sören Dhoore, et al. *Expanding the silicon photonics portfolio with silicon nitride photonic integrated circuits*. Journal of Lightwave Technology, 35(4):639–649, 2017.

[47] Jacob S Levy, Alexander Gondarenko, Mark A Foster, Amy C Turner-Foster, Alexander L Gaeta, and Michal Lipson. *CMOS-compatible multiple-wavelength oscillator for on-chip optical interconnects*. Nature photonics, 4(1):37, 2010.

[48] Rene M De Ridder, K Warhoff, Alfred Driessen, Paul V Lambeck, and Hans Albers. *Silicon oxynitride planar waveguiding structures for application in optical communication*. IEEE Journal of selected topics in quantum electronics, 4(6):930–937, 1998.

[49] Sebastian Romero-García, Florian Merget, Frank Zhong, Hod Finkelstein, and Jeremy Witzens. *Visible wavelength silicon nitride focusing grating coupler with AlCu/TiN reflector*. Optics letters, 38(14):2521–2523, 2013.

[50] Ananth Z Subramanian, Shankar Selvaraja, Peter Verheyen, Ashim Dhakal, Katarzyna Komorowska, and Roel Baets. *Near-infrared grating couplers for silicon nitride photonic wires*. IEEE Photonics Technology Letters, 24(19):1700–1703, 2012.

[51] Ali W Elshaari, Iman Esmaeil Zadeh, Klaus D Jöns, and Val Zwiller. *Thermo-optic characterization of silicon nitride resonators for cryogenic photonic circuits*. IEEE Photonics Journal, 8(3):1–9, 2016.

2

On-chip Co-propagative Stationary Fourier Transform Spectrometer: Principles and Designs

This chapter covers the main topic of this Ph.D. research, the on-chip integrated co-propagative stationary Fourier transform spectrometer. The focus of this chapter is on the working principles and the critical design parameters. Ref. [1–3] are own publications on this research topic.

Contents

2.1 Introduction

Essentially, a Fourier transform spectrometer (FTS) executes the tasks of generating, recording, and analyzing the interference pattern, or the interferogram. While the analysis approach can be similar, significant differences arise in the way a particular type of FTS generates and records the interferogram. The interferogram can be generated in a scanning manner as in the traditional FTS where a moving mirror is used to create an optical path difference (OPD) and generate an interference pattern. It can also be generated without utilizing the movable component as in the stationary FTS introduced in Chapter 1.

Inspired by the work of [4], our proposed on-chip integrated FTS can be classified into the category of stationary-wave integrated FTS (SWIFTs). Nevertheless, our approaches differ from the SWIFTs concept in that we generate the interferogram in a co-propagative manner. As will become clear later, this allows us to create an interferogram that is spatially stretched compared to the one generated in the original SWIFTs concept. As a result, we can avoid the limitation of sub-sampling, which is inevitable in the original SWIFTs and limits the operational bandwidth.

The co-propagative stationary FTS has two different types, as their ways of generating the interferogram are slightly different from each other. In the following sections, we will successively introduce their basic principle and discuss the design details.

2.2 Evanescent-scattering-based co-propagative stationary FTS

Light confined in an optical waveguide can propagate in the form of guided modes with the phase velocity determined by the geometry and the material properties of the waveguide. For a guided mode, there is an associated effective refractive index that describes how fast the phase velocity is when compared to the light speed in vacuum.

In the first type of co-propagative stationary FTS, light is injected into two parallel single-mode waveguides that have different widths. Due to the different waveguide geometry, the guided modes (for example, the fundamental TE-like modes) in the two waveguides will have different effective refractive indices and propagate at different phase velocities. This means that, after the same propagation distance, the two modes experience a dif-

ferent optical delay. Along propagating, the optical path difference (OPD) between the two modes increases with the propagation distance. As the two waveguides are positioned close to each other, the evanescent tails of the two waveguide modes can overlap slightly and interfere with each other, creating an interferogram in the region between the two parallel waveguides.

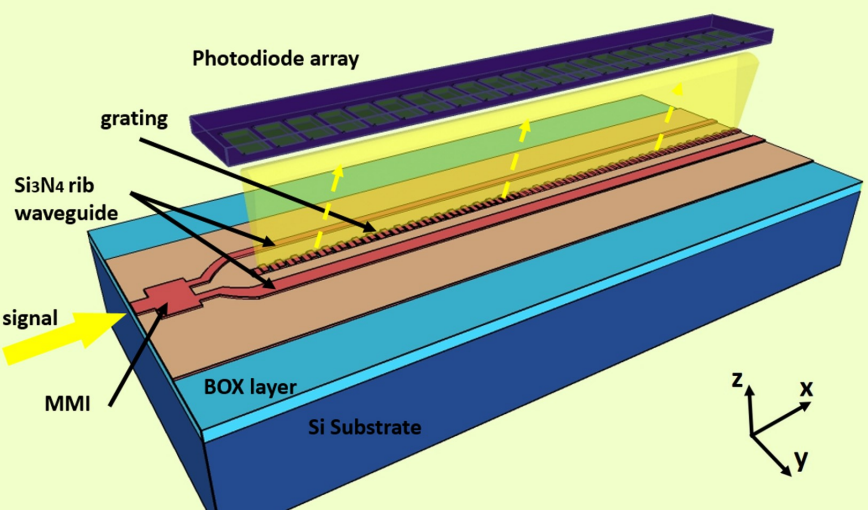

Figure 2.1: A conceptual drawing of the co-propagative stationary FTS. Adapted from Ref. [1]

In figure 2.1, we show a 3D representation of the evanescent scattering based co-propagative stationary FTS. The signal to be analyzed is first injected into the input port of a Multi-Mode Interference (MMI) coupler, which then splits the light into two parallel waveguides with different widths. At the location where the interferogram is expected to have the best contrast, a well-designed grating with a proper period is positioned in order to scatter the interferogram upwards onto the detection system, for example, a photodiode array.

2.2.1 Resolution and bandwidth

To quantitatively discuss the performance, we consider the injection of a monochromatic signal with a wavelength of λ. The intensity distribution of the interferogram I as a function of propagation distance x can be related

to the optical intensity in the overlap region as

$$I(x) \propto I_1 + I_2 + 2\sqrt{I_1 I_2}\cos(\Delta\beta x), \tag{2.1}$$

where I_1 and I_2 are the intensity of waveguide modes in the overlap region and $\Delta\beta$ is the propagation constant difference, which can be written as

$$\Delta\beta = \beta_1 - \beta_2 \approx 2\pi\frac{\Delta n_{eff}}{\lambda}, \tag{2.2}$$

with Δn_{eff} the difference between the effective refractive indices of the two guided modes. As one can see from equation 2.1, the interferogram of a monochromatic signal is a sinusoidal pattern with a period of

$$\Lambda = \frac{\lambda}{\Delta n_{eff}}. \tag{2.3}$$

If one compares this expression to the one in the original SWIFTs [4], one can find that the period is stretched by a factor of $2n_{eff}/\Delta n_{eff}$.

One of the critical characteristics of the FTS is the spectral resolution. Before discussing the spectral resolution, we need to first define some terms in order to clarify the discussion. An interferogram has a zero OPD point where the phase of the two light beams that interfere with each other are equal (ϕ_1-ϕ_2=0). The interferogram extends on both sides of the zero OPD point. We refer to the side where ϕ_1-ϕ_2 $<$0 as the negative OPD part of the interferogram and call the side where ϕ_1-ϕ_2 $>$0 the positive OPD side. When the negative OPD part has the same length of the positive OPD part, the interferogram is referred to as a double-sided interferogram and when an interferogram has a much longer positive part, we called it a single-sided one [5]. When an interferogram has no negative OPD part, it is named one-sided. In our co-propagative stationary FTS, the recorded interferogram is such a one-sided interferogram. We use Fast Fourier transform (FFT) algorithm to calculate the Discrete Fourier transform (DFT) of the obtained interferogram, which is an array of real numbers. The output of the FFT is usually an array of complex numbers. Unless otherwise mentioned, we take the absolute values of the complex array as the spectrum. The terminology defined here will be used throughout this and the next chapter. In our case, the spectral resolution is determined by the length of the one-sided interferogram that we can capture. To give the expression of the resolution, we consider a single wavelength injection. The fact that the interferogram we can measure only covers a finite length L will broaden the delta-shaped peak in the Fourier domain into a sinc line shape, sinc$[\pi(f_x - 1/\Lambda)L]$,

where f_x is the spatial frequency. We define the spectral resolution as the Full Width Half Maximum (FWHM) of the sinc shape spectrum, which can be expressed by:

$$\delta\lambda \approx 1.207\frac{\lambda^2}{\Delta n_{eff} L}. \tag{2.4}$$

It is noteworthy that, in principle, one can obtain higher spectral resolution through additional data processing [6]. In order to not deviate from the central theme of this chapter, we will come back to this in the next chapter, and for now, we stick to the resolution as defined by equation 2.4 in the following discussions. To give an example, we can assume an effective index difference of 0.05 at a wavelength of 800 nm, which is practical in a SiN rib waveguide platform, and consider an interferogram of 1 cm long. According to equation 2.4, we can expect a spectral resolution of 1.28 nm. Even higher resolution can be obtained by making the waveguide and the grating longer and thus recording an interferogram with a larger length.

Although equation 2.4 gives the achievable spectral resolution, other factors can lower the resolution in practice. For instance, due to waveguide losses and the fact that we use grating to couple power to the detector, an exponential decay will be superimposed on the interferogram, which leads to further line broadening and a lower resolution. In principle, this exponential decay can be partially compensated by designing a grating with increasing strength as well as by post data processing.

Another characteristic is the operational spectral range. We can insert the assumed effective index difference of 0.05 and the wavelength λ=800 nm into equation 2.3 and get the calculated period Λ=16 μm. According to the Nyquist-Shannon's sampling theorem, to avoid subsampling we should sample the interferogram with a sample step-length below 8 μm, which can be done with the photodiode arrays that are commercially available and have pixel pitch down to 5 μm. Without the bandwidth limitation set by subsampling, the remaining factors that limit the bandwidth are the operation wavelength range of the detectors, the bandwidth of the grating and the spectral range where the waveguides remain single-mode. These usually indicate a bandwidth of a few hundreds of nanometers in the implementation on the silicon nitride (SiN) platform. We will discuss these limitations in details in the next chapter, where we present the measurement results.

2.2.2 Design details

As the operation of the co-propagative stationary FTS relies on the interference between the evanescent fields of the two waveguide modes, it is beneficial to use rib waveguides to realize the design. Typically, in a rib waveguide, the modes are less confined, and therefore the evanescent field can extend further when compared to that in a wire waveguide. After choosing the rib waveguide platform, we still need to determine a few things, as listed below, for the design of the co-propagative stationary FTS.

- **The widths of the two waveguides** The widths of the narrow and the wide waveguide, w_n and w_w respectively, will determine the difference of effective refractive index of the two modes considered. As introduced before, a large difference of effective refractive indices will lead to a higher resolution but also a small pattern period, according to equation 2.4 and equation 2.3. The choice of w_n and w_w should make sure we get the high resolution under the condition that the pattern period is large enough for sufficient sampling. Additionally, precaution should be taken to avoid the high order modes in the operational wavelength range.

- **The length of the waveguide (or the grating)** This length L determines the length of the interferogram, which, together with a given Δn_{eff}, tells us the resolution. To design a co-propagative stationary FTS with high resolution, it is always good to have a large L.

- **The position of the grating** To record the interferogram with the best contrast, the grating should be positioned at the region where the optical intensity of the evanescent fields of both waveguide modes has the same strength. As an example, we assume a monochromatic input signal and simulate the optical intensity distribution in the region between the two waveguides. The simulated intensity distribution (in top view) is shown in figure 2.2 (a), where the distance starts from the edge of the wide waveguide and ends at the edge of the narrow waveguide. The blue frame in figure 2.2(a) indicates the region where the interference pattern has the best contrast. As this region is not in the exact middle of the two waveguides, the grating should also be positioned off the mid-line shifting to the side of the wide waveguide. We use the distance between the grating and the narrow and wide waveguides, d_{gn} and d_{gw} to describe the relative position of the grating.

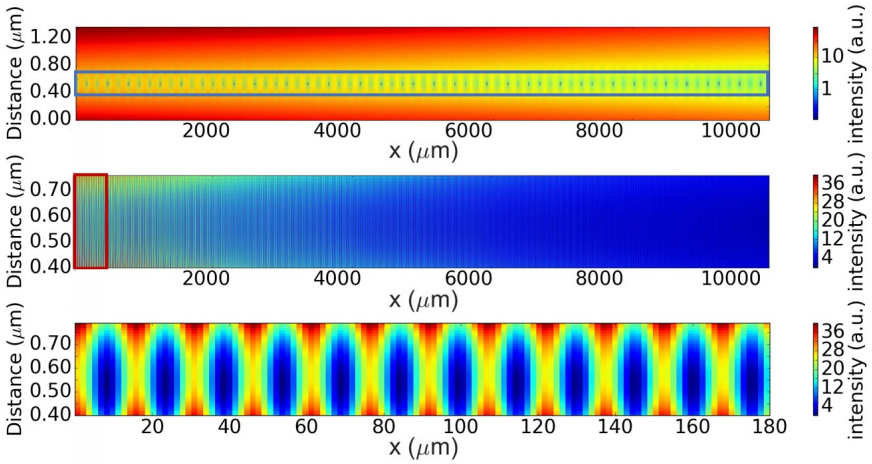

Figure 2.2: (a) The simulated interference pattern between the two waveguides in the case of the single wavelength injection. The blue frame marks the position where one should put the grating as the contrast is the best. (b) A zoom-in of the intensity distribution of the interferogram in the grating region. (c) A zoom-in of the first several periods of the intensity oscillation. Adapted from Ref. [1].

- **The efficiency of the evanescent scattering** The grating serves the purpose of diffracting the interferogram to the recording system. This means that the grating units will constantly couple out the optical power from the guided modes confined in the waveguides through evanescent scattering. Due to the scattering of the grating units and the waveguide losses, there will be an exponential decay superimposed on the interferogram. A high out-coupling efficiency leads to a large decay rate, reducing the optical intensity of the interferogram at a large OPD. As we will see from the experiments, the result is a reduced resolution. On the other hand, a small out-coupling means that only a little part of the light is coupled out to the recording system. Since the out-coupled intensity is weak, we will need a very sensitive detection system, otherwise the SNR could be impaired. According to our experience, a good compromise is that after a length L, the total power has decayed to $1/e$ of the input value. The efficiency of the out-coupling is determined by how much the evanescent fields feel the grating and how strong the grating is. For a given distance between the grating and the waveguide as well as a fixed grating strength S, the efficiency is proportional to the width of the grating w_g. It is therefore also important to properly choose the width of the grating for the desired efficiency of the evanescent

scattering.

- **The period of the grating** This parameter Λ_g determines the out-coupling angle (with respect to the normal direction) of the grating. In order to record the interferogram from above, this angle is preferably around 10 degrees. This will keep us away from the drop of grating efficiency due to the second order back reflection [7]. The out-coupling angle is wavelength-dependent, which would eventually play a role in limiting the operation bandwidth of our FTS, especially when considering a record system with a limited numerical aperture (NA).

- **The directionality of the grating** Typically, a standard grating can only diffract half (or less) of the scattered power upwards. This means at least half of the power that is coupled out by the grating does not go the recording system in the case where we want to record the interferogram from above. In literature, there are various ways to design a high-directionality grating [8–10]. Inspired by them, we can also design a grating with a high directionality in the upwards direction, considering the allowable minimum feature size of 150 nm for the available SiN MWP runs. Figure 2.3 shows a design of the stairs-like grating that diffracts the majority of the power upwards.

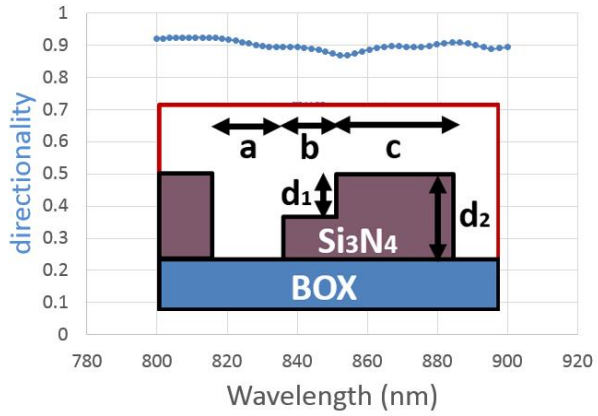

Figure 2.3: The side cross section of a period of the high directionality grating. The directionality describes the fraction of the out-coupled power that is diffract upwards. The parameters used are: a=180 nm, b=160 nm, c=280 nm, d_1=150 nm and d_2=300 nm. Adapted from [2].

2.2.3 An example for the design

Now, we will give an example of the design with the parameters listed in table 2.1 and present the corresponding simulation results. In this example, we consider a rib waveguide with the rib core height of 300 nm and the rib slab thickness of 150 nm. We are targeting the operational wavelength range in the NIR region centered at 850 nm.

width w_n	350 nm
width w_w	650 nm
width w_g	280 nm
spacing d_{gn}	790 nm
spacing d_{gw}	440 nm
period of the grating Λ_g	580 nm
total length of the grating L	10 mm

Table 2.1: List of parameters for the design of the co-propagative stationary FTS based on evanescent scattering

The first step is to choose waveguide widths, as they will determine the resolution and the required sample step length. With a commercially available mode solver FIMMWAVE [11], we can solve the modes and calculate the effective refractive indices for the waveguide modes considered. Through parameter sweep, we can have an idea of how the effective refractive indices change with the waveguide width. The choice of widths w_n and w_w should lead to a large Δn_{eff} for achieving high resolution. But we also need to keep in mind that high order modes should be avoided in the waveguides. For instance, we can choose w_n of 350 nm and w_w of 650 nm. It's worth mentioning that these two values are not strict numbers, as deviations will only affect the resolution slightly but not harm the operation of the on-chip FTS. Figure 2.4 shows the dispersion curve, the effective indices as a function of wavelength, for the waveguide modes. At the center wavelength of 850 nm, the narrow and wide waveguides have effective refractive indices of 1.6221 and 1.6639, leading to a Δn_{eff} of 0.0418. Considering the total length of the grating L of 10 mm, the resolution is calculated to be 1.72 nm while the pitch of the interferogram is 20.33 μm.

With the effective indices, we can find the desired grating period with the following equation,

$$\Lambda_g = \frac{\lambda}{n_{eff} - \sin\theta} \tag{2.5}$$

where n_{eff} is the effective refractive index of the mode considered, and θ is

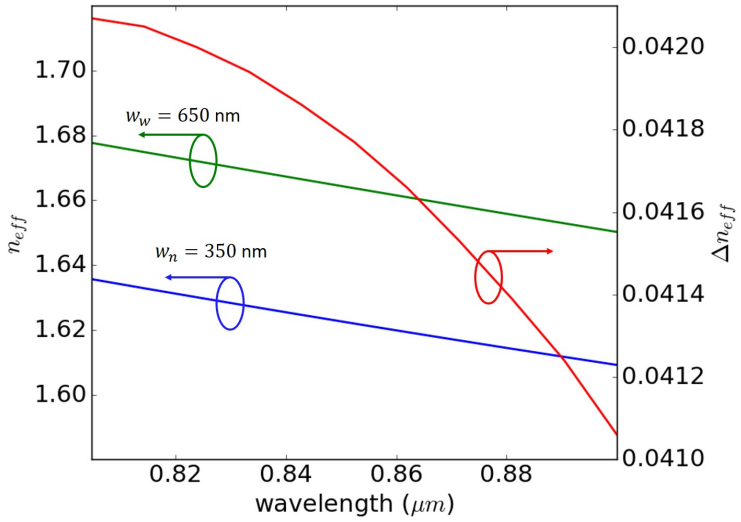

Figure 2.4: The wavelength dependent effective indices and their difference calculated for the narrow (w_n = 350 nm) and the wide (w_w = 650 nm) rib waveguides.

the diffraction angle with respect to the normal of the grating. For example, a grating period Λ_g of 580 nm will result in θ of 9.0 and 11.4 degrees for the considered waveguide modes at a wavelength of 850 nm. In practice, it is often useful to avoid perpendicular diffraction, i.e., θ = 0, since in that case, the grating has low diffraction efficiency due to back reflection.

The grating strength can then be calculated with another commercially available finite-difference-time-domain (FDTD) software, Lumerical [12]. In the 2D simulation as sketched in figure 2.5, we monitor the power P_{in} before the gratings and the remaining power P_{re} after the gratings. The grating strength can be calculated as,

$$S = -\frac{1}{l} \ln \frac{P_{re}}{P_{in}} \tag{2.6}$$

where l is the total length of the grating units considered in the simulation. For the grating with a period of 580 nm and a duty cycle of 50%, S is calculated to be around 0.062 μm^{-1}.

The next step is to determine the desired confinement factor Γ, which describes how much a guided mode feels the grating units with specific dimensions. Together with the grating strength S, the confinement factor Γ has an impact on the power decay rates of the waveguide modes as they

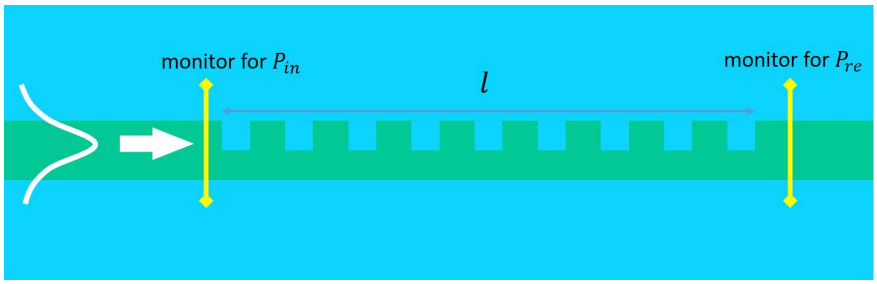

Figure 2.5: A sketch of the simulation that allows the calculation of the grating strength.

propagate alongside the grating. As introduced above, with waveguide losses α taken into consideration, a proper value of Γ should allow a power decay of $1/e$ over the length of L.

$$L \cdot (\Gamma \cdot S + \alpha) = 1 \tag{2.7}$$

Again, FIMMWAVE is used to calculate the intensity distribution of the modes. The confinement factor for a waveguide mode can then be calculated as the normalized integration of the electric fields in the grating area. In FIMMWAVE, this can be calculated with the mode property of "fill factor", after specifying the grating area with the "cfseg" flag (section 5.1.8 in [13]). For a given grating width, we can always calculate the corresponding spacing between the waveguide and the grating for a desired confinement factor. It is also vital to ensure that the two confinement factors of the two waveguide modes equal to each other approximately for the best contrast of the interference pattern. For example, with w_g of 280 nm, we can sweep the spacing between the waveguide and the grating in the simulation, targeting at the desired confinement factor determined by equation 2.7. The parameter sweeps lead to the optimum spacing d_{gn}=790 nm and d_{gw}=440 nm. In figure 2.6, we show the two fundamental TE modes in the cross-section at a wavelength of 850 nm.

As we want to have broadband operation, we are also interested in seeing how these confinement factors change with varying wavelength. In figure 2.7, we plot the confinement factors as a function of the wavelength. We can see that the confinement factors roughly equal each other in the wavelength range considered. However, due to the dispersive nature of the waveguide modes, the confinement factors show a large wavelength dependency. As we will see in the next chapter when we discuss the experimental results, this could influence the performance of the on-chip FTS and eventually

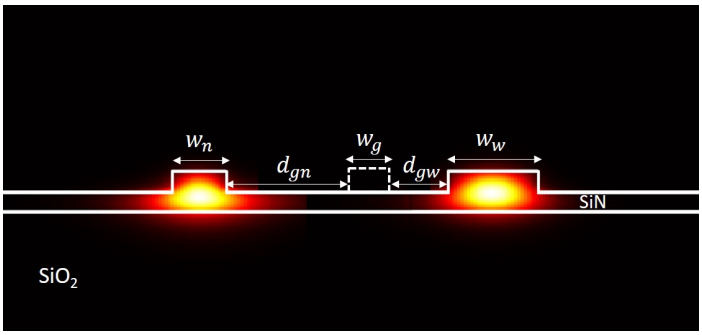

Figure 2.6: The cross-section of the design with the parameters listed in 2.1 and the intensity distribution of the fundamental TE modes confined in the two waveguides considered.

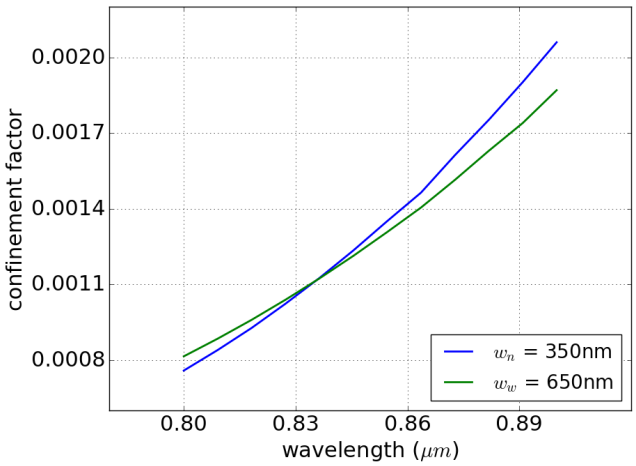

Figure 2.7: The calculated confinement factors in the grating region for the fundamental TE modes confined in the narrow (w_n = 350 nm) and the wide (w_w = 650 nm) rib waveguide.

leads to a limitation on the operation bandwidth.

2.2.4 Inverted taper for edge coupling

Fiber-to-chip coupling is typically inefficient due to the large mode mismatch between the big fiber mode (a few microns) and the small waveguide mode (sub micron). Grating couplers have been widely used to solve this

problem. A well designed standard SOI grating coupler typically has a peak coupling efficiency of 31% and a 1 dB bandwidth of 40 nm [14]. While the coupling efficiency can be further improved by introducing an additional bottom mirror layer [15] or by utilizing a nonuniform grating [16], the improvement of bandwidth is much more complicated and requires sophisticated design [17] and/or sub-wavelength features [18].

Another often used coupling approach is horizontal coupling where an edge coupler can be used to couple the fiber mode to the waveguide mode in a much broader wavelength range. This coupling approach is suitable for the proposed on-chip co-propagative stationary Fourier transform spectrometer as it is expected to be operational in a broad wavelength bandwidth.

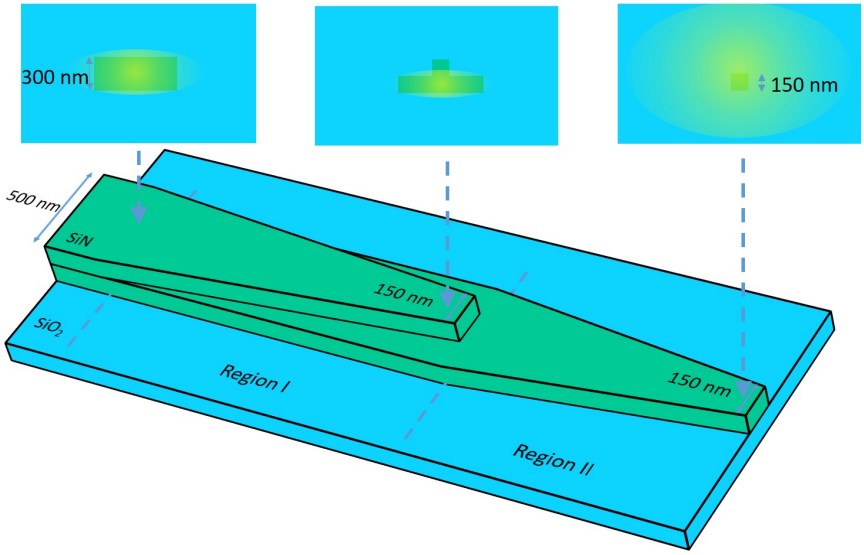

Figure 2.8: A schematic illustration of an inverted taper for the wire waveguide with a height of 300 nm and a width of 500 nm. The cross-sections show the procedure of pushing a guided mode into the cladding. The top cladding is not depicted in the 3D drawing.

A widely used solution for edge coupling utilizes the inverted taper [19, 20], which can be either lateral, vertical, combined (3D) or based on a sub-wavelength grating waveguide [21]. A typical inverted taper functions as a spot size converter (SSC), tapering the waveguide from the standard waveguide dimensions to a smaller tip and pushing the guided modes into the cladding. This efficiently solves the problem rising from the large mode mismatch between the optical fiber and waveguides and inherently provides large transmission bandwidth as well as high coupling efficiency. In a sim-

ple form, figure 2.8 shows the sketch of an inverted taper edge coupler connected to an optical wire waveguide with the cross-section dimension 500×300 nm. In transition region I, the wire waveguide transits to a shallow etch rib waveguide (etch depth of 150 nm), with the rib core tapering down to a tiny tip end with a width of 150 nm, limited by the minimum feature size allowed by the available lithography. This would push the optical modes into the 150 nm thick rib slab. In transition region II, the rib slab is again tapered down to a tip end to further push the mode into the oxide cladding. In such a way, the optical mode guided in a waveguide is converted to the cladding mode that has relatively large mode dimension, matching the Mode Field Diameter (MFD) of a lensed fiber, for example.

2.2.5 Polarization control

Typically, an inverted taper edge coupler has a relatively low extinction ratio between the TE and TM modes. As we only want to use the fundamental TE modes of the waveguides for the operation of the proposed on-chip co-propagative stationary FTS, there is a need for polarization control. A straightforward way to implement polarization control is, of course, to do it off-chip with polarization management either based on a fiber squeezer or free-space optics. Nevertheless, having on-chip polarization control would be beneficial to the simplification of the characterization and also to the further integration [22–24].

There are various ways to implement on-chip polarization control by introducing different asymmetries in the waveguides [25–27]. Among different types of waveguide-based on-chip polarization rotators, [28] offers a convenient approach for polarization splitting and converting, which is easy to implement on the SiN platform as used here. In this approach, the coupling between the TE and TM mode is enabled by breaking the symmetry of the waveguide in the vertical direction. This can be implemented with SOI wire waveguides that have a different cladding material on the top and below as introduced in [28].

Similarly, this principle can be applied to SiN rib waveguides that have the same cladding material around it. Solved with FIMMWAVE, the effective indices of the guided modes for a silicon nitride rib waveguide are shown in figure 2.9 as a function of the core width ranging from 0.55 to 1.55 μm. Due to the vertical asymmetry induced by the rib geometry, there is a point where the polarization of some eigen-modes are indistinguishable because of mode hybridization. Around this point, the fundamental TM mode can be converted to the first order TE mode as the rib core width varies.

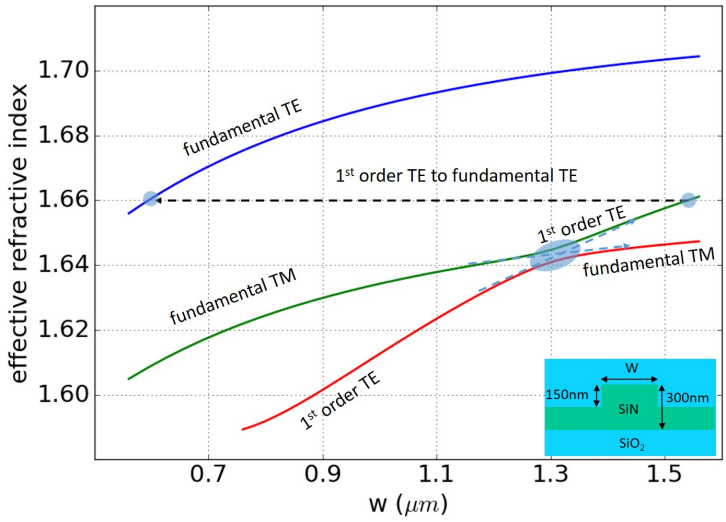

Figure 2.9: The calculated effective indices for the eigen-modes of Silicon nitride rib waveguide. The inset shows the cross-section of the rib waveguide that is considered in the simulation.

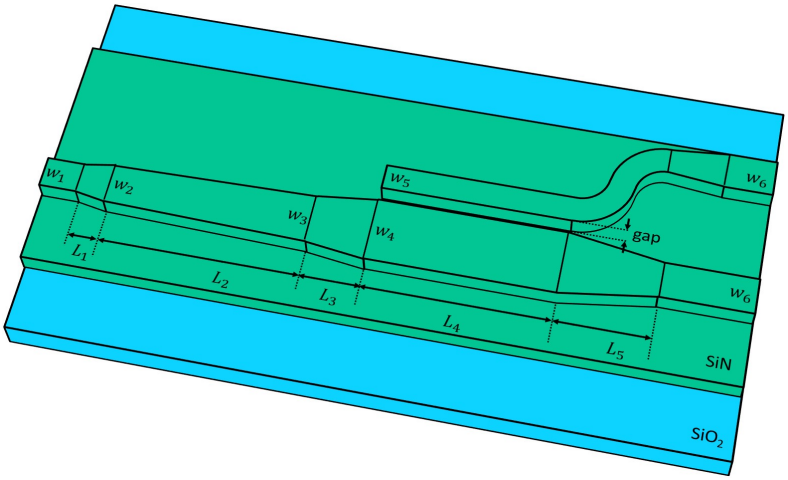

Figure 2.10: The 3D schematic drawing of a polarization rotator that is based on the silicon nitride rib waveguide. The top cladding is not depicted.

Figure 2.10 shows a top view sketch of a silicon nitride rib waveguide based polarization rotator. When the waveguide is tapered from w_1 to w_4, the fundamental TM mode is coupled into the first order TE mode. After that, in an asymmetrical directional coupler region of length L_4, this first-order TE mode is coupled to the fundamental TE mode of a narrow bus waveguide with the width of w_5. The bus waveguide then bends away from the main waveguide. In the meanwhile, the main waveguide is tapered down to a width of w_6 so that the high order TE modes are not guided. Throughout the tapers and couplers, the launched fundamental TE mode keeps its polarization state and stays in the main waveguide.

width w_1, w_6	0.5 μm
width w_2	1.28 μm
width w_3	1.32 μm
width w_4	1.5 μm
width w_5	0.6 μm
length L_1	60 μm
length L_2	86 μm
length L_3	14 μm
length L_4	20.26 μm
length L_5	10 μm
gap	0.23 μm

Table 2.2: List of parameters for the design of the polarization rotator.

Table 2.2 shows the parameters for a design. In the design, a small value of w_1 and w_6 should be considered for single-mode operation, allowing only the fundamental TE and TM modes. w_4 should be large enough to stay far away from the mode hybridization width range while still permit coupling of the first order TE mode in the main waveguide to the fundamental TE mode in the bus waveguide. w_2 and w_3 should be on the two sides of the point where mode hybridization happens. A large L_2 is preferable to maximize the mode-conversion efficiency. L_1 and L_3 should be small while still providing high tapering efficiency. Lastly and importantly, the gap and L_4 are together optimized for efficient coupling between the first order TE mode in the main waveguide and the fundamental TE mode in the bus waveguide.

To determine the parameters, we first pick the widths from figure 2.9. With these widths, we can use FIMMPROP [29] to optimize the taper lengths. L_1 is set to 60 μm, which according to our experience, should be enough for achieving maximum tapering efficiency. As discussed in reference [28], L_3

can be calculated as $L_1(w_4 - w_3)/(w_2 - w_1)$. Through parameter sweep, we find that L_2 should be longer than 85 μm to reach the maximum mode-conversion efficiency. The gap is chosen to be 0.23 μm as a compromise between a small length of the direction coupler (L_4) and a better fabrication tolerance. With the gap determined, the optimal value of L_4 can be obtained through sweeping the length. With the design parameters as listed in table 2.2, we simulated the intensity distribution in the polarization rotator under different input polarization with FIMMPROP. The results are shown in figure 2.11.

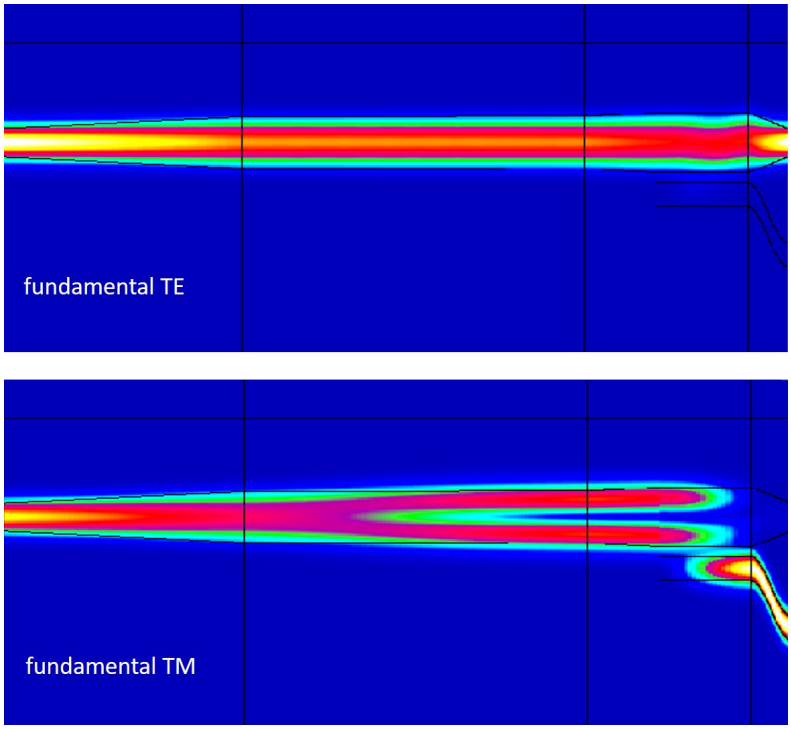

Figure 2.11: The simulated intensity distribution of the light propagating in the designed polarization rotator when the launched mode are the fundamental TE (upper) and TM mode (lower).

2.2.6 Power splitter

After the polarization rotator, the light should be split into two copies to generate the interferogram. This can be done with an on-chip optical power splitter. As one of the most widely-used components, the optical power

splitter has been studied and implemented in various forms. The three major categories of 3-dB power splitter are the Y-junction structures [30, 31], the directional couplers [32] and the multimode interference (MMI) waveguides [33, 34].

While the Y-junction splitters are usually compact in size and insensitive to the polarization, they have very low fabrication tolerance. In practice, the limited resolution of the lithography and etching process would often result in substantial scattering loss. To improve the loss performance of a Y-junction splitter, one would need to carefully design the shape of the junction as reported in [31]. The directional couplers, on the other hand, offer very low loss as the light will not encounter abrupt changes of geometry during propagation. However, for a required splitting ratio, a directional coupler often has a rather small operational bandwidth. Besides, the splitting ratio of the directional coupler is considerably affected by the fabrication uncertainties.

Based on the self-imaging effect, the MMI splitters can provide a low loss, high fabrication tolerance as well as stable splitting ratio as in the case of a 1×2 MMI. These all make an MMI splitter attractive for beam splitting in various photonics applications and motivate researchers to optimize the performance continuously. As an example, it has been reported that a well designed MMI splitter can perform optical power splitting with only 0.1 dB excess loss [34].

In the design of our on-chip FTS, we use a 1×2 MMI as the power splitter. To achieve the low loss splitting, the 1×2 MMI is implemented with rib waveguides, where the SiN rib core height is 300 nm, and the rib slab is etched down to the thickness of 150 nm, as shown in figure 2.12 (a).

In the first step of the design, a proper value of the width of the multi-mode section, w_{mmi} is selected. The length of the multi-mode section can then be estimated to be $3L_\pi/8$, where the beating length L_π can be expressed as $4nw_{eff}^2/3\lambda$ [35]. From this starting point, we perform simulations to further decide the exact MMI length l_{mmi} by parameters sweeping in the software FIMMPROP. Next, the offset at which the two output waveguides should be placed is determined. Furthermore, we design a linear taper with length l_{taper} to shrink the access waveguide from a large width w_1 to the width of the input and output waveguide w_0. This could help minimize the excess loss. With the parameters listed in table 2.3, the simulated light intensity distribution (at a wavelength of 850 nm) is shown in figure 2.12 (b). From the simulation, the transmission measured at each output port is around 48.9%.

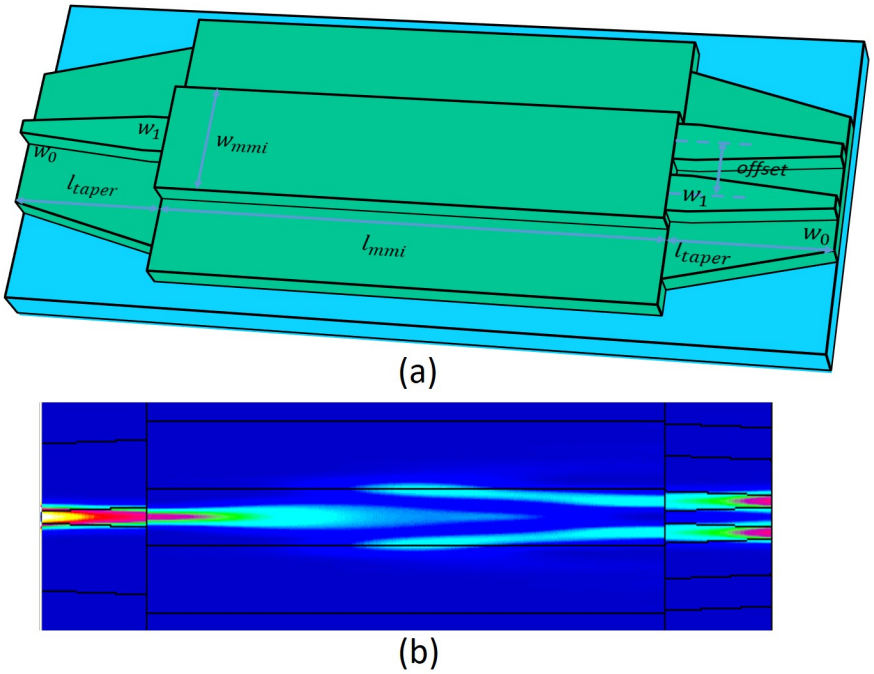

Figure 2.12: (a) The 3D drawing of the shallow-etched 1×2 MMI where the top cladding is not depicted. (b) The simulated intensity distribution of the light split by the 1×2 MMI splitter. The parameters used in the simulation are listed in table 2.3.

width w_0	0.5 μm
width w_1	1.2 μm
width w_{mmi}	3.44 μm
length l_{mmi}	14.5 μm
length l_{taper}	5 μm
offset	1.89 μm

Table 2.3: List of parameters for the design of the shallow etched 1×2 MMI.

2.3 Lateral-leakage-based co-propagative stationary FTS

In this section, we will introduce a different approach to implement the co-propagative stationary FTS. Similar to what is introduced in the previous section, in this new approach, we still have two parallel waveguides with different widths. Instead of exploiting the interferogram generated by the interference of the evanescent fields of the two guided modes in the region between the two waveguides, we take advantage of lateral leakage and let the two modes interfere in the slab far away from the two waveguides.

Lateral leakage is the phenomenon that a waveguide mode laterally couples to the slab mode in the flank of the waveguide core. It is first reported in an SOI rib waveguide platform where the TM-like modes suffer from waveguide-width-dependent lateral leakage loss in the rib waveguides [36, 37]. To understand the cause of the lateral leakage, we can look at the phase-matching diagram shown in figure 2.13.

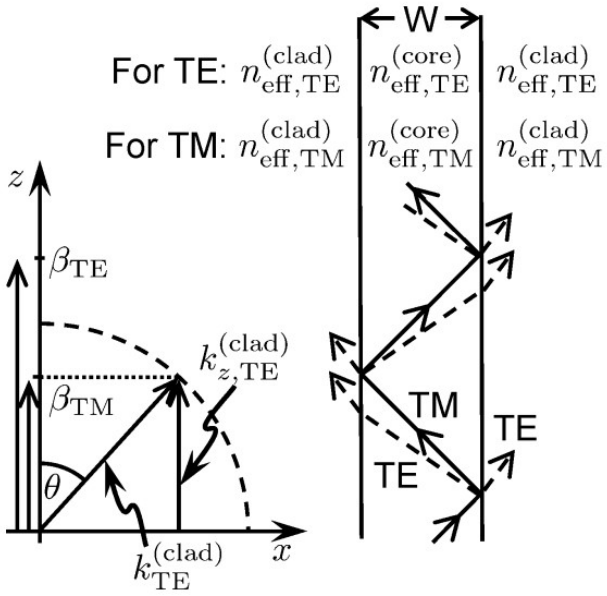

Figure 2.13: A diagram shows that the TM-like guided mode in a rib waveguide can be phase-matched to a radiating TE slab mode propagating in the rib slab. Reprinted from Ref. [37].

For a typical SOI rib waveguide, the propagation constants of the TM-like modes confined in the core region are not only much smaller than those of the guided TE-like modes but also smaller than that of the propagating TE slab mode in the cladding. As the slab modes can propagate at any direction in the slab, a TM waveguide mode can be phase-matched in the z direction to a TE slab propagating mode. Therefore, the TM-guided mode can be coupled into the TE-slab mode that propagates in the slab at a particular angle θ with respect the z direction, as illustrated in figure 2.13.

2.3.1 Lateral leakage in a SiN rib waveguide platform

In a silicon nitride waveguide platform, the index contrast is smaller than in an SOI waveguide platform. Considering SiN rib waveguide with rib core height of 300 nm and shallow etch depth of 150 nm, the propagation constant of the fundamental TM mode in the rib waveguide is still larger than that of the TE slab modes propagating in the thin rib slab. As a result, the lateral leakage of the guided TM mode will not happen. Nevertheless, we can force the guided modes to leak laterally by positioning a thick slab (of the same height as the rib core) on the flank of the rib waveguide. In this situation, according to simulations, the TE-slab modes in this thick slab now have larger propagation constants than the guided fundamental TE mode, allowing for the lateral leakage of the latter.

As an illustration, figure 2.14 shows the lateral leakage in the halfway etched silicon nitride rib waveguide that has a rib core height of 300 nm and rib slab thickness of 150 nm. The guided TE mode can be coupled to the slab TE mode that propagates in the thick slab (300 nm) when the following phase-matching condition is fulfilled,

$$\beta_{TE}^{(core)} = k_{z,TE}^{(slab)} = k_{TE}^{(slab)} \sin\theta. \tag{2.8}$$

Such a phase-matching condition is easy to satisfy. Since the propagation constants of the guided modes are always smaller than that of the propagating TE mode in the thick slab, there must be a θ that allows for phase-matching. Besides, given that the lateral leakage is enabled by the evanescent coupling between the guided modes and the slab modes, we can tailor the leaking rate by changing the spacing between the rib core and the thick slab.

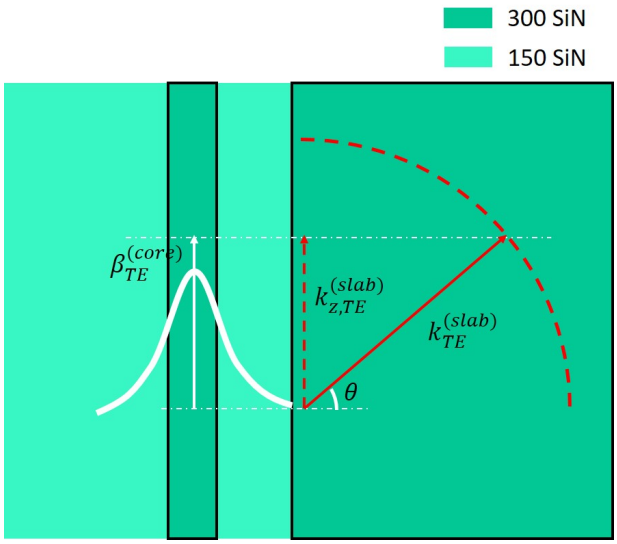

Figure 2.14: A sketch illustrates the lateral leakage of a TE-like guided mode in a SiN rib waveguide into the radiating TE slab mode propagating in a thick slab that has the same thickness as the rib core. Along the propagating direction, the guided mode is phase-matched to the slab mode.

2.3.2 Interferogram generated in the slab

Now we can explain how to implement the co-propagative Stationary FTS, with use of the lateral leakage. As shown in figure 2.15, if we put two parallel rib waveguides next to the thick slab at a proper distance, due to lateral leakage, both modes can be coupled to the slab modes that propagate at two different directions (indicated by θ_1 and θ_2, respectively). These two modes, propagating in the slab, can interfere with each other and create an interference pattern in the slab at any distance from the two waveguides. The advantage is that we can measure the interferogram away from the two waveguides. As will be introduced later, this allows for more approaches to record the interferogram. The direction of the interference pattern (defined at the direction of the periodicity) is at an angle to the waveguides, which is calculated to be $\frac{\theta_1+\theta_2}{2}$, as one can see in figure 2.15.

To simplify the discussion, we again assume a monochromatic signal with a wavelength of λ that excites the fundamental TE modes in the two waveguides. The interferogram generated in the slab will have a period given by

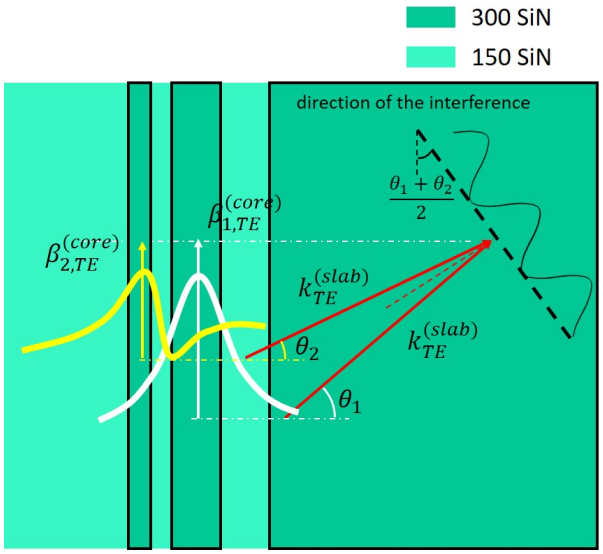

Figure 2.15: A sketch showing how the interferogram can be generated by the lateral leakage as two waveguides with different widths are placed on the flank of the thick slab.

$$\Lambda_0 = \frac{\lambda}{2n_{eff}^{(slab)} \sin\left(\frac{\theta_1-\theta_2}{2}\right)} \tag{2.9}$$

where $n_{eff}^{(slab)}$ is the effective refractive index of the slab TE modes, which has different propagation directions but share the same phase velocity. As the interferogram is generated along the direction at an angle to the direction of the waveguides, it is more interesting to look at the period projected to the direction of the waveguides. The projected period can be calculated as,

$$\Lambda = \frac{\Lambda_0}{\cos\left(\frac{\theta_1+\theta_2}{2}\right)} = \frac{\lambda}{n_{eff}^{(slab)}(\sin\theta_1 - \sin\theta_2)} \tag{2.10}$$

According to the phase-matching condition given by equation 2.8, the effective refractive indices of the slab TE modes can be related to the effective refractive indices (n_1 and n_2) of the two guided modes as

$$n_{eff}^{(slab)} = \frac{n_1}{\sin\theta_1} = \frac{n_2}{\sin\theta_2}. \tag{2.11}$$

Inserting these expressions into equation 2.10, we can calculate the length of the projected period as,

$$\Lambda = \frac{\lambda}{n_1 - n_2} \tag{2.12}$$

With n_1-n_2 written as Δn_{eff}, we can see that this is the same expression as equation 2.3. Therefore, we can also use expression 2.4 to estimate the theoretical resolution for this new type of co-propagative stationary FTS.

2.3.3 A design example

In designing a lateral-leakage-based stationary FTS, similarly, we first need to determine the widths of the two waveguides with a proper Δn_{eff}, which determines the resolution (for a given waveguide length) and the required sample step-length. With the waveguide widths determined, the next step is to decide the spacing between the two waveguides and to find out how close the thick slab should be placed next to the two waveguides. These spacings will give the leaking rate of the two waveguide modes. Again, as detailed in section 2.2.2, the criteria are that the two waveguides should have equal leaking rate and that the decay of the optical power in the waveguides over a length of L should be around $1/e$. For the former, we should place the thick slab at the side of the wide waveguide, as the guided mode is more confined in it.

The leaking rate can be calculated in FIMMWAVE simulation by calculating the mode loss. In principle, assuming no material loss, a TE mode guided in the rib waveguide has zero propagation loss in the simulation (with a complex mode solver) as the mode is confined in the rib core region. However, when a thick slab is placed next to the rib core, the optical power of a guided TE mode can be coupled into the radiating slab mode, leading to a "side loss" as mentioned in section 2.6.3.3 in [13]. In FIMMWAVE, with the complex mode solvers, by using Perfect Matching Layers (PML) as the boundary on the side of the thick slab, the side loss can be calculated. As an example, with the same considerations explained in section 2.2.3, we take w_n of 350 nm and w_w of 650 nm. In FIMMWAVE simulations, we sweep the spacing between the waveguide and the thick slab, targeting at the desired leakage loss. The parameter sweeps lead to the spacings as listed in table 2.4. With these parameters, we show the simulated intensity distribution of the waveguide modes in the cross-section. Figure 2.16 shows the intensity distribution of the two fundamental TE-like modes.

width w_n	350 nm
width w_w	650 nm
spacing d_{wn}	790 nm
spacing d_{ws}	440 nm
total length of the grating L	10 mm

Table 2.4: List of parameters for the design of the co-propagative stationary FTS based on lateral leakage

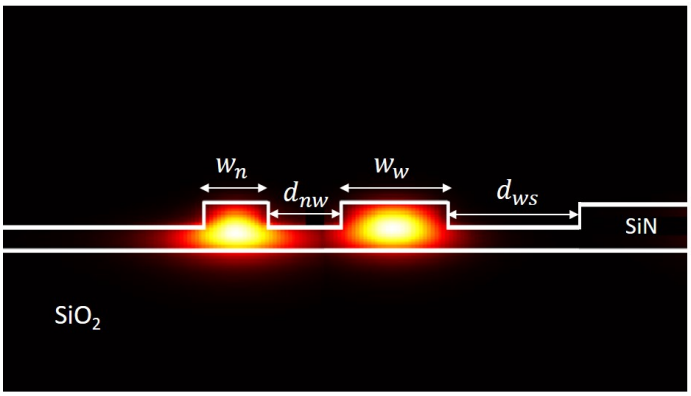

Figure 2.16: the cross-section of the design with the parameters listed in 2.4 and the intensity distribution of the fundamental TE modes confined in the two waveguides considered.

In figure 2.17, we plot the calculated mode loss as a function of the wavelength. The loss α is defined by

$$P_L = P_0 \cdot e^{-\alpha L} \tag{2.13}$$

where P_0 and P_L are the power of a waveguide mode before and after the propagation over a distance of L, respectively.

As one can see from figure 2.17, while the two leaking rates are equal to each other, they both show a large wavelength dependency, resulting from the dispersive nature of the waveguide modes. A large mode loss for long wavelengths will result in a rapid exponential decay superpositioned on the interferogram at large OPD, limiting the length of the interferogram that can be measured. For short wavelengths, a low leaking rate means that the average intensity of the interferogram is small and the SNR is therefore bad. From both sides, the dispersive nature of the waveguide modes limits the operational band. In the next chapter, we will further discuss this limitation with the measurement results presented.

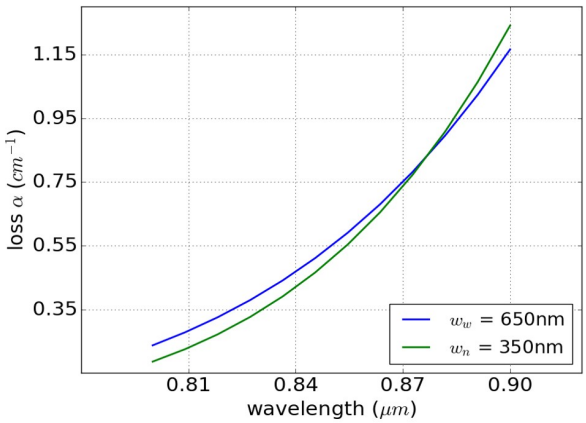

Figure 2.17: The calculated mode loss for the fundamental TE modes confined in the narrow (w_n = 350 nm) and the wide (w_w = 650 nm) rib waveguide.

2.3.4 Approaches to record the interferogram

Compared to the evanescent scattering based configuration, the lateral leakage based FTS introduced in this section has the advantage in that the generation and the detection of the interferogram can be "decoupled". As the interferogram is generated in the slab and can propagate away from the two waveguides, there are more options for recording the interferogram. In the next paragraphs, we introduce some approaches that can potentially be applied to record the interferogram.

In the first approach, as shown in figure 2.18, we can position an oblique grating to diffract the interferogram upwards to a photodiode array. As the interferogram is created by the TE slab modes that can propagate in the slab, the grating can be positioned far away from the two waveguides, avoiding any potential influence to the waveguide modes. It is worth mentioning that the grating should be strong enough to couple all the light out. Otherwise, the light surviving through the gratings can be reflected by the edge of the thick slab, propagating back to the grating region and making the recorded interferogram complicated.

The second approach is shown in figure 2.19. As the two modes that generate the interferogram can propagate in the slab, the interferogram can also be treated as a pattern that can propagate in the slab. In this case, we can use a series of inverted tapers to sample the interferogram and send the light to integrated photodiodes.

Another two potential approaches, while still using an external photodiode array, do not rely on the gratings, or any scatterers. After propagating in the slab mode for a short distance, the interferogram can be directed to a detector array by the reflection from a slanted mirror, possibly with a metal coating (as shown in figure 2.20) or the refraction from an angled facet (as shown in figure 2.21).

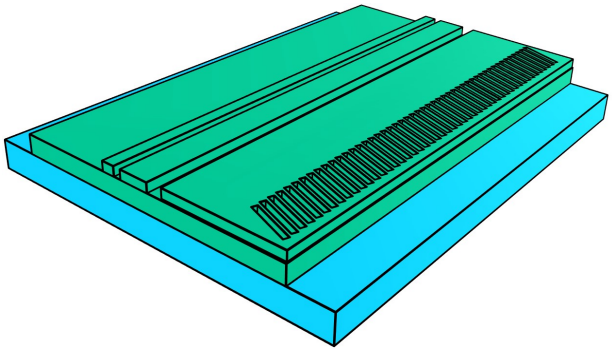

Figure 2.18: A sketch for the grating based approach to record the interferogram. The grating can be positioned far away from the two waveguides to diffract the interferogram to a photodiode array (not shown in the sketch).

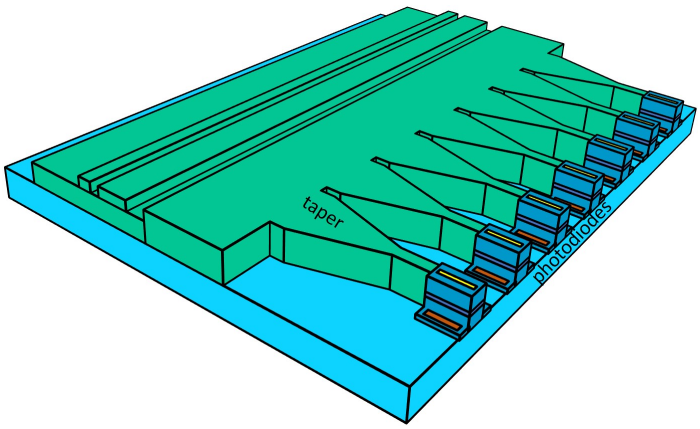

Figure 2.19: A sketch for the integrated photodiodes based approach to record the interferogram. A series of inverted tapers are used to sample the interferogram as it can propagate in the thick slab away from the two waveguides.

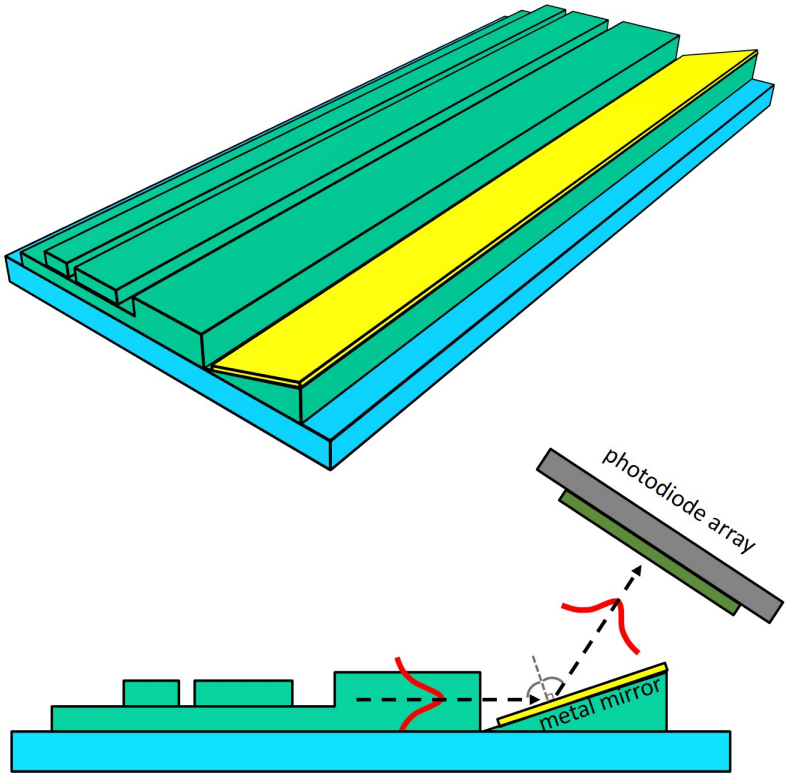

Figure 2.20: A sketch for the metal mirror based approach to record the interferogram. The interferogram propagating through the slab can be reflected by the metal mirror and coupled to the detector array.

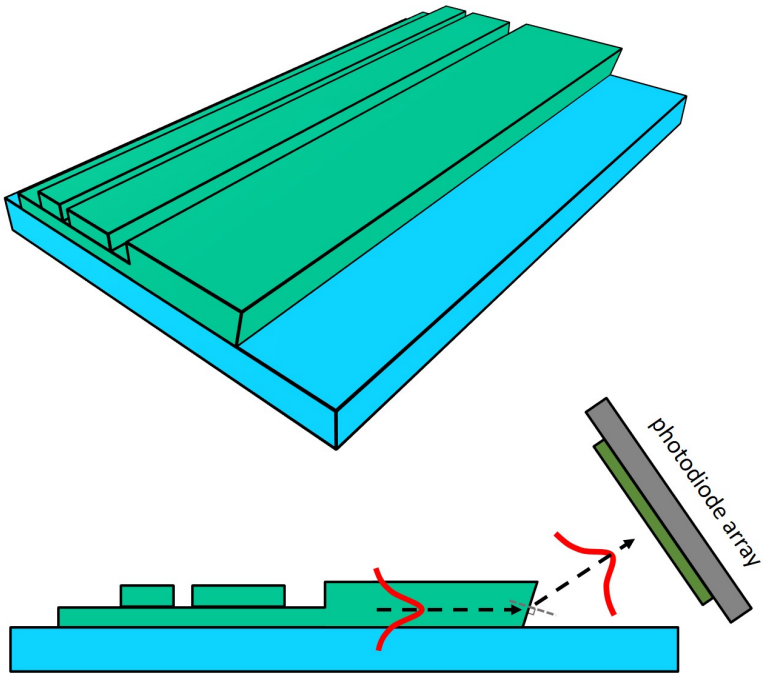

Figure 2.21: A sketch for the angled facet based approach to record the interferogram. The interferogram propagating through the slab can be deflected to the detector array by an angled facet.

2.4 Conclusion

We proposed a novel type of on-chip integrated stationary FTS that relies on the interference between two co-propagative waveguide modes with different phase velocities. As introduced, the co-propagative stationary FTS we proposed can provide a moderately high resolution over a broad wavelength range in a very small area without any moving components. These characteristics make it a promising candidate for a compact and robust on-chip FTS spectrometer and make it suitable for further integration into various lab-on-a-chip systems such as on-chip Raman or absorption spectroscopy systems. In this chapter, the working principles and the design details of the two different implementations have been explained and discussed. We also presented design examples for the implementations on a SiN rib waveguide platform. In the next chapter, we will present our work regarding the experimental explorations of both the evanescent-scattering-based and lateral-leakage-based on-chip FTS.

References

[1] Xiaomin Nie, Eva Ryckeboer, Günther Roelkens, and Roel Baets. *Novel concept for a broadband co-propagative stationary Fourier transform spectrometer integrated on a Si3N4 waveguide platform*. In CLEO: Applications and Technology, pages JW2A–120. Optical Society of America, 2016.

[2] Eva Ryckeboer, Xiaomin Nie, Ananth Z Subramanian, Daan Martens, Peter Bienstman, Stephane Clemmen, Simone Severi, Roelof Jansen, Günther Roelkens, and Roel Baets. *CMOS-compatible silicon nitride spectrometers for lab-on-a-chip spectral sensing*. In Silicon Photonics and Photonic Integrated Circuits V, volume 9891, page 98911K. International Society for Optics and Photonics, 2016.

[3] Xiaomin Nie, Eva Ryckeboer, Günther Roelkens, and Roel Baets. *CMOS-compatible broadband co-propagative stationary Fourier transform spectrometer integrated on a silicon nitride photonics platform*. Optics express, 25(8):A409–A418, 2017.

[4] Etienne Le Coarer, Sylvain Blaize, Pierre Benech, Ilan Stefanon, Alain Morand, Gilles Lérondel, Grégory Leblond, Pierre Kern, Jean Marc Fedeli, and Pascal Royer. *Wavelength-scale stationary-wave integrated Fourier-transform spectrometry*. Nature Photonics, 1(8):473, 2007.

[5] Peter R Griffiths and James A De Haseth. *Fourier transform infrared spectrometry*, volume 171. John Wiley & Sons, 2007.

[6] Sumner P Davis, Mark C Abrams, and James W Brault. *Fourier transform spectrometry*. Elsevier, 2001.

[7] Dirk Taillaert. *Grating couplers as interface between optical fibres and nanophotonic waveguides.* 2005.

[8] Xia Chen, David J Thomson, Lee Crudginton, Ali Z Khokhar, and Graham T Reed. *Dual-etch apodised grating couplers for efficient fibre-chip coupling near 1310 nm wavelength*. Optics express, 25(15):17864–17871, 2017.

[9] Daniel Benedikovic, Carlos Alonso-Ramos, Pavel Cheben, Jens H Schmid, Shurui Wang, Dan-Xia Xu, Jean Lapointe, Siegfried Janz, Robert Halir, Alejandro Ortega-Moñux, et al. *High-directionality*

fiber-chip grating coupler with interleaved trenches and subwavelength index-matching structure. Optics letters, 40(18):4190–4193, 2015.

[10] Ming Dai, Leilei Ma, Yelong Xu, Minghui Lu, Xiaoping Liu, and Yanfeng Chen. *Highly efficient and perfectly vertical chip-to-fiber dual-layer grating coupler*. Optics express, 23(2):1691–1698, 2015.

[11] Photon Design. *Fimmwave, mode solvers for optical waveguides*. `https://www.photond.com/products/fimmwave.htm`. Accessed: 2019-09-09.

[12] Lumerical Inc. *Lumerical FDTD: Nanophotonic FDTD Simulation Software*. `https://www.lumerical.com/products/fdtd/`, Accessed: 2019-09-09.

[13] Photon Design. *FIMMWAVE Version 6.6*. manual, Jul. 2018.

[14] Dirk Taillaert, Frederik Van Laere, Melanie Ayre, Wim Bogaerts, Dries Van Thourhout, Peter Bienstman, and Roel Baets. *Grating couplers for coupling between optical fibers and nanophotonic waveguides*. Japanese Journal of Applied Physics, 45(8R):6071, 2006.

[15] Frederik Van Laere, Günther Roelkens, Melanie Ayre, Jonathan Schrauwen, Dirk Taillaert, Dries Van Thourhout, Thomas F Krauss, and Roel Baets. *Compact and highly efficient grating couplers between optical fiber and nanophotonic waveguides*. Journal of lightwave technology, 25(1):151–156, 2007.

[16] Yongbo Tang, Zhechao Wang, Lech Wosinski, Urban Westergren, and Sailing He. *Highly efficient nonuniform grating coupler for silicon-on-insulator nanophotonic circuits*. Optics letters, 35(8):1290–1292, 2010.

[17] Neil V Sapra, Dries Vercruysse, Logan Su, Ki Youl Yang, Jinhie Skarda, Alexander Y Piggott, and Jelena Vučković. *Inverse design and demonstration of broadband grating couplers*. IEEE Journal of Selected Topics in Quantum Electronics, 25(3):1–7, 2019.

[18] Yun Wang, Wei Shi, Xu Wang, Zeqin Lu, Michael Caverley, Richard Bojko, Lukas Chrostowski, and Nicolas AF Jaeger. *Design of broadband subwavelength grating couplers with low back reflection*. Optics letters, 40(20):4647–4650, 2015.

[19] Vilson R Almeida, Roberto R Panepucci, and Michal Lipson. *Nanotaper for compact mode conversion*. Optics letters, 28(15):1302–1304, 2003.

[20] Minhao Pu, Liu Liu, Haiyan Ou, Kresten Yvind, and Jørn M Hvam. *Ultra-low-loss inverted taper coupler for silicon-on-insulator ridge waveguide*. Optics Communications, 283(19):3678–3682, 2010.

[21] Pavel Cheben, Jens H Schmid, Shurui Wang, Dan-Xia Xu, Martin Vachon, Siegfried Janz, Jean Lapointe, Yves Painchaud, and Marie-Josée Picard. *Broadband polarization independent nanophotonic coupler for silicon waveguides with ultra-high efficiency*. Optics express, 23(17):22553–22563, 2015.

[22] TK Liang and HK Tsang. *Integrated polarization beam splitter in high index contrast silicon-on-insulator waveguides*. IEEE photonics technology letters, 17(2):393–395, 2005.

[23] Masa-aki Komatsu, Kunimasa Saitoh, and Masanori Koshiba. *Design of miniaturized silicon wire and slot waveguide polarization splitter based on a resonant tunneling*. Optics express, 17(21):19225–19234, 2009.

[24] Hiroshi Fukuda, Koji Yamada, Tai Tsuchizawa, Toshifumi Watanabe, Hiroyuki Shinojima, and Sei-ichi Itabashi. *Ultrasmall polarization splitter based on silicon wire waveguides*. Optics Express, 14(25):12401–12408, 2006.

[25] Ning-Ning Feng, Rong Sun, Jurgen Michel, and Lionel C Kimerling. *Low-loss compact-size slotted waveguide polarization rotator and transformer*. Optics letters, 32(15):2131–2133, 2007.

[26] Yang Yue, Lin Zhang, Muping Song, Raymond G Beausoleil, and Alan E Willner. *Higher-order-mode assisted silicon-on-insulator 90 degree polarization rotator*. Optics express, 17(23):20694–20699, 2009.

[27] BMA Rahman, SSA Obayya, N Somasiri, M Rajarajan, KTV Grattan, and HA El-Mikathi. *Design and characterization of compact single-section passive polarization rotator*. Journal of lightwave technology, 19(4):512, 2001.

[28] Daoxin Dai and John E Bowers. *Novel concept for ultracompact polarization splitter-rotator based on silicon nanowires*. Optics express, 19(11):10940–10949, 2011.

[29] Photon Design. *Fimmprop, optical propagation software - 3D field analysis*. https://www.photond.com/products/fimmprop.htm. Accessed: 2019-09-09.

[30] SH Tao, Q Fang, JF Song, MB Yu, GQ Lo, and DL Kwong. *Cascade wide-angle Y-junction 1× 16 optical power splitter based on silicon wire waveguides on silicon-on-insulator*. Optics express, 16(26):21456–21461, 2008.

[31] Yi Zhang, Shuyu Yang, Andy Eu-Jin Lim, Guo-Qiang Lo, Christophe Galland, Tom Baehr-Jones, and Michael Hochberg. *A compact and low loss Y-junction for submicron silicon waveguide*. Optics express, 21(1):1310–1316, 2013.

[32] Hirohito Yamada, Tao Chu, Satomi Ishida, and Yasuhiko Arakawa. *Optical directional coupler based on Si-wire waveguides*. IEEE photonics technology letters, 17(3):585–587, 2005.

[33] Amir Hosseini, Harish Subbaraman, David Kwong, Yang Zhang, and Ray T Chen. *Optimum access waveguide width for 1× N multimode interference couplers on silicon nanomembrane*. Optics letters, 35(17):2864–2866, 2010.

[34] Zhen Sheng, Zhiqi Wang, Chao Qiu, Le Li, Albert Pang, Aimin Wu, Xi Wang, Shichang Zou, and Fuwan Gan. *A compact and low-loss MMI coupler fabricated with CMOS technology*. IEEE Photonics Journal, 4(6):2272–2277, 2012.

[35] ECM Pennings, RMJN van Roijen, MJN Van Stralen, PJ De Waard, RGMP Koumans, and BH Verbeck. *Reflection properties of multimode interference devices*. IEEE photonics technology letters, 6(6):715–718, 1994.

[36] R Pafchek, R Tummidi, J Li, MA Webster, E Chen, and Thomas L Koch. *Low-loss silicon-on-insulator shallow-ridge TE and TM waveguides formed using thermal oxidation*. Applied optics, 48(5):958–963, 2009.

[37] MA Webster, RM Pafchek, A Mitchell, and Thomas L Koch. *Width dependence of inherent TM-mode lateral leakage loss in silicon-on-insulator ridge waveguides*. IEEE Photonics Technology Letters, 19(6):429–431, 2007.

3

Prototyping and Characterizing the On-chip Stationary FTS

This chapter covers the experimental characterization of the on-chip stationary FTS introduced in Chapter 2. We first introduce the methods we used in the characterization. After that, we will present the measurement results which are followed by the discussions and the conclusions. Some of the materials we will present in this chapter have been published in Ref. [1].

Contents

3.1 Introduction

In Chapter 2, we introduced the basic principle and the design details of the on-chip integrated co-propagative stationary FTS. There are two slightly different ways to implement this new concept of the on-chip stationary FTS. As we explained, in both configurations, we can use gratings, or scatterers, to couple the generated interferogram to the recording system. In this chapter, we will demonstrate the prototypes of the proposed on-chip FTS, explain the different approaches we used to characterize the devices, and discuss the measurement results. In the first part, we will briefly talk about the platforms used for prototyping the design. Next, we will describe the different method for characterizing. After that, we will show the results and discuss the findings.

3.2 Prototyping the on-chip stationary FTS

We first fabricated the evanescent-scattering-based on-chip FTS in PECVD silicon nitride Multi-Project Wafer (MPW) run (BioSiN4 from IMEC). The fabrication of the layer stack starts from a bare silicon wafer. In the first step, a layer of silicon dioxide (SiO_2) is deposited using a high-density plasma (HDP) chemical vapor deposition (CVD) process. This silicon dioxide layer is usually referred to as the Buried Oxide (BOX) layer and has a thickness of 2300 nm in this case. On top of the BOX layer, SiN is deposited with PECVD, which has a thickness of 220 nm for 780 to 900 nm wavelength operation.

On such a SiN wafer, the designed structures are patterned by deep UV lithography (193 nm) with a minimum feature size of 150 nm. There can be two different etch steps, a full etch of 220 nm etch depth to provide the deep trenches that define the wire waveguides, and a shallow etch that has an etch depth of 110 nm, mainly used to define the grating lines and the rib waveguides. As introduced in chapter 2, we should use the shallow etch to define the two asymmetric waveguides and the gratings lying in between. As shown in figure 3.1 (a), one can choose to have oxide top cladding and air top cladding. The former, typically requiring a thin aluminum oxide (AlO) etch stop layer for the precise control of the etching process, offers lower refractive index contrast and therefore can provide lower propagation loss. As a result, we choose to have oxide top cladding for our designs.

In figure 3.2, we show the Scanning Electron Microscope (SEM) images of the designed on-chip FTS at some locations. It is worth noting that

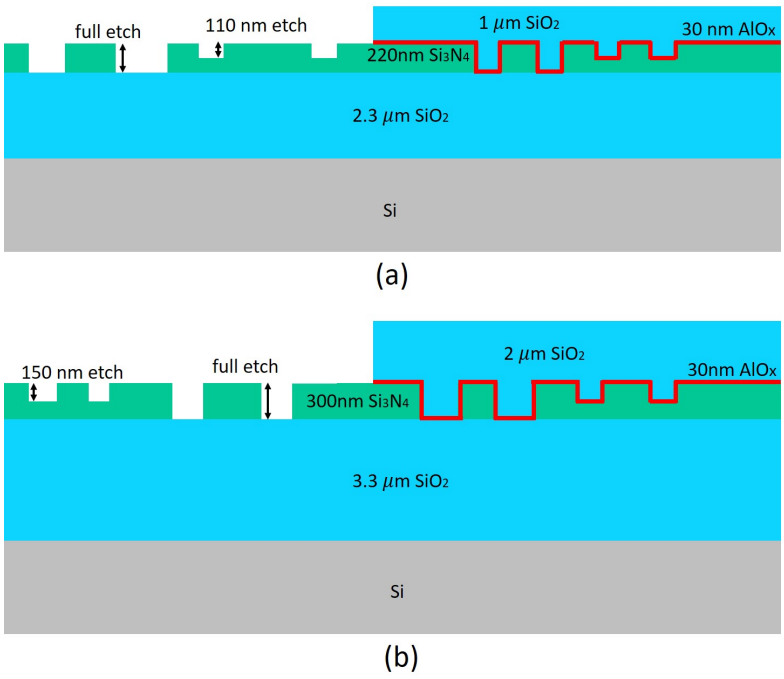

Figure 3.1: Illustrations of the different material stacks used in the SiN platform in (a) BioSin4 run and (b) BioPIX300 run.

these images are taken from a chip that has air top cladding. The oxide top cladding chip often gives poorer images under SEM due to the uniform top surface and the effects of charging.

In figure 3.2 (a), we show the full etched MMI, which is used to split the input signal into two wire waveguides with an equal splitting ratio (50:50). After that, the waveguides are tapered to rib waveguides with different widths in the tapering section, as shown in figure 3.2 (b). A small part of the main structure, including two rib waveguides with different widths and a grating in between, is shown in figure 3.2 (c) with an insert sketching the cross-section. The total length of the grating goes up to 7800 μm with a grating period of 640 nm, allowing the near-vertical out-coupling for a broad wavelength range centered at the wavelength of 850 nm. Although the device has a large length, its width is only ($\sim$10 μm), leading to an overall footprint around of 0.1 mm^2. Such a small footprint potentially offers the possibility to integrate multiple on-chip FTS devices on a single chip, as such can be useful, for instance, in building a hyperspectral imager.

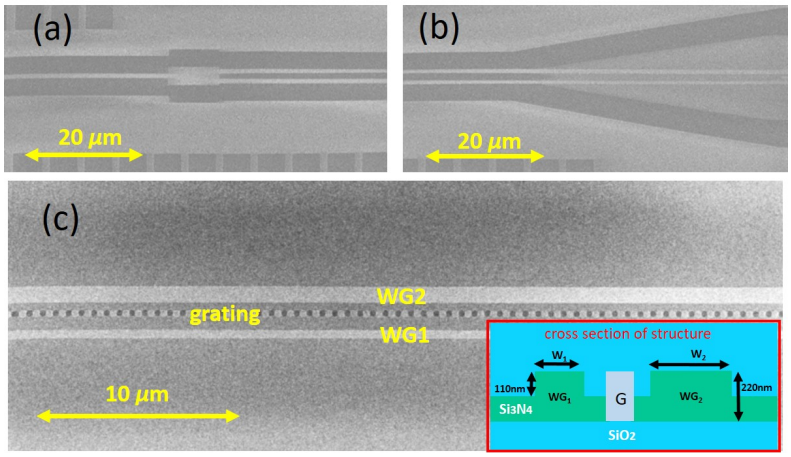

Figure 3.2: SEM pictures of (a) fully etched MMI, (b) taper section tapering wire waveguides to rib waveguides with different widths, (c) the main structure containing two rib waveguides with different widths and the grating units in between. The insert in (c) shows the cross-section, with G indicating the grating. Reprinted from [1].

Later, we shifted to a different silicon nitride platform when the PIX4life project started. The PIX4life project (H2020-ICT-2015 contract 688519) aims to mature a SiN pilot line, that offers high performance, high yield and CMOS-compatible production of SiN PICs together with the accompanying supply chains for various applications in the visible-NIR wavelength range (400-1000 nm) [2]. As shown in figure 3.1 (b), the BioPIX runs we joined uses different layer stacks from that in the BioSiN run.

In BioPIX300 technology, the full thickness of the SiN layer is 300 nm. Both full etch and shallow etch are possible with etch depth of 300 nm and 150 nm respectively. The thickness of the top oxide and the BOX layer are changed to 2 μm and 3.3 μm for optimized grating coupler performance.

The design of on-chip FTS should be adapted to the new stack. For example, in the new designs for these runs, the period of the grating is changed to 580 nm. Moreover, in the BioPIX runs, we also realized the prototype of the lateral leakage based on-chip co-propagative stationary FTS that uses the oblique grating to couple out the interferogram.

3.3 Methods for recording the interferogram

As introduced in Chapter 1, the proposed on-chip FTS could be integrated onto a CMOS image sensor wafer, so as to create a fully integrated solution. While the original PhD plan was to develop a proof-of-concept demonstration for this approach, several delays within the PIX4life project have made experimental demonstration impossible. Therefore we developed characterisation methods without detector array integration. Sine the interferogram generated by our on-chip stationary FTS can be coupled out from the photonic chip with the grating, we can record it with an imaging system that images the interferogram into a camera positioned far away from the chip. Another approach is to use a near field measuring system that can directly collect the light in close proximity to the chip.

3.3.1 Measure in the far-field with a scanning imaging system

In the preliminary experiments, we characterize the evanescent scattering based on-chip FTS with the far-field scanning imaging system.

3.3.1.1 Adapted horizontal coupling setup

We perform the measurements with an adapted horizontal coupling setup, which is designed to couple the light into and out from a photonic chip with the end-fire horizontal coupling. Figure 3.3 shows a photographic picture of the setup.

In order to couple the light in and out, two lensed fibers (LF) are installed on two 3-axis translation stages that are mounted on a rail along the y-direction. In between of the two 3-axis translation stages, there is a 2-axis translation stage (with translation axis along x- and z-direction). On top of the 2-axis translation stage, we use a vacuum chuck to hold the photonic chip in place. Above the photonic chip, we use an imaging system, consisting of an objective microscopy lens and a low noise Charge-Coupled Device (CCD) camera, to provide an optical view of alignment and also to measure the interferogram generated from the photonic chip.

As the imaging system has a limited field of view which is much smaller than the dimension of the interferogram, we need to scan it along the direction parallel to the direction of the on-chip FTS devices to cover the whole interferogram.

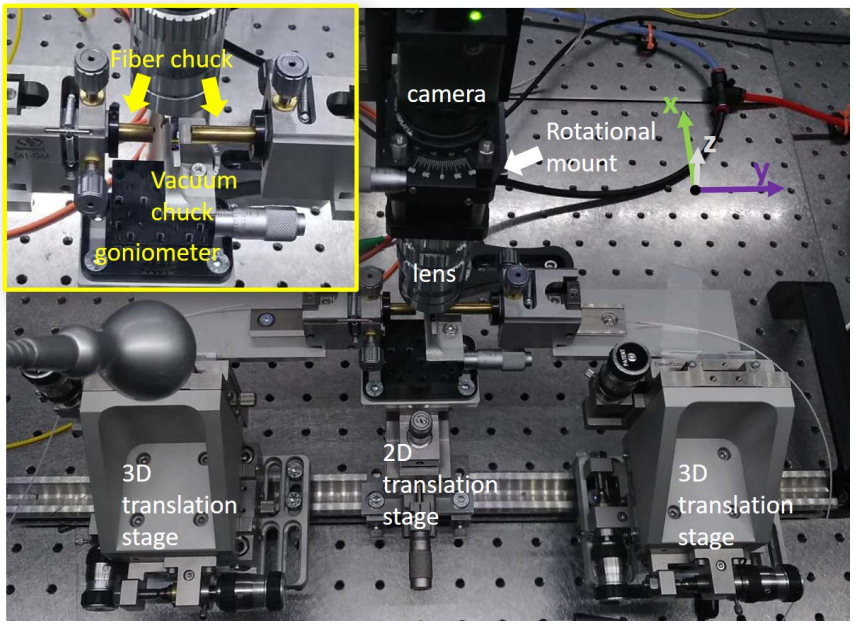

Figure 3.3: A photography picture of the horizontal coupling setup used in the far-field imaging approach. The inset shows a zoom-in focus on the fibers and chip holder.

To allow the scanning, we mount the objective lens on a 3-axis stage and attach the camera to the lens through a rotation mount. The purpose of the rotation mount is that we can rotate the camera so that the interferogram projected to the sensor inside the camera can be aligned to a particular row of pixel array. This makes it easier to extract the data of the interferogram from the images generated by the camera. Moreover, we also have a goniometer between the vacuum chuck, which holds the photonic chip and the 2-axis translation stage. The goniometer allows the rotation of the photonic chip around the x-axis, helping to parallel the interferogram to the sensor in the y-z plane. Here, and in the following discussion, we refer to the direction of the interferogram as the y-direction.

As such, we adapt the horizontal coupling setup and make it ready to measure the interferogram generated by the on-chip FTS. Although the setup contains two lensed fiber to couple in or out the light, we only need one side for launching the light into the chip. In figure 3.4, we show a simplified sketch of the complete setup. We use two lasers to provide various input spectral features. A polarization controller (PC) is assigned to each laser to provide independent polarization tuning. A 50:50 combiner is then applied to combine the two lasers. After proper alignment, the signal is horizontally coupled into our device by a lensed fiber (LF). The collection of the light is done by the imaging system hanging over the sample chip. As the imaging system scans across the interferogram, a series of images are taken, each containing a fragment of the interferogram. To reconstruct the complete interferogram, we have to stitch them together properly.

3.3.1.2 Disadvantages of the far-field scanning imaging approach

In practice, the approach mentioned above has some disadvantages. Firstly, the manual scanning is time-consuming and has low accuracy as well as low reproducibility. In order to capture the interferogram in a series of pictures, we manually rotate the corresponding micrometer drive to shift the imaging system with a fixed step length along the y-axis. Although we can try to parallelize the sensor to the interferogram in the y-z plane, it is needed to adjust the focus when the imaging system moves along the y-axis and reaches a new position. The reason is that, in order to obtain an interferogram with less distortion, all the fragments of the interferogram, as they are recorded in a series of images, should be equally well focused. Secondly, the objective lens of the imaging system limits the performance since it has chromatic aberration and field distortion to a certain degree.

As shown in figure 3.5, the chromatic aberration describes the wavelength-

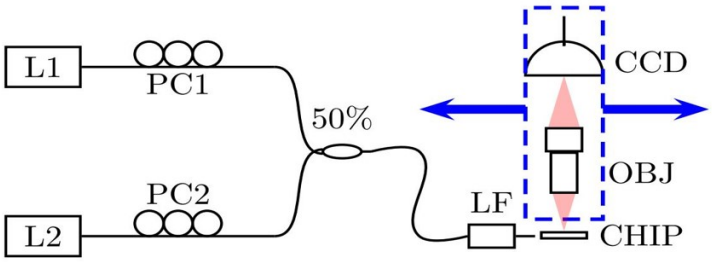

Figure 3.4: The setup used in the preliminary experiments, where we use a lensed fiber (LF) to couple the signal into the photonic chip and project the interferogram onto a CCD camera with an objective lens (OBJ). Two laser sources (L1 and L2) with the polarization controller (PC) can be applied simultaneously or individually. The CCD camera and OBJ (both shown inside the blue dash box) can move together to scan the whole interferogram. Reprinted from [1].

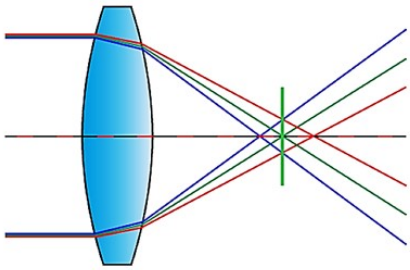

Figure 3.5: An illustration of longitudinal chromatic aberration, where light with different wavelengths focuses at different distances.

dependent focus distance. In our case, the chromatic aberration of the objective lens will make it difficult to focus the interferograms generated by light with different wavelengths at the same time. This can limit the bandwidth of the on-chip FTS.

The field distortion, as shown, for example, in figure 3.6, can either compress or stretch the image at the edge of the field of view. Since we are taking pictures for the interferogram, such distortions could potentially change the period of the interferogram at different locations in a picture, leading to the artificial side peaks in the calculated spectrum, as we will see later.

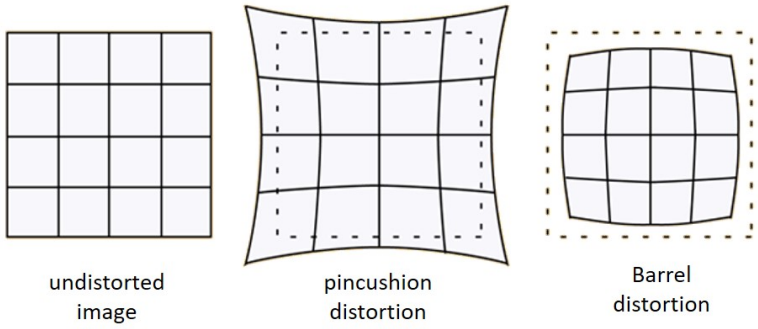

Figure 3.6: An illustration of different types of field distortion. [3]

3.3.2 Measure in the near-field with a fiber scanning system

In order to go beyond the limitations set by the manual scanning imaging system, we can collect the light directly at the near field. Intuitively, one might think to position a detector array, or a sensor, above the sample chip, as shown in figure 3.7.

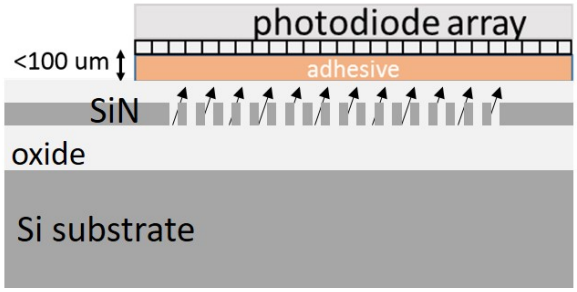

Figure 3.7: A sketch of near field detection where the photodiode array is brought into the close proximity of the chip.

However, this is practically difficult. Commercially available sensors typically have the detector pixels surrounded by a ceramic package and covered by a protective glass plate. As we need to approach the photonic chip to the detector pixels within a few tens of micrometers to prevent the interferogram from diverging too much, the ceramic package and the protective glass become problematic. Another problem is that, as the ceramic package blocks the four sides, there is no space for the lensed fiber to couple the light into the photonic chip. Furthermore, there are three other techni-

cal challenges: making the sensor parallel to the chip, blocking the stray light emitted from the lensed fiber and driving the sensor. Many attempts have been made to deal with these issues. In the end, we could not fix the malfunctions of the driver electronic boards, and have to explore a different approach.

3.3.2.1 Near-field fiber scanning system

Inspired by the Scanning Near-field Optical Microscopy (SNOM) [4], we built a simplified near field fiber scanning system. As shown in figure 3.8, with the setup, we can hold a fiber above the chip and drive it to automatically move along the interferogram, collecting light emitted from different locations.

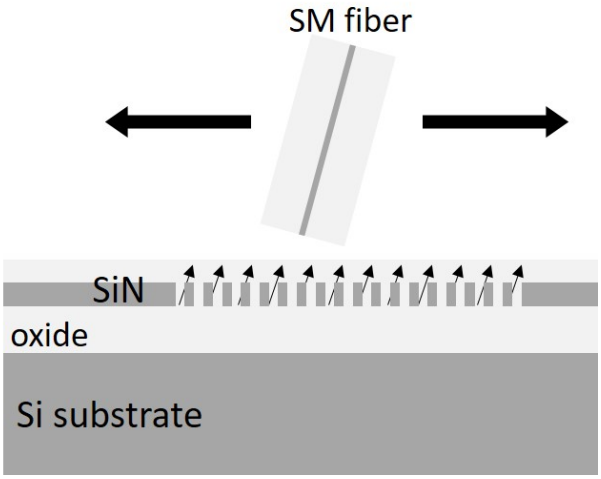

Figure 3.8: A sketch of near field detection by scanning a single-mode (SM) fiber above the interferogram.

We managed to build such a system with the high accuracy motion control stages, P-616 NanoCube® Nanopositioner and V-408 PIMag® Linear Stage, from PI (Physik Instrumente). The former provides 3-axis motion control with nanometer accuracy in the 100 μm range for each axis, while the latter allows large range (25 mm) linear motion along one axis with sub-micrometer accuracy.

In figure 3.9, we show the setup built around the fiber scanning system. The axis of V-408 defines the direction along which the interferogram should lie in. Consequently, we use a manual rotational stage to mount the vacuum

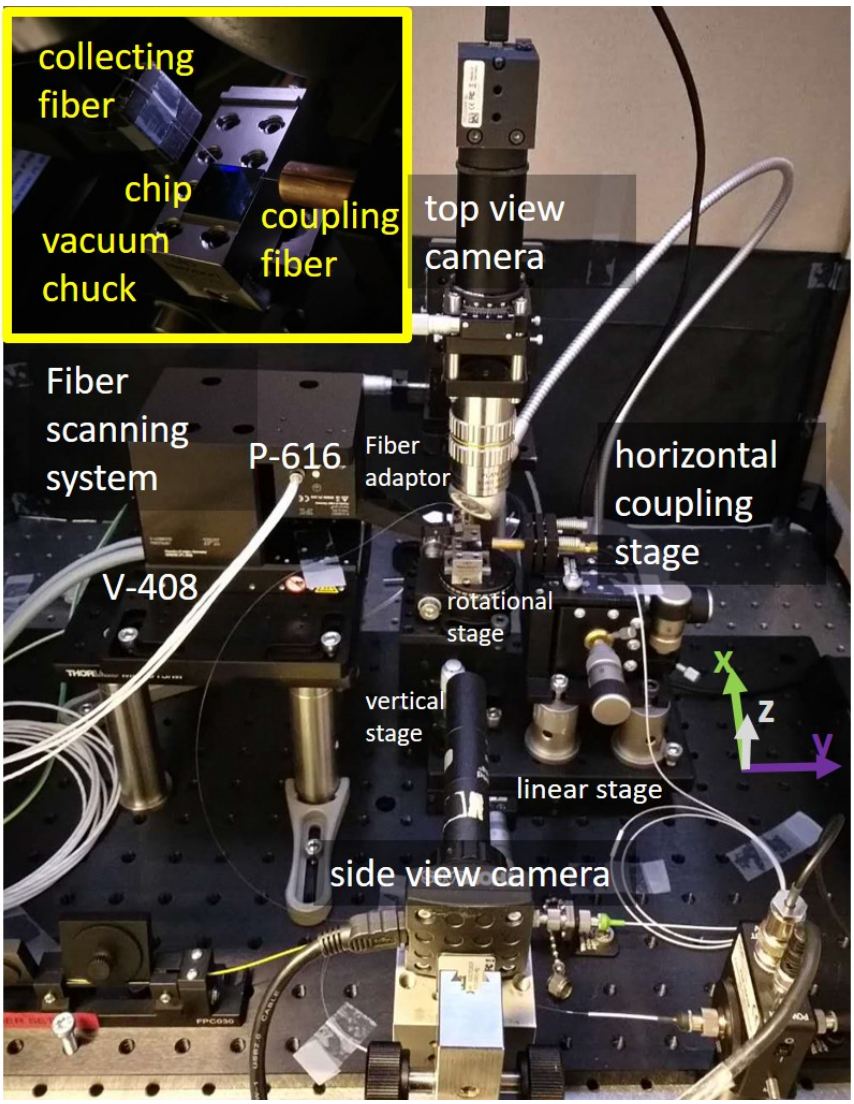

Figure 3.9: A photograph picture of the near field fiber scanning setup. The inset shows the zoom-in view focused on the collecting and coupling fibers as well as the chip and the vacuum chuck.

chuck, which holds the chip in place. Nevertheless, there is some tolerance to the parallelism, as we can use P-616 to correct the deviation. It is also important that the position of the chip in the z-direction should be adjustable as we need to approach the chip to the fiber tip within 100 μm so that P-616 can take over and move the fiber accurately towards the chip. This is done with the vertical translation stage, as shown in figure 3.9.

In order to couple the light into the chip, we install a lensed fiber on the 3-axis translation stage that is positioned on the opposite side of the fiber scanning system. As the fiber scanning system can not move in the y-direction, we put the horizontal coupling stage and the sample stage on a linear translation stage that travels along the y-direction. In this way, we can align the device under test coarsely to the fiber tip. Moreover, we have a top-view camera held above the sample stage to provide optical view for alignment and a side-view camera mounted on the side to monitor the fiber tip when we approaching the photonic chip to the fiber.

The fiber scanning system itself is built by stacking the P-616 on top of the V-408 with a specially designed bracket. As shown in the inset of figure 3.9, a 3D-printed fiber adaptor is used to install a lensed fiber on the P-616, which aims to collect the scattered light with a large numerical aperture (NA). The parallel-kinematic piezo system P-616 is specialized in photonics related nano-positioning when used together with the driver E-712 digital piezo controller (from PI). The latter offers built-in firmware based fast alignment routine which provides a spiral or sinusoidal scan to find the position of the global intensity maxima of the measured signal in an area (2-axis scan) or along one line (1-axis scan) [5].

As an example, we show in figure 3.10, the intensity distribution of the light field scattered from the photonic chip that contains the interferogram generated from our on-chip FTS device. This figure, obtained with a 2-axis scan using the fast alignment routine, shows five periods of a sinusoidal interference pattern generated by a monochromatic input signal. It is also noticeable that the interferogram is not precisely in parallel with the y-axis of the P-616.

3.3.2.2 Procedure of the manual alignment

In order to obtain the image, as shown in figure 3.10, the whole setup needs to be aligned. The near field scanning approach requires some alignment steps. The procedure is shown in figure 3.11.

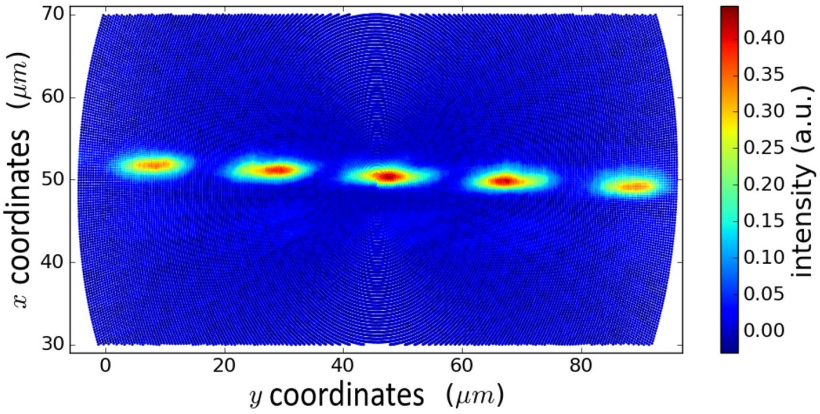

Figure 3.10: Power of the scattered light collected by the lensed fiber at different location, using the 2-axis fast alignment routine.

- As both V-408 and P-616 have integrated distance sensors, they need to be referenced and zeroed at the startup, which requires movements in a large physical range. As a result, during the initialization, the photonic chip should be lowered to avoid any potential collision.

- After initialization, we raise the chip, approaching it to the fiber tip while still leaving some safety space. This step is done in the side view provided by the side camera.

- In this step, we need to align the edge of the photonic chip, as it is parallel to the on-chip FTS devices, to the travel axis of V-408. We drive the V-408 to move the fiber tip from one side of the photonic chip to the other side and tune the rotational stage so that the edge for the chip is aligned roughly to the trajectory. It is not necessary to align with very high accuracy since the P-616 can correct the deviation if it is within a few tens of micrometer.

- After the previous alignment, we can couple the light into the chip with the 3-axis horizontal coupling stage. When the light is coupled into one of the devices, bright light scattered out from the device can be observed from the top-view camera. This is the interferogram to be measured.

- With the light coupled into the chip, we move the top-view camera to find the image of the collecting fiber tip and move the linear stage that carries both the sample stage and the coupling stage. We need

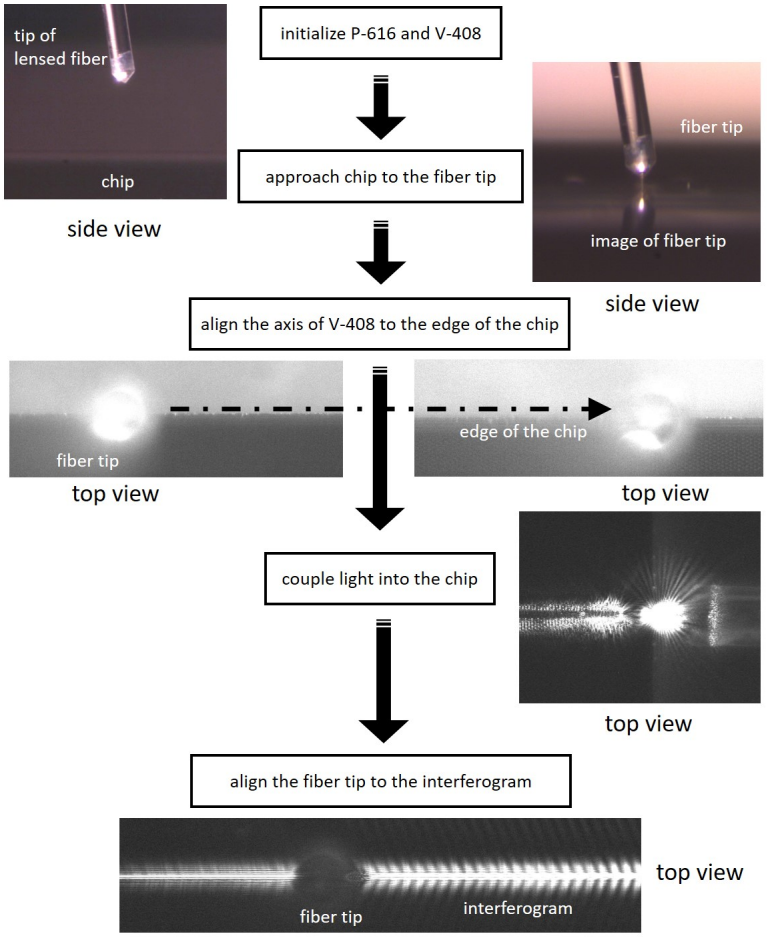

Figure 3.11: Flow chart of the manual alignment procedure.

to tune the linear stage so that the interferogram lies in the middle of the fiber tip (in the camera view from the top).

Now the manual alignment is finished. From this point, we continue with the software PIMikroMove, which controls the movement of V-408 and P-616.

3.3.2.3 Fiber scanning routine

The fiber scanning routine is written as a python script with the instruction set provided in the PIMikroMove. In figure 3.12, we summarize the steps of the fiber scanning routine.

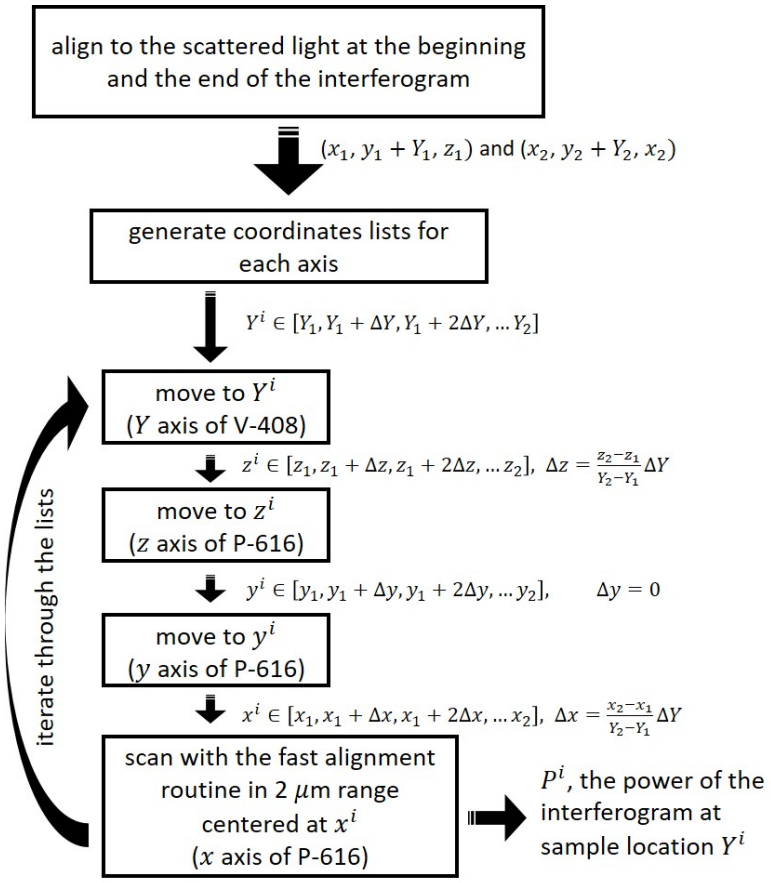

Figure 3.12: Flow chart of the fiber scanning routine.

To scan the fiber tip over the interferogram, the first step is to get the fiber tip aligned to the scattered light at a start point (x_1, y_1+Y_1, z_1) and an endpoint (x_2, y_2+Y_2, z_2). Y_1 and Y_2 are the coordinates of the start point and endpoint on the travel axis Y of V-408. The difference, $Y_2 - Y_1$, should equal to the length of the interferogram that we want to measure.

The coordinates with lower case letters are associated with the three axes of P-616. We set y_1 equals to y_2 so that the sample step length is determined by the step length ΔY with which the V-408 moves from Y_1 to Y_2. Typically, x_1 is not equal to x_2 to compensate the lateral deviation, since the Y axis of V-408 is not perfectly parallel to the interferogram. Also, as the chip is not accurately horizontal, z_1 is not equal to z_2 to compensate the varying distance between the tip of the lensed fiber and the surface of the chip.

With a proper sample step length ΔY, the lists of coordinates are generated and sent to the driver to assign to the corresponding axes. In practice, directly assign a coordinate value to the x axis of P-616 might not be enough to find the peak intensity at a specific Y^i position. Therefore, we send the coordinate value x^i to the fast alignment routine (1-axis) as the central coordinate. As such, for every Y^i position, we ask the software to run a scan along x axis (in a 2 μm range centered at x^i) to find the peak power value P^i, which gives the intensity of the interferogram at each sample point.

So far, we covered the different measuring approaches applied in characterizing the on-chip FTS. In the next sections, we will present and discuss the measurement results obtained from these approaches.

3.4 Preliminary experimental results obtained with the far-field imaging approach

In the preliminary experiments, the aforementioned horizontal coupling setup is used to characterize the evanescent scattering based on-chip FTS with the far-field imaging approach. The on-chip FTS devices discussed in these experiments are implemented on the BioSin4 platform, where the SiN layer has a thickness of 220 nm.

3.4.1 Measurements with input of one spectral line

We first consider the input of 895 nm monochromatic light beam emitted from a TLB-6318 tunable laser (Newport, tuning range 890-910 nm). The imaging system captures the interferogram generated from the on-chip FTS, creating pictures that are shown in figure 3.13 (a) and (b). In the pictures, the interferogram exhibits the feature of a periodic bright-to-dark pattern. From the pictures, we can then extract the intensity profile of the interferogram, as shown in figure 3.13 (c).

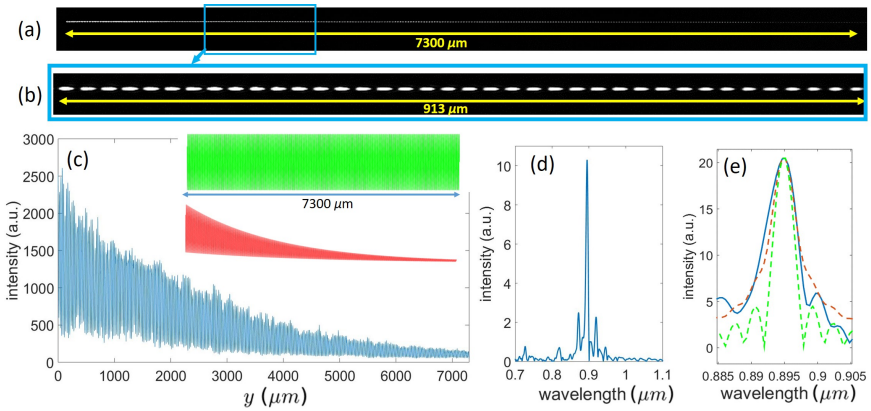

Figure 3.13: (a) The interferogram reconstructed by stitching eight snapshots taken by the scanning imaging system. (b) One of the snapshots covering the length of 913 μm as limited by the field of view. (c) The intensity profile extracted from the measured interferogram. The inset shows the computed perfect sinusoidal interferogram with the same period and total length as the measured one with (red) and without (green) exponential decay. (d) The spectrum calculated from the measured interferogram as shown in (c). (e) The zoom-in of the spectrum displayed in (d) and the green and red spectra calculated from the simulated interferogram.

As expected, an exponential decay superposed on the interferogram can be observed, resulting from a continuous grating strength. In order to decode the spectral content of the injected light from the interferogram, we use the Fast Fourier Transform (FFT) function (in Matlab or Python) to calculate the Discrete Fourier Transform (DFT).

As introduced, the interferogram is generated in a stretched way and the OPD can be calculated from the propagation distance y with

$$OPD = \Delta n_{eff} \cdot y, \tag{3.1}$$

where Δn_{eff} is the difference in effective indices. For the input interferogram recorded as a function of y, the calculated spectrum should have wavenumber axis,

$$\nu = \frac{\Delta n_{eff}}{\lambda}. \tag{3.2}$$

With a proper value of Δn_{eff}, the resulted spectrum can be mapped onto the wavelength axis. In order to match the position of the peak as shown in figure 3.13 (d) to the known laser source wavelength, we choose a Δn_{eff} value of 0.0376, which is not far away from the simulation value 0.0387.

Once we know the value of Δn_{eff}, we can theoretically calculate the resolution to be 3.5 nm. However, the Full Width Half Maximum (FWHM) of the main peak in figure 3.13 (d) is measured to be around 6 nm. In order to investigate the broadening, we calculated the Fourier transform of a perfect sinusoidal interferogram with the same period for two cases. These perfect sinusoidal lines are shown in the inset of figure 3.13 (c) for the case (in green) that there is no power decay and for the case (in red) where the same decay rate applies as in the measured interferogram. The resulting spectra coded with the corresponding color are plotted in the inset in figure 3.13 (d). The theoretical value of 3.5 nm FWHM is observed from the green spectrum, while the red one has an FWHM of 5.5 nm. From this, we can conclude that the broadening is mainly resulting from the exponential decay superimposed on the sinusoidal interferogram pattern.

3.4.2 Measurements with input of two spectral lines

We also tested the devices with a signal that contains two spectral lines. The signal is generated by combining the laser light emitted from the TLB-6318 (with linewidth $<$ 5 MHz) and another ultra-narrow linewidth Continuous Wave (CW) Ti: Sapphire laser (M2lasers, tuning range 710-975 nm and linewidth $<$ 5 MHz).

In figure 3.14, we present two sets of experimental results, each including the stitched intensity profile of the interferogram, one of the snapshots taken by the CCD camera and the calculated spectrum mapped to the wavelength axis.

So far, we demonstrated the basic operation of the on-chip co-propagative stationary FTS in both monochromatic and polychromatic cases. While the results seem to be promising, there is still space for improvement.

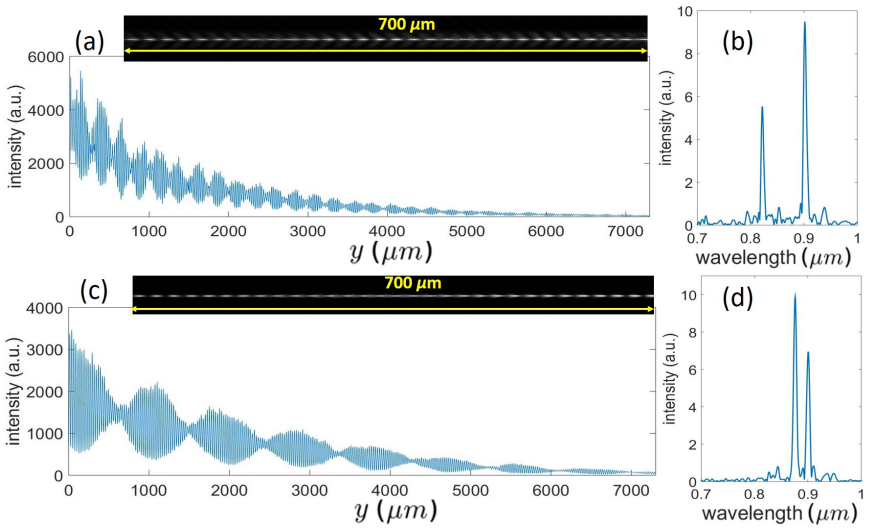

Figure 3.14: Two sets of experimental results obtained with scanning imaging system considering a signal generated by two laser lines. The recorded interferogram (a) and the calculated spectrum (b) comes from the input laser light of 822 and 900 nm. The recored interferogram (c) and the calculated spectrum (d) are for 876 and 900 nm laser lines. The insets show the snapshots as observed from the CCD camera. The figure is reprinted from [1].

Firstly, in all the spectra we obtained, there are some unexpected small bumps and peaks which we think could be related to the various distortions of the interferogram introduced by the measuring approach. As mentioned before, the scanning imaging approach has quite some drawbacks. Manually scanning and refocusing the imaging system is not only time-consuming but also can introduce distortion to the interferogram. Stitching the fragments of the interferogram together can be another source of distortion.

Besides, as can be observed, the exponential decay is much more rapid than expected, leading to a considerable broadening of the main peak. As the camera sensor is not strictly in parallel to the photonic chip, the focus at one side of the field of the view could be different from that at the other side. This leads to an interferogram fragment that has a strong average intensity on the one side and linearly decays to the other side. When the fragments are stitched to reconstruct the complete interferogram, the artificial decays in each fragment are accumulated, resulting in a greatly exaggerated exponential decay. It is always possible to compensate and remove the decay by

data processing so that the broadening can be avoided. However, it should be noted that data processing will inevitably amplify the high frequency noise to some extent as the SNR degrades at larger OPD. In this work, instead of exploring the details of data processing, we are more interested in characterizing the intrinsic performance of the proposed on-chip FTS.

3.5 Experimental results obtained with the near-field fiber scanning approach

In order to improve the performance, we need to get rid of the imaging system and measure from the near field, i.e., a few tens of micrometers above the photonic chip. We developed the near field fiber scanning system, which relies on high accuracy automatic scanning instruments and should introduce less distortion. In the meanwhile, we moved on to the 300 nm BioPIX platform where we prototyped both types of the on-chip FTS. In this section, we present the detailed measurement results.

3.5.1 Measurements of a monochromatic signal

In the experiments, we first examine the evanescent-scattering based on-chip stationary FTS with the input signal of the monochromatic light emitted by the Ti: Sapphire laser. The interferogram generated by an 890.5 nm laser line is measured in the form of an intensity curve recorded as a function of the propagation distance y (up to 8408 μm), containing 1052 points with the sample step length of 8 μm. After removing the offset, the interferogram oscillating around zero intensity is shown in figure 3.15 (a). Fast Fourier transform (FFT) is applied in Python to calculate the spectrum, which is then mapped to the wavelength axis. With Δn_{eff} = 0.0431, we show that we match the calculated peak wavelength to the wavelength of the laser line.

3.5.1.1 Zero-padding

The spectrum calculated by applying FFT to the 1052-point interferogram also has 1052 data points. While information theory indicates that it contain all the information required to completely reconstruct the spectrum, it is often preferred to have two or more data points per resolution element

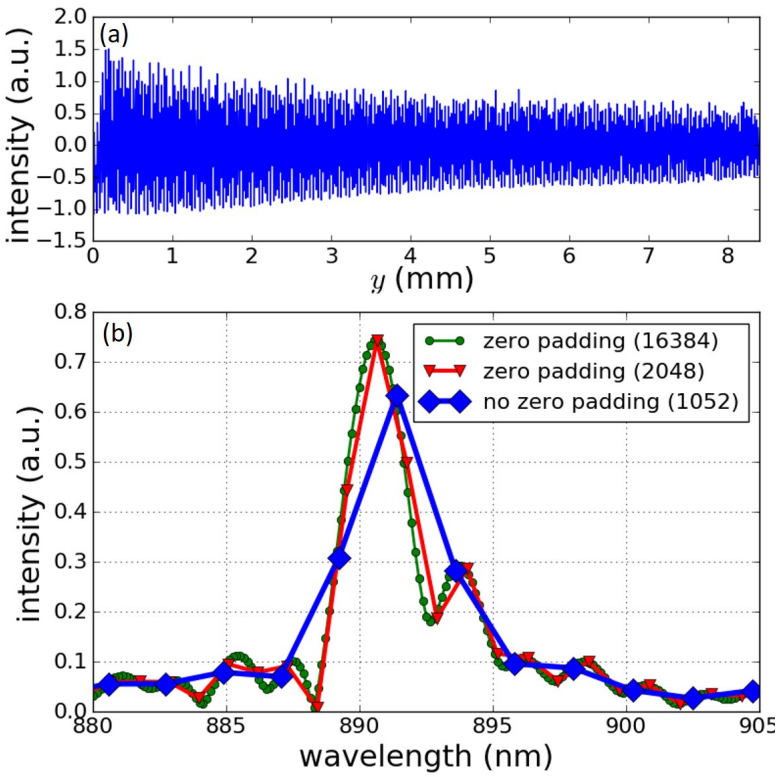

Figure 3.15: (a) The interferogram measured from the evanescent-scattering based on-chip FTS, considering a single wavelength signal. The interferogram is centered around 0 intensity as we subtracted the average. (b) The spectra calculated with the interferogram considering different amount of zero padding.

so that adjacent features can be better resolved visually [6]. To interpolate the spectrum, one of the most useful approach is zero-padding. Zero padding simply refers to adding zeros to the end of a time-domain signal to increase its length. The spectrum calculated with the 1052-point interferogram is shown with the blue curve in figure 3.15 (b). By adding zeros to the end of the measured interferogram, while there is no additional information added, we increases the length of the interferogram, which leads to an increased sample rate in the wavelength space [7]. The advantage is that we can accurately determine the peak position with a reduced FWHM of the peak. As presented by the red line in figure 3.15 (b), with the interferogram zero-padded to 2048 (2^{11}) points, the peak position can already be accurately determined. Further padding to 16348 (2^{14}) points leads to a

much smoother spectrum, as shown by the green curve.

3.5.1.2 Side-lobes

In figure 3.15 (b), one can also see a side peak at around 893 nm. It is interesting to investigate whether this side peak contains real spectral information or it is only the side-lobe of the main peak. In figure 3.16 (a), we show the spectra calculated with the full interferogram (with all 1052 data points) and a part of the interferogram (with the first 800 data points). We can see that while the shifting of the main peak centered at around 890.5 nm is negligible, the side peak is shifted considerably.

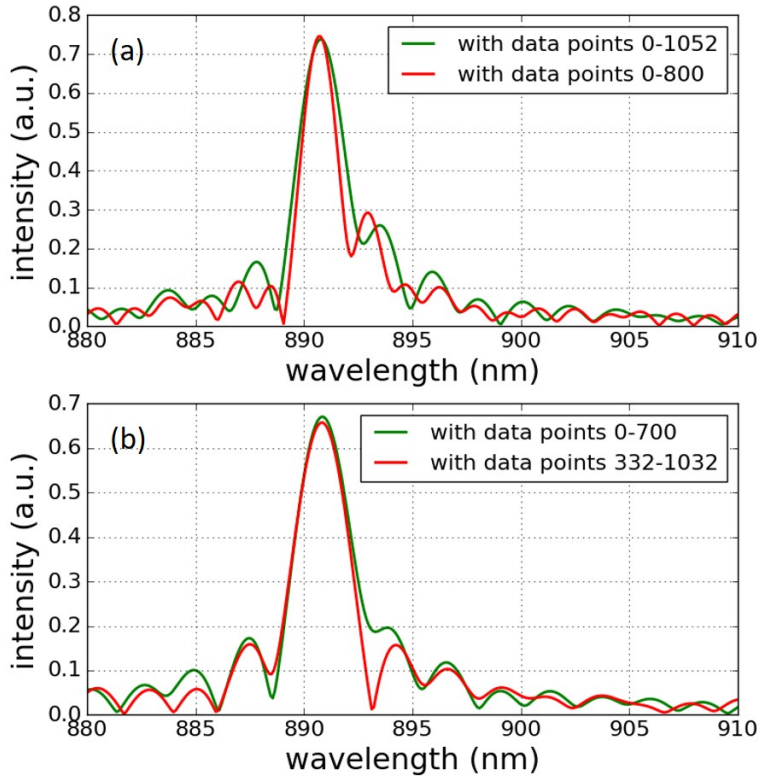

Figure 3.16: The spectra calculated from the different fragment of the interferogram, as shown in figure 3.15 (a). In (a), the spectra obtained from a long (data points 0-1052) and a short fragment (data points 0-800) are compared to show that the side-lobe shifts while the main peak stays still. In (b), the spectra obtained from interferogram fragments that cover the same length but different locations are compared to show the different shape of side-lobes.

Besides, the spectra calculated with different fragments of the interferogram have a different shape of the side-lobes. This can be seen in figure 3.16 (b), where we show the spectra calculated from two different fragments with the same length. While the main peaks almost overlap with each other, the side peaks are quite different. These simulations indicate that the side peak is only the side-lobe of the main peak. In principle, as the side-lobes of a sinc line-shape are symmetric about the main-lobe, we should also see symmetric side-lobes here. However, the spectra obtained from our on-chip FTS have asymmetric side-lobes. Although we have made efforts to understand the asymmetry, we could not find a clear answer. In the end, what we can conclude is that the side peak is a side-lobe instead of a physical spectral feature.

3.5.1.3 Higher resolution

The resolution measured as the FWHM of the main peak shown in figure 3.15 (b) is 2.71 nm. This is already very close to the theoretical value of 2.64 nm, calculated according to equation 2.4. Nevertheless, as mentioned already in Chapter 2, in principle, we can obtain an even higher resolution from the interferogram. As introduced in section 2.2.1, the interferogram measured from our on-chip FTS is a one-sided interferogram that only contains positive OPD part. For such a one-sided interferogram, the resolution could be calculated with equation 2.4 as the reciprocal of the maximum OPD. However, in principle, we can obtain a higher resolution.

To illustrate this, let us consider a one-sided interferogram that starts from the zero OPD point and measures up to an OPD of $+L$. As the DFT computes both the cosine and the sine Fourier transforms, such an interferogram is effectively treated as the linear combination of an even and odd component. Mathematically, a cosine function $f(x)$ with constant amplitude of 1, extending from 0 to $+L$ is equivalent to the superposition of an even component $f_e(x)$ that has a constant amplitude of 1/2 extending from $-L$ to $+L$, and an odd component $f_o(x)$ with amplitude of -1/2 from $-L$ to 0 and +1/2 from 0 to $+L$. We can write these in equation 3.3. According to Fourier transform theory [8], the Fourier transform of the real-and-even function $f_e(x)$ is pure real and even, and the Fourier transform of the real-and-odd function $f_o(x)$ is pure imaginary and odd. Therefore, the Fourier transform of the one-sided interferogram (with the OPD from 0 to $+L$) should give a complex spectrum containing both a real part and an imaginary part. By taking the absolute values of the complex spectrum, we get an absolute spectrum where the peak has an FWHM of $\sim 1.207/L$. However, if we

only use the real part of the resulting complex spectrum, we can get a real spectrum which gives the spectral peak with an FWHM of $\sim$1.207/(2L). This 1/(2L) resolution corresponds to the even component $f_e(x)$ that extends from OPD of -L to OPD of +L, as written in equation 3.3. It should be noted that, to be able to extract the 1/(2L) resolution from the real spectrum, the one-sided interferogram needs to start exactly from the zero OPD point. There are no phase errors in this ideal case. However, in practice, we usually do not know where exactly the zero OPD point is. When we fail to start the recording of the interferogram from the zero OPD point, phase errors arise and we are effectively multiplying a phase term to the complex spectrum obtained from the phase-error-free interferogram [9]. For the interferogram generated by a monochromatic source, we can simply multiply the complex spectrum with an additional phase term (wavelength-dependent) $e^{i\phi(\lambda)}$ to correct the phase error.

$$
\begin{aligned}
f(x) &= f_e(x) + f_o(x) \\
f(x) &= \begin{cases} \cos x, & \text{if } x \in [0, L]. \\ 0, & \text{otherwise.} \end{cases} \\
f_e(x) &= \begin{cases} \frac{1}{2}\cos x, & \text{if } x \in [-L, L]. \\ 0, & \text{otherwise.} \end{cases} \\
f_o(x) &= \begin{cases} -\frac{1}{2}\cos x, & \text{if } x \in [-L, 0). \\ \frac{1}{2}\cos x, & \text{if } x \in [0, L]. \\ 0, & \text{otherwise.} \end{cases}
\end{aligned}
\tag{3.3}
$$

The interferogram obtained from our on-chip FTS is a one-sided interferogram, as introduced in section 2.2.1. In figure 3.17 (a), we plot the absolute spectrum and the real spectrum calculated from the measured interferogram. To obtain the two spectra, we multiple the complex spectrum with a phase shift term (ϕ=180^o) and respectively take its absolute value and real value. It can be observed that, in the real spectrum, the peak is about half as broad as the one in the absolute spectrum. The phase shift term serves the purpose of phase correction and can affect the shape of the real spectrum. When it is not chosen correctly, it would be difficult to determine the peak position and the resolution. For example, by multiplying a phase shift term with ϕ=90^o to the complex spectrum, we obtain a real spectrum and an absolute spectrum as shown in figure 3.17 (b). We can see, a phase shift term with ϕ=180^o is a better choice compared to ϕ=90^o.

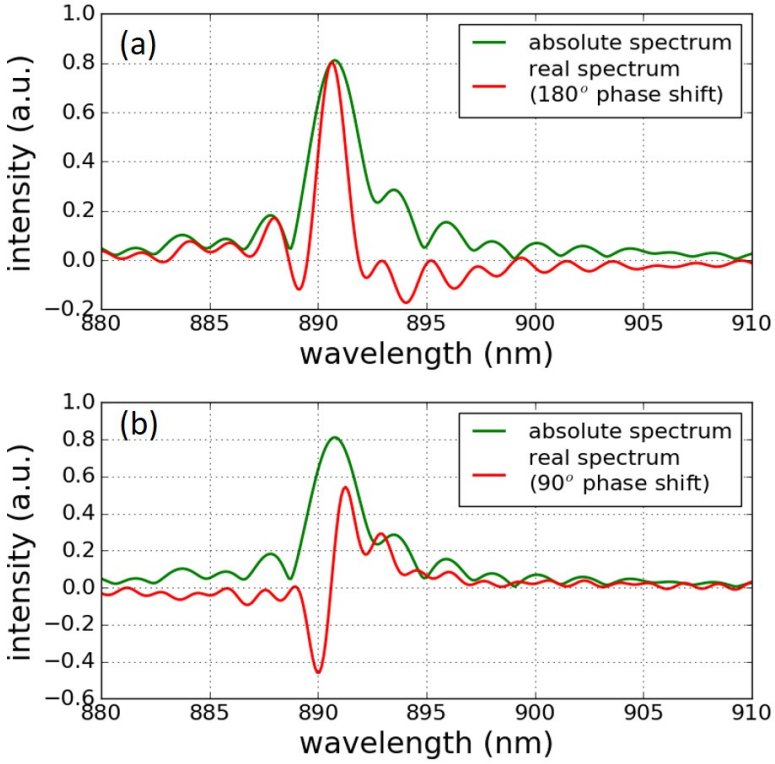

Figure 3.17: The absolute and real spectra calculated with the interferogram shown in figure 3.15: (a) the real and absolute spectra are obtained from the complex spectrum (the output of the FFT) that is phase shifted by ϕ=180^o, (b) the real and absolute spectra are obtained from the complex spectrum that is 90^o phase shifted. In case (a) the FWHM of the peak in the real spectrum is about half of that of the absolute spectrum.

Generally speaking, for one-sided interferogram, by looking into the real spectrum, we can obtain a higher resolution than that is defined by equation 2.4. However, we need to have a very good handle on where the zero OPD point is, and what the instrument phase response is. Ideally, the zero OPD point of all frequency components should be put to the origin, otherwise phase errors will be introduced. For monochromatic input light, it is relatively easy to correct the phase error. However, in the case of polychromatic light, the situation becomes complicated, as every wavelength component could have a different phase-shifting term. In order to use the real spectrum without introducing distortions, a broadband phase correction should be performed to shift the zero OPD point of all the cosine compo-

nents (with different periods) to the starting point of the interferogram. In this sense, it is always safer to stick to the absolute spectrum, although it has a relatively low resolution.

3.5.1.4 Characterize the evanescent-scattering based on-chip stationary FTS in a wide wavelength range

Furthermore, we characterized the evanescent-scattering based on-chip stationary FTS using the monochromatic signal with several other wavelengths in the range from 780 nm to 980 nm. Figure 3.18 shows the interferogram and the corresponding calculated spectra. This shows that our on-chip FTS is operational in at least 200 nm bandwidth from 780 nm to 980 nm. From figure 3.18, we can see that the interferogram has a wavelength-dependent decay rate. This is because the confinement of the optical power in a waveguide varies with the wavelength.

For short wavelengths, the guided mode is more confined in the core region and therefore is less subject to the perturbation introduced by the grating units. As a result, the gratings only scatter a relatively small portion of optical power from the guided mode. While this leads to a low decay rate, it limits the amount of light that can be detected by the recording system. The former is preferable as it leads to less spectral broadening. The latter, however, can be a problem, resulting in a weak spectrum that has degraded SNR.

One the other hand, for the light with long wavelengths, the guided mode is less confined. Consequently, the optical mode is more subject to the scattering of the grating units, leading to a relatively large decay rate. This would broaden the peak in the spectrum. When the decay rate is too large, this can even limit the maximum measurable OPD and eventually reduce the resolution.

In table 3.1, we summarize the difference in effective refractive indices Δn_{eff} used in the calculation of the spectra, the theoretical FWHM calculated with equation 2.4, the measured FWHM estimated from the calculated spectra and the broadening percentages for different wavelengths. In principle, we can use these wavelength-dependent values (Δn_{eff} and broadening percentages) to correct the calculated spectrum for broadband input signals.

From figure 3.18, we can also get a clue about what is limiting the operational bandwidth. On the long wavelength side, as the decay rate increases rapidly, the peak is considerably broadened, resulting in a reduced resolution. On the short wavelength side, there are two limiting factors. One is

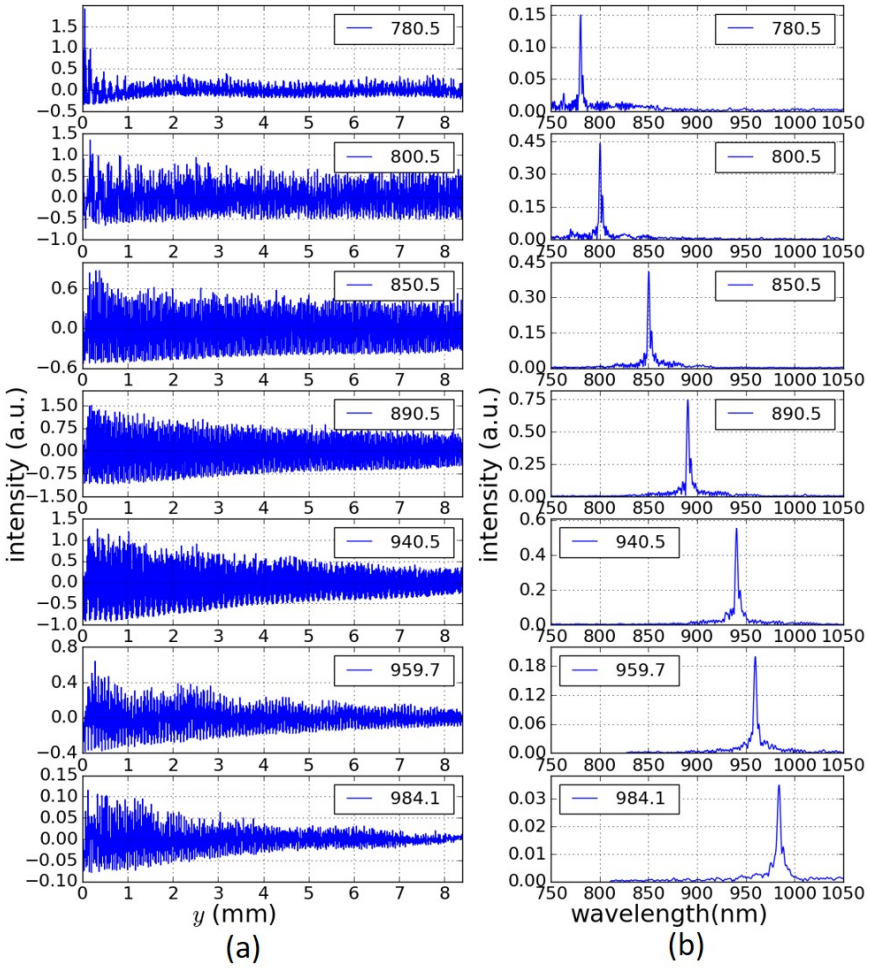

Figure 3.18: (a) Interferograms generated by the monochromatic signal with different wavelength measured with the evanescent-scattering based on-chip stationary FTS. (b) the corresponding spectra calculated with the measured interferograms.

the weak signal strength, which leads to a bad SNR. The other one is that, as the wavelength becomes short, the wide waveguide of the FTS will start to support higher order modes. This is already happening from light with a wavelength of 780.5 nm. The rapid decay at the beginning of the interferogram is evidence of the high order mode. While the high order mode is supported by the waveguide, it is confined very loosely and thus, scattered

wavelength	Δn_{eff}	theoretical FWHM	measured FWHM	broadening
780.5 nm	0.04411	1.98 nm	2.00 nm	1.0%
800.5 nm	0.04412	2.09 nm	2.12 nm	1.4%
850.5 nm	0.04375	2.39 nm	2.42 nm	1.3%
890.5 nm	0.04313	2.64 nm	2.71 nm	2.7%
940.5 nm	0.04196	3.03 nm	3.25 nm	7.3%
959.7 nm	0.04138	3.20 nm	3.50 nm	9.4%
984.1 nm	0.04058	3.43 nm	4.28 nm	24.8%

Table 3.1: List of the values related to the peaks shown in the spectra in 3.18

significantly by the grating units.

3.5.1.5 Characterize the lateral-leakage based on-chip stationary FTS in a wide wavelength range

Using the near-field fiber scanning setup, we also measured the response of the lateral-leakage-based on-chip stationary FTS with a monochromatic laser line at several wavelengths. The interferogram measured from the lateral-leakage based on-chip stationary FTS only has a length of about 8.1 mm, as we only have limited space where we can put the designs.

In the measurement, we also use the tunable Ti: Sapphire laser as the light source to provide monochromatic light with different wavelength. The measured interferogram and the corresponding spectra are shown in figure 3.19. As discussed already in chapter 2, the curve of leakage rate has a rather steep slope as a function of wavelength. This has two consequences. On the one hand, a large leakage rate at long wavelengths leads to a large rate of the exponential decay superposed on the interferogram. As we can see from the interferograms in figure 3.19, at the wavelength of 916 nm, the decay rate is much more rapid even when compared to that of the interferogram generated from the evanescent-scattering based on-chip stationary FTS with a 984.1 nm input signal. The result is a significantly broadened spectral peak and a greatly reduced resolution. On the other hand, at the short wavelength side, the small leakage rate means only a minimal amount of optical power can be coupled into the slab modes, leading to a weak spectrum with a bad SNR. This is the case for the spectrum with an 815 nm peak, as shown in figure 3.19.

Again, in table 3.2, we listed the Δn_{eff}, the theoretical FWHM, the mea-

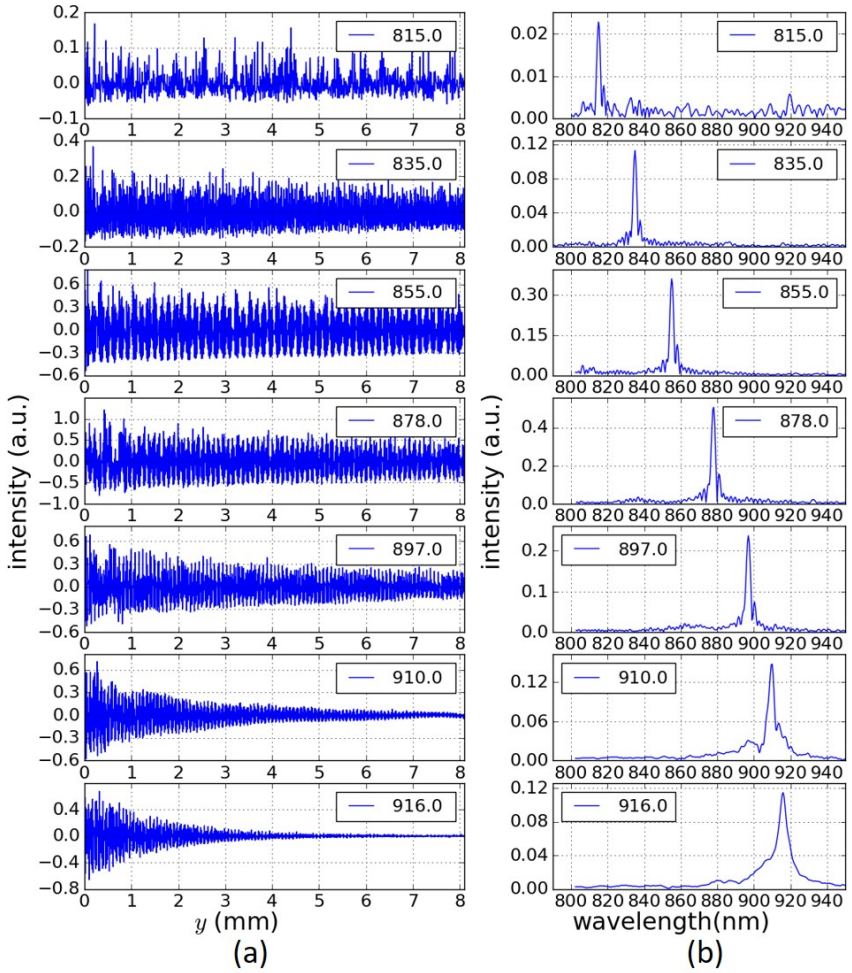

Figure 3.19: (a) The interferograms generated by the monochromatic signal with different wavelength measured with the lateral-leakage based on-chip stationary FTS. (b) the corresponding spectra calculated with the measured interferograms.

sured FWHM, and the broadening percentages for the different wavelengths considered. For the measurements, we can conclude that the dispersive nature of the lateral leakage mechanism limits the operational bandwidth by decreasing the resolution at the long wavelength side and by degrading the SNR at the short wavelength side.

wavelength	Δn_{eff}	theoretical FWHM	measured FWHM	broadening
815 nm	0.04440	2.23 nm	2.28 nm	2.24%
835 nm	0.04457	2.33 nm	2.39 nm	2.58%
855 nm	0.04458	2.44 nm	2.51 nm	2.87%
878 nm	0.04465	2.57 nm	2.67 nm	3.89%
897 nm	0.04462	2.69 nm	2.85 nm	5.95%
910 nm	0.04460	2.77 nm	4.28 nm	54.51%
916 nm	0.04449	2.81 nm	6.83 nm	143.1%

Table 3.2: List of the values related to the peaks shown in the spectra in 3.19

3.5.2 Measure with a broadband signal

After examining the on-chip FTS with the monochromatic light signal, we continue to characterize the devices with a broadband light source. We construct the broadband signal by filtering the supercontinuum light with a free space band-pass filter. For example, with the band-pass filter (FB850-10, THORLABS) that has 10 nm pass-band centered around 850 nm, we measured the interferogram generated from the evanescent-scattering-based on-chip stationary FTS.

The measured interferogram, shown as the red curve in figure 3.20 (a), has a baseline which transforms to a big DC peak at 0 frequency (or $+\infty$ wavelength) in the Fourier domain. It is better to remove the baseline, as the side-lobes of the DC peak can sometimes extend to the interested wavelength range. To remove the baseline, we fit the measured interferogram with a fourth degree polynomial and subtract the result from the measured interferogram. The resulting interferogram centered around zero intensity level is shown in 3.20 (a) in green, from which we can then calculate the spectrum, as shown in 3.20 (b).

We also measured the same broadband signal with the lateral-leakage-based on-chip stationary FTS. Similarly, we remove the baseline and obtain the interferogram, as shown in 3.21 (a). From the interferogram, we calculate the spectrum as shown in figure 3.21 (b). To study the reconstructed spectra, we measured the spectrum of the input light with a bench-top optical spectrum analyzer (OSA). The spectra are shown in figure 3.22. In comparison, we notice that the spectrum obtained with our on-chip FTS is noticeably broadened with relative to the expected 10 nm FWHM. Also, as confirmed by multiple measurements, the spurious ripples appeared on spectra were

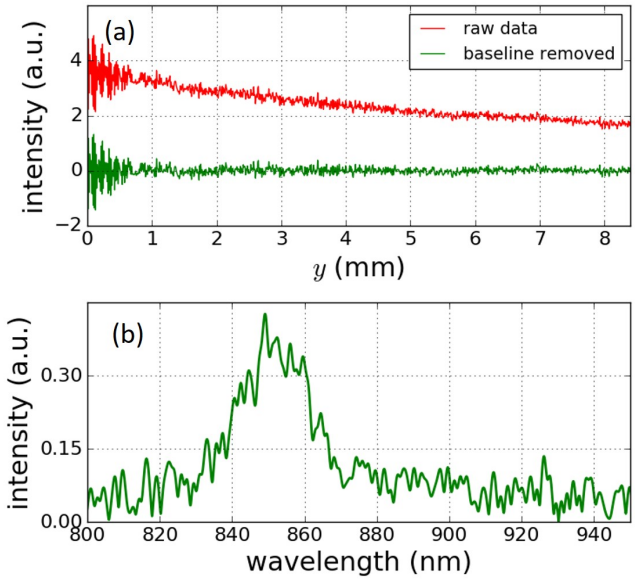

Figure 3.20: (a) The interferograms (before and after removing the baseline) generated by a broadband signal from the evanescent-scattering based on-chip stationary FTS. (b) The calculated spectrum mapped to the wavelength axis.

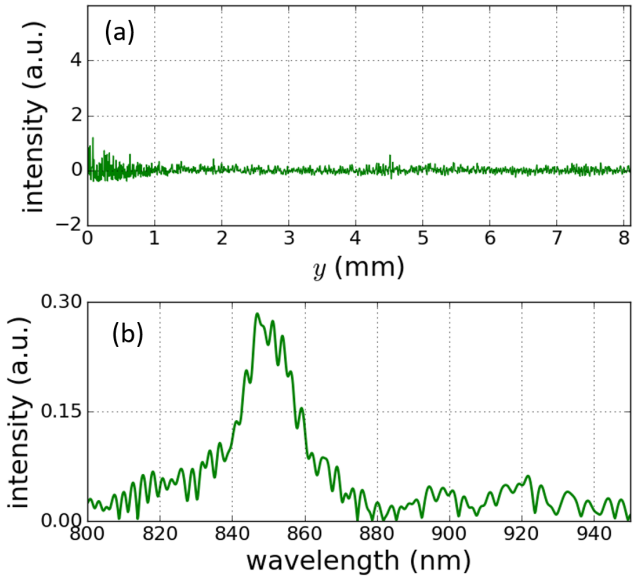

Figure 3.21: (a) The interferogram (with baseline removed) generated by a broadband signal from the lateral-leakage based on-chip stationary FTS. (b) The calculated spectrum mapped to the wavelength axis.

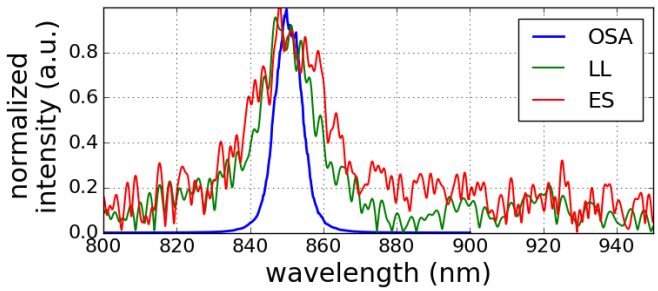

Figure 3.22: Normalized spectra measured with a bench-top optical spectrum analyzer (OSA) and with the evanescent-scattering-based (ES) and the lateral-leakage-based (LL) on-chip stationary FTS.

stochastic, thus come from the noise. The spectra we measured have an impaired SNR as compared to the spectra measured with the OSA. In the following two section, we will discuss about the broadened spectral peak and the impaired SNR.

3.5.2.1 Broadening of the spectral peak

Intuitively, one might think the broadening is due to the fact that our on-chip FTS has a limited resolution, as discussed in the experiments with a monochromatic source. However, that is not enough to explain such a large broadening.

When the monochromatic input signal is considered, according to equation 2.1, the interferogram is a cosine-like line shape that extends infinitely. After Fourier transform, this will gives a delta peak with infinitely small line width. The fact that we can only measure a limited length of the interferogram leads to a limited resolution and broadening of the delta peak. It is worth to mention that, in principle, the FWHM of the spectral peak is solely determined by the length of the recorded interferogram, no matter which part of the cosine line shape is recorded. We also demonstrated that the exponential decay superpositioned on the interferogram resulting in spectral broadening. As shown in figure 3.19, a rapid decay could lead to a considerable broadening.

For the case where the broadband signal is considered, the interferogram is no longer a simple cosine line shape, and things become different. Usually, in the interferogram generated by a broadband signal, one can see a burst of central fringes with large modulation amplitude around the ZPD where all the cosine components are in phase and therefore can add up constructively. These central fringes are often referred to as the centerburst [10]. Moving away from the centerburst, more and more cosine components become out of phase, leading to a rapid decay of the modulation amplitude at the large OPD part of the interferogram. It turns out that, if the recorded interferogram does not cover the centerburst sufficiently, the resulted spectral peak will be broadened considerably. When one can only measure a fixed length of the interferogram, it matters which part of the interferogram is covered in the recording.

To illustrate this, we performed simulations considering a broadband signal that has a Gaussian distribution of spectral intensity, as shown in figure 3.23. The Gaussian signal is constructed with a set of Delta peaks, each corresponding to a cosine line shape in the Fourier domain.

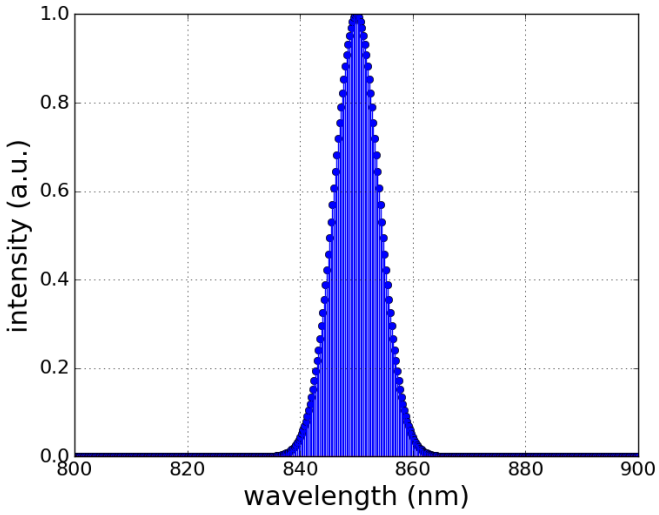

Figure 3.23: A set of delta peaks used in the simulation to mimic a Gaussian-like signal.

The interferogram is then the sum of these cosine components, as can be expressed by:

$$I(x) = \sum_{\lambda} [2I(\lambda) + 2I(\lambda)\cos(2\pi \frac{\Delta n_{eff}}{\lambda} x + \Delta\phi)] \tag{3.4}$$

where $I(x)$ is the interferogram as a function of propagation distance x, $I(\lambda)$ is the amplitude of a cosine component corresponding to the frequency component with wavelength of λ. A phase-shifting term, $\Delta\phi$, allows us to shift the interferogram along the x-axis. In the simulation, we take the different fragments of the interferogram, as shown in 3.24, and calculate the corresponding spectrum.

While having different length of coverage, the fragments a, b and c all cover the centerburst completely. Fragments d, e and f have the same length as fragment b, but only cover part of the centerburst. The spectra calculated from the different simulated interferograms are shown in figure 3.25.

It is easy to find that as long as the recorded interferogram covers the centerburst completely, there will be no peak broadening in the calculated spectrum, no matter how wide is the coverage of the interferogram. From the spectra calculated from fragment b, d, e, and f, we can see that, while having the same coverage length, the interferogram recorded at the different

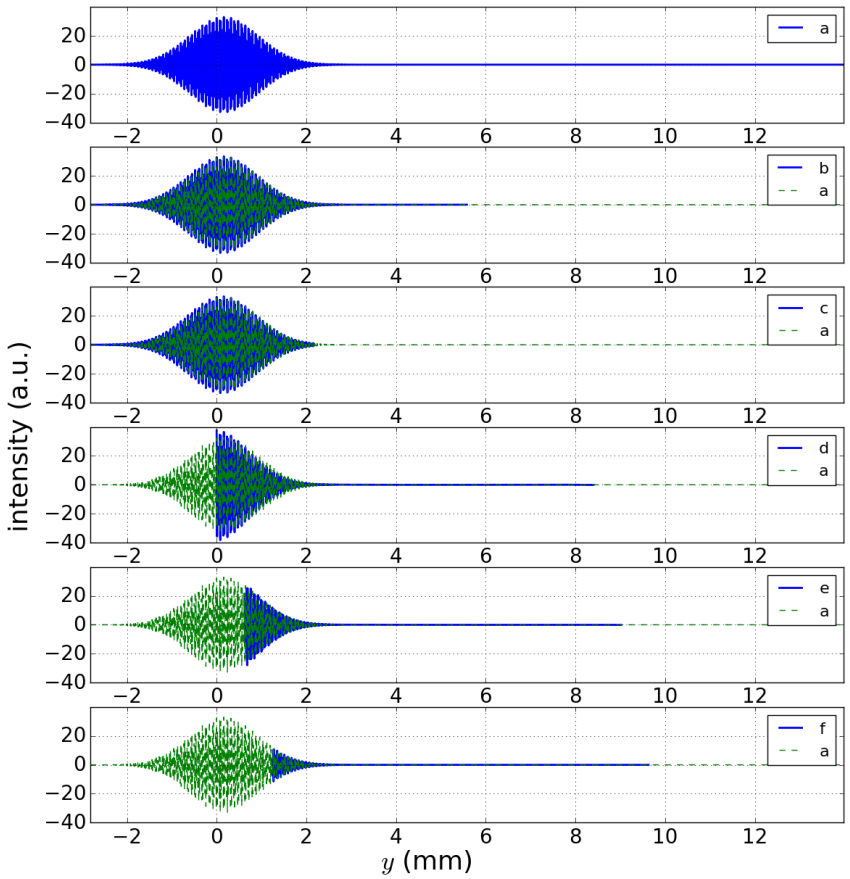

Figure 3.24: Different fragments of interferogram generated with the same Gaussian-like signal: while having different coverage lengths, a, b and c all cover the centerburst completely; b, d, e, f have the same coverage length while covering different parts of the centerburst.

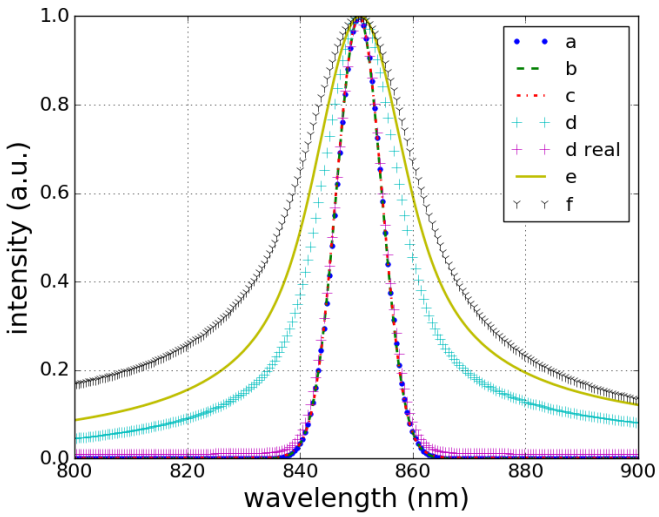

Figure 3.25: Calculated spectra with the different fragments shown in figure 3.24, all spectra are absolute spectra except for the real spectra indicated by $d\ real$. The peak in spectrum a, b and c has the same FWHM as the one shown in figure 3.23 and figure 3.22. In spectrum d, e and f, the peak is broadened to different extent as the corresponding interferograms only cover a small portion of the centerburst. The peak in the real spectrum $d\ real$ also shows no broadening.

location can lead to a different spectrum. As the coverage window moves away from the centerburst, the spectral peak gets more and more broadened.

Now, it is clear that in order to avoid broadening, one must be careful in choosing which part of the interferogram to be recorded. In principle, an ideal one-sided interferogram recorded on the positive OPD side (from 0 to L) can provide as much information as the double-sided one (from -L to L), because the interferogram is symmetrical about ZPD [6]. The fragment d is such a single-sided interferogram. We can see that the peak shown in the real spectrum $d\ real$ is not broadened.

According to Fourier transform theory [6], to obtain the real spectrum from the one-sided interferogram without introducing distortions, one should make sure that the ZPD points of all the cosine components are positioned at the origin. Any deviation will introduce phase errors leading to a distorted real spectrum. For a practical interferogram, there usually are phase errors due to imperfect instrument phase response. As a result, it is often beneficial to start the recording of the interferogram from the negative OPD side so that the recorded interferogram contains a small symmetric

part. Using the information contained in this part, one can perform phase correction [11, 12] and thus obtain a real spectrum with less distortion. For more details about the phase correction, one can read section 4.3 of [6].

3.5.2.2 Impaired SNR

Furthermore, we want to investigate why the spectra obtained with our on-chip FTS have such an impaired SNR. We introduce noise to the simulated interferogram and see how the spectrum changes. The noise is introduced by adding a random value to each point of the interferogram. The random value has a probability distribution combining Gaussian type and Poisson type to mimic the thermal noise and the shot noise. We add the noise to the interferogram fragment d, e and f and show them in figure 3.26.

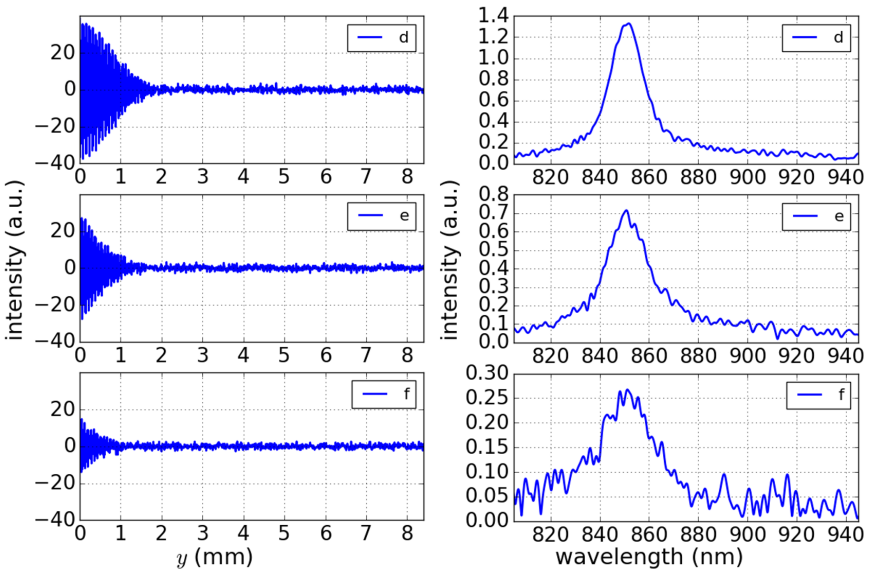

Figure 3.26: Interferogram fragments (d, e and f as shown in 3.24) with same noise level and the corresponding spectra calculated from them.

We can calculate the corresponding spectrum from these interferogram fragments. As shown in 3.26, the spectrum f now looks very similar to the interferogram we measured. While the noise levels are set to be the same for the interferogram d, e and f, the calculated spectra exhibit different SNR level. We can see from figure 3.26, as the coverage of the centerburst getting small, the SNR becomes worse. Such a trend is not difficult to understand. The useful information comes mainly from the centerburst, while

the noise is added to every data points of the interferogram. As the recording window moves further away from the centerburst, less signal could be obtained from the remaining centerburst, leading to reduced signal strength in the spectrum. On the other hand, the noise level stays almost the same. The overall outcome is a worse SNR.

3.5.2.3 Discussion

The simulation tells us that both the broadening of the spectral peak and the impaired SNR come from the fact that the recorded interferogram covers only a small part of the centerburst. This is actually the case for the current design of our on-chip FTS. OPD starts to increase immediately after the two waveguides begin to have different widths. This is the zero OPD point. However, in the design, the grating does not start from here. The light first needs to go through the tapers and then propagate in the two waveguides (with different widths) for a long distance to meet the grating. In this case, the starting point of the interferogram is on the positive OPD side and is away from the ZPD point. As a result, the spectral peak is considerably broadened and the SNR is poor.

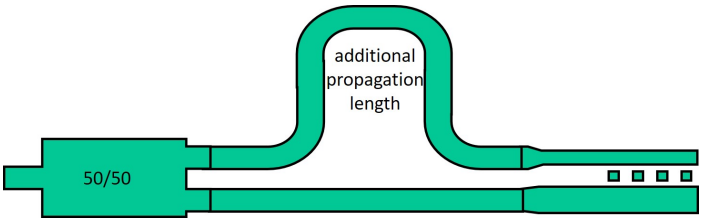

Figure 3.27: Sketches of introducing an initial frequency-dependent phase delay by adding an additional propagation length.

In the future designs, in order to reduce the broadening and improve the SNR, we should make sure that we can start the recording of the interferogram from a negative OPD point. As the OPD keeps increasing when the light propagates in the two waveguides (with different widths), we should set an initial phase delay that scales with wavelength to the light that goes into the narrow waveguide. As such, when the light starts to propagate in the two waveguides (with different widths), the OPD will start to increase from a negative value. We can, therefore, put the first grating unit at the point of a small negative OPD. In practice, the extra frequency-dependent phase delay can be introduced by adding an additional propagation length to the taper that goes to the narrow waveguide, as shown in figure 3.27.

3.6 Conclusion

In this chapter, we introduced the methods we used to characterize our on-chip integrated co-propagative stationary FTS and presented the experimental results measured from both types of on-chip FTS. Considering monochromatic input signals, we demonstrated that our on-chip FTS could provide a moderately high resolution (down to 2 nm) in a wide wavelength range (up to 200 nm). While there is no theoretical limitation of the operational bandwidth, we found that, in practice, the bandwidth is limited by the dispersive nature of the waveguide modes and the single-mode condition of the waveguides. Furthermore, we performed experiments with a broadband signal. We showed that the spectral peak could be reconstructed from the measured interferogram, though the spectrum is noisy and the peak is broadened noticeably. We investigated with simulations and realized that, in order to have a high SNR and reduce the broadening, the recorded interferogram should cover the centerburst as completely as possible.

In conclusion, we experimentally demonstrated that the proposed on-chip co-propagative stationary FTS works reasonably well and can be useful for on-chip applications requiring spectral measurement with a high resolution in a broad bandwidth. The experimental results not only demonstrated the performance of our on-chip FTS but also gave us insight on how to make improvements in future versions.

References

[1] Xiaomin Nie, Eva Ryckeboer, Günther Roelkens, and Roel Baets. *CMOS-compatible broadband co-propagative stationary Fourier transform spectrometer integrated on a silicon nitride photonics platform*. Optics express, 25(8):A409–A418, 2017.

[2] Pix4Life. *European Pilot line for supporting life science and biomedical applications on silicon nitride-based photonic integrated platforms*. `https://www.pix4life.eu/`. Accessed: 2019-09-09.

[3] Eugene Hecht. *Optics 2nd edition*. Optics 2nd edition by Eugene Hecht Reading, MA: Addison-Wesley Publishing Company, 1987, 1987.

[4] Bert Hecht, Beate Sick, Urs P Wild, Volker Deckert, Renato Zenobi, Olivier JF Martin, and Dieter W Pohl. *Scanning near-field optical microscopy with aperture probes: Fundamentals and applications*. The Journal of Chemical Physics, 112(18):7761–7774, 2000.

[5] *E712T0016, User Manual valid for Fast Multi-Channel Photonics Alignment*. Physike Instrumente GmbH & Co.

[6] Peter R Griffiths and James A De Haseth. *Fourier transform infrared spectrometry*, volume 171. John Wiley & Sons, 2007.

[7] Peter R Griffiths. *Photometric precision in infrared spectra measured by Fourier transform spectroscopy*. Applied Spectroscopy, 29(1):11–14, 1975.

[8] Eric W Hansen. *Fourier transforms: principles and applications*. John Wiley & Sons, 2014.

[9] CD Porter and DB Tanner. *Correction of phase errors in Fourier spectroscopy*. International Journal of Infrared and Millimeter Waves, 4(2):273–298, 1983.

[10] Brian C Smith. *Fundamentals of Fourier transform infrared spectroscopy*. CRC press, 2011.

[11] Lawrence Mertz. *Transformations in optics*. New York: Wiley, 1965, 1965.

[12] Lawrence Mertz. *Auxiliary computation for Fourier spectrometry*. Infrared Physics, 7(1):17–23, 1967.

4

On-chip Pump Rejection Filter

This chapter covers the working principles, the design details, and the experimental characterizations of an on-chip pump rejection filter implemented on a silicon nitride rib waveguide platform. This filter has an unlimited free spectral range on the long-wavelength side of the stop/pass-band and could provide an ultra-high extinction ratio. Therefore, it is of particular interest for the implementation of on-chip spectroscopic systems where the pump light needs to be rejected for the better detection of the weak spectroscopic signals. As an example, this can be an on-chip Raman spectrometer. Most of the content of this chapter is based on [1, 2].

Contents

4.1 Introduction

On-chip wavelength filters, as the essential components for various optical devices, are attractive to researchers in the fields of on-chip lasers, optical sensors [3] and wavelength-division multiplexers [4]. Filters based on Bragg reflectors, micro ring resonators (MRRs) and cascaded Mach-Zehnder interferometers (MZIs) have been studied and demonstrated to meet the requirements of various applications [3–5].

4.1.1 Filters with limited FSR

Usually, filters based on the MRRs or cascaded MZIs have a limited and often small free spectral range (FSR), which means the spectral spacing between two consecutive pass/stop bands is small (in the range of a few or a few tens of nanometers). To give some examples, figure 4.1 shows the transmission spectrum of a ring resonator and a five-stage cascaded Mach-Zehnder filter. More information on the design and principle of the ring resonators and cascaded MZIs can be found in [6, 7].

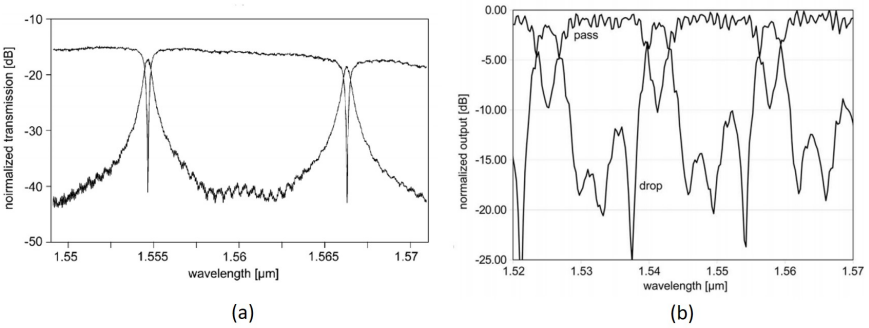

Figure 4.1: The transmission spectra of drop and pass ports for (a) a racetrack ring resonator with 5 μm bend radius and 6.28 μm coupling section; (b) a five-stage cascaded Mach-Zehnder filter. Reprinted from [7].

The limited FSR makes MMRs or cascaded MZIs based filters not suitable for applications such as the on-chip Raman spectroscopic systems [8], which requires a flat spectral response in the wavelength range where the Raman Stokes signals are generated. Quite some efforts have been made to realize a large FSR in these types of filters. An intuitive way is to reduced the bend radius of the ring as in the case of [9], where a bend radius of 2 μm leads to the FSR as high as 47 nm. Utilizing the Vernier effect presented

in multiple ring resonators with slightly different FSRs is another way to increase FSR [10, 11]. One can also obtain large FSR by introducing intentional reflections inside the ring resonator which suppresses or cancels the side modes [12–14]. Nevertheless, these approaches are not easy to implement as they require high fabrication accuracy, careful designs and sometimes complicated controls.

4.1.2 Grating-based filters

One the other hand, grating-based filters inherently have a large or unlimited FSR aside its pass/stop band [15].

4.1.2.1 Bragg reflector

As a type of grating-based filter, the Bragg reflectors have been widely used in the field of fiber communications for the purpose of in-line wavelength selection and dispersion compensation [16–18]. In a single mode waveguide-based Bragg reflector, the stopband in the transmission spectrum appears at the wavelength given by

$$\lambda = \frac{2}{m} n_{eff} \Lambda, \tag{4.1}$$

where n_{eff} is the effective refractive index of the waveguide mode, Λ is the period of the grating and m is an integral number describing the order of the grating. As a typical Bragg reflector normally uses a first order grating, there is no spectral feature in the transmission spectrum at the long wavelength side of the stopband. This is advantageous and makes the grating-based filters particularly attractive for the applications that require a flat spectral response in a large bandwidth aside the stopband.

However, a Bragg reflector has its own drawback. As a two-port device, the Bragg reflector reflects the light back into the input. This can be harmful to the on-chip light source such as an integrated laser. To use a Bragg reflector as an on-chip pump rejection filter, one would also need to integrate an on-chip circulator, which adds extra complexity and cost to the system.

4.1.2.2 Grating assisted contra-directional coupler

To solve this problem, one can employ a filter based on the grating assisted contra-directional coupler (GACDC). As demonstrated in [19–21],

a GACDC has a Bragg-grating-defined transfer function and therefore enjoy the same advantage of having an unlimited FSR (on one side of the stopband). Moreover, a GACDC filter is different from the Bragg reflector in that it can couple the rejected light contra-directionally into a bus waveguide, instead of reflecting it back to the input. This property allows a GACDC filter to be integrated directly after an on-chip light source without the need for a circulator.

4.1.3 Filters with very high extinction ratio

Another critical characteristic of an on-chip filter is the extinction ratio. As mentioned, a pump rejection filter needs to have an extremely high extinction to suppress the strong pump and, therefore, helps to reveal the weak signal to the spectrometer. It has been reported that an ultra-high rejection ratio can be achieved by cascaded filters based on ring resonators or MZIs with active phase-tuning between the stages [22–24]. Again, these filters typically have a small FSR, precluding their usage as pump-rejection filters in applications that require a broad passband.

Theoretically, a filter based on the Bragg-grating can have an arbitrarily high extinction ratio with a sufficient grating length. However, most of the practical implementations have a maximum achievable extinction around 40 dB, limited by the fabrication imperfections [5, 25, 26]. In this chapter, we will also study this saturation phenomenon and take a close look at the possible underlying mechanism. With the understanding of mechanism that leads to the saturation, we demonstrate a novel design of cascaded GACDC filters and show that it can surpass the limitation set by the fabrication errors.

4.1.4 GACDC filters implemented on SiN platform

As the main subject of this chapter, GACDCs were first implemented in planar optical waveguides based on silica and III-V materials [19]. After that, researchers have developed GACDCs on a silicon-on-insulator (SOI) platform at telecommunication wavelengths [21]. However, little effort has been spent to implement GACDCs operating at shorter wavelengths on the silicon nitride platform where optical bio-sensing applications such as on-chip Raman spectroscopy are growing and developing. The GACDC filters demonstrated in this chapter are implemented for TE-like modes on a silicon nitride rib waveguide platform. To allow device operation in the NIR

region (such as at the often used pump wavelength of 785 nm in on-chip Raman applications), we need to design the gratings with a period smaller than what can be achieved by conventional deep-UV lithography [27]. As a result, an e-beam lithography is used to realize the current prototype device. In the future, however, the proposed device can also be realized by deep-UV immersion lithography in a CMOS fab [28].

4.2 Working principles and design details

As shown in figure 4.2, a GACDC consists of a narrow and a wide rib waveguide (waveguide a and b) and a grating between them.

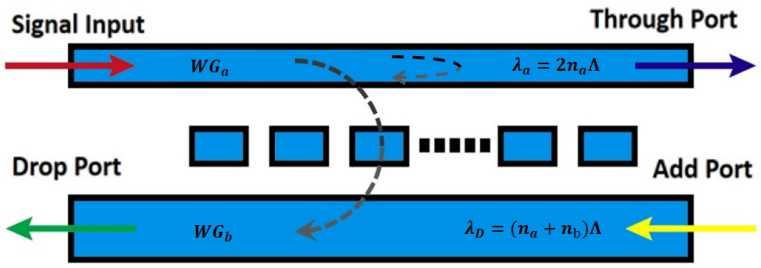

Figure 4.2: Schematic top view of the proposed grating assisted contra-directional coupler.

In such a waveguides system, the co-directional coupling between the fundamental TE-like modes in waveguide a and b is suppressed due to the large phase mismatch as the two modes have different propagating constants determined by their wavelength-dependent effective refractive indices (n_a and n_b). However, with the assistance of the grating, the contra-directional coupling can be achieved between the forward propagating modes and the backward propagating modes. Depending on the wavelength of the injected light, different types of coupling can occur when the corresponding phase-matching condition is fulfilled.

As shown in the k-diagrams in figure 4.3, the intra-waveguide Bragg reflection can happen to couple the forward mode into the backward mode in waveguide a for the light with wavelength λ_a determined by the phase matching condition:

$$k_a(\lambda_a) - \frac{2\pi}{\Lambda} = -k_a(\lambda_a), \tag{4.2}$$

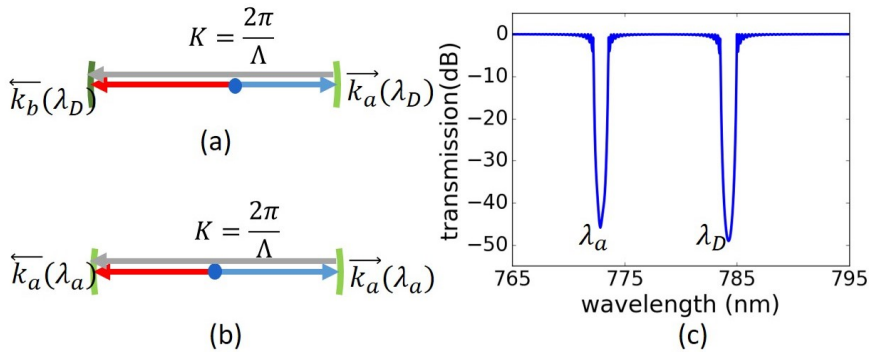

Figure 4.3: K-diagrams for the phase matching condition: (a) the forward-propagating mode in waveguide a is phase matched to the backward-propagating mode in waveguide b; (b) in waveguide a, the forward-propagating mode is phase matched to the backward-propagating mode.(c) An illustrative drawing of the transmission spectrum measured at the through port assuming broadband light in input into the narrow waveguide.

where Λ is the period of the grating and the propagation constant $k_a(\lambda_a)$ is calculated as $2\pi n_a/\lambda_a$. This leads to the expression of λ_a as $2n_a\Lambda$.

Moreover, at the wavelength of λ_D, the inter-waveguide contra-directional coupling can happen to couple the forward-propagating mode in waveguide a into the backward-propagating mode in waveguide b when the following phase-matching condition is fulfilled with the assistance of the grating [29].

$$k_a(\lambda_D) - \frac{2\pi}{\Lambda} = -k_b(\lambda_D), \tag{4.3}$$

where $k_a(\lambda_D)$, $k_b(\lambda_D)$ are the propagation constants of the guided modes in the two waveguides at wavelength λ_D. Again, we can calculate the inter-waveguide contra-directional coupling wavelength λ_D as $(n_a + n_b)\Lambda$.

Assuming broadband light is injected into the narrow waveguide of the GACDC, the transmission spectrum measured at the through port will have two stopbands corresponding to the intra-waveguide Bragg reflection and the inter-waveguide reflection induced by the contra-directional coupling, as illustrated in figure 4.3 (c). To make it convenient for the discussion, we refer to the two stopbands as the self-reflection band and cross-reflection band, respectively. It is worth to mention that, in applications such as on-chip Raman spectroscopy, the latter is used to reject the pump since there is an unlimited FSR on its red side and the former (as a side-effect of the design) is not used, given that light is injected into the narrow waveguide.

4.2.1 Design concerns

The proposed GACDC filters are sketched in figure 4.4. In a single-stage version as shown in 4.4 (a), we use grating couplers as I/O ports, and design waveguide tapers to connect them to the GACDC. As a 4-port device, the single-stage GACDC filter can be effectively cascaded by simply connecting multiple stages. In figure 4.4 (b), we show as an example the 4-stage cascaded GACDC filter. As will become clear later, the effective cascading allows the multistage GACDC filter to have an ultra-high extinction ratio.

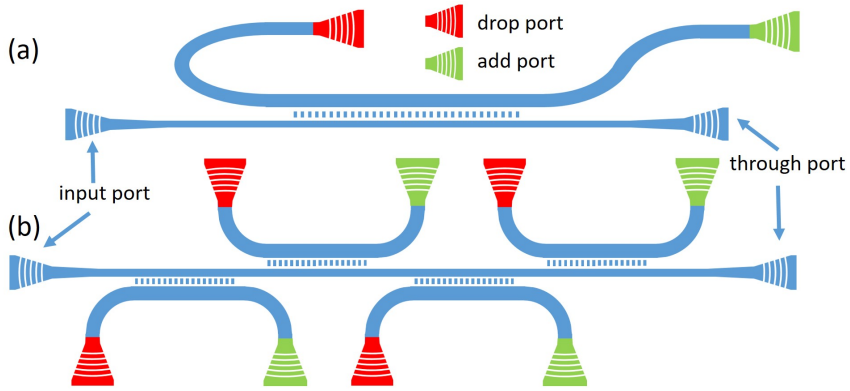

Figure 4.4: Sketches of (a) a single-stage CDC filter and (b) a 4-stage cascaded CDC filter.

In the design of a GACDC filter, we start with solving the waveguide modes in the coupler region with mode solver FIMMWAVE [30]. Through sweeping waveguide width, we can have an idea about how the effective refractive indices of the fundamental TE mode and first high order mode change with waveguide width. Then we can pick two waveguide widths that suppress co-directional coupling. After choosing two waveguide widths, we can calculate the required grating period for a desired center wavelength of the cross-reflection band. According to our simulation, a good example is to consider waveguide widths of 340 mn and 600 nm. In figure 4.5, we show the cross-section with the calculated intensity profiles of the fundamental TE-like modes in both rib waveguides. In the simulation, we set both of the rib height and slab thickness to 150 nm and choose 1.89 as the material refractive index of SiN, according to [31].

The reason of choosing the rib waveguide platform lies in the fact that the

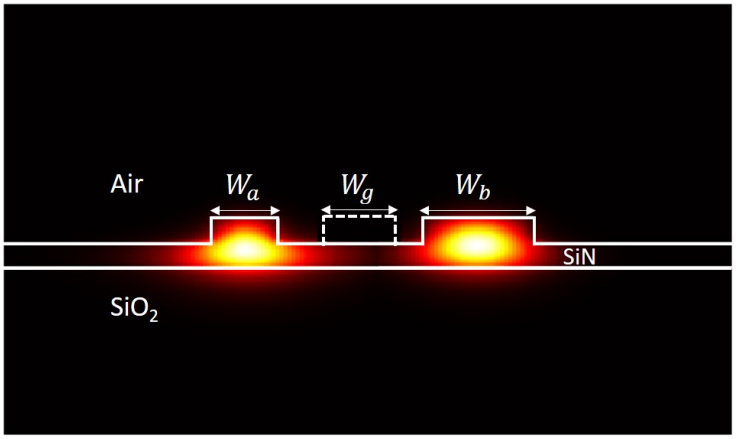

Figure 4.5: Cross-section of the coupler region with the intensity profiles of the fundamental TE-like modes of both rib waveguides.

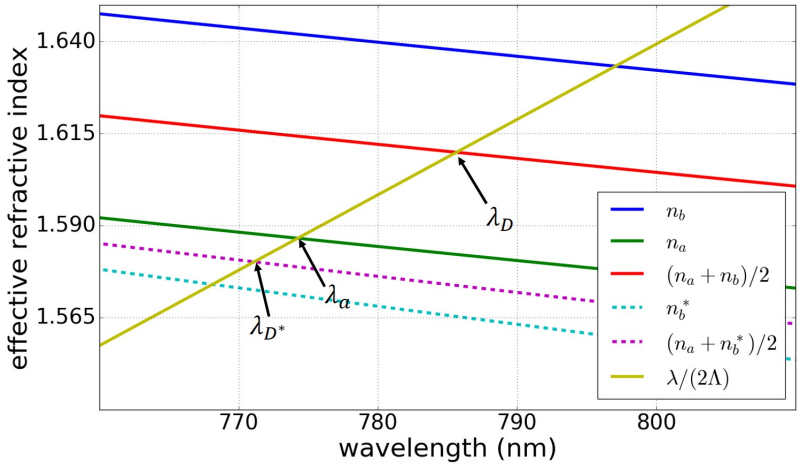

Figure 4.6: Dispersion curves of the modes with phase-matching wavelengths indicated with arrows and labels.

loosely confined modes in the rib waveguides allow a stronger coupling strength so that one can avoid placing the two waveguides too close to each other, which might be problematic in fabrication.

In figure 4.6, the effective indices of the modes in both waveguides are plotted as a function of the wavelength. The waveguide widths are determined to ensure a large phase mismatch between the fundamental TE-like mode in waveguide a and the guided modes in waveguide b to suppress the co-directional coupling. After that, we add the curves of the average indices and $y = \lambda/(2\Lambda)$ to calculate the grating period that allows matching λ_D to the required reflecting wavelength. In this work, we set λ_D to 785 nm and λ_a to 774 nm.

Other design concerns are the position and the width of the grating which play a role in determining the coupling strength. The coupling strength can be estimated by calculating the coupling coefficient κ_D and κ_a according to the coupled mode theory [29]:

$$\begin{aligned} \kappa_a &= \frac{\pi}{\lambda n_a} \iint e_a^*(x,y)\Delta\epsilon_1(x,y)e_a(x,y)dxdy \\ \kappa_D &= \frac{\pi}{\lambda n_a} \iint e_a^*(x,y)\Delta\epsilon_1(x,y)e_b(x,y)dxdy \end{aligned} \tag{4.4}$$

where $\Delta\epsilon_1(x,y)$ is the 1^{st} coefficient of the Fourier series expansion of the perturbation of the relative permittivity introduced by the grating, which only has a non-zero value in the grating region. And $e_{a,b}(x,y)$ is the electric field distribution of the fundamental TE-like mode in waveguide a or b, normalized with

$$\iint e_n^*(x,y)e_m(x,y)dxdy = \delta_{n,m} \tag{4.5}$$

where $m, n \in [a, b]$. From simulations, we can obtain the field distribution and then estimate the coupling strength.

4.2.2 Extinction ratio and the saturation

With the coupling strength κ, we can, in principle, calculate the achievable extinction ratio. According to mode coupling theory [29], for a grating-based reflector with a total grating length L, the peak reflection at the center wavelength of the stopband can be written as

$$R = \tanh^2(\kappa L). \tag{4.6}$$

According to equation 4.6, theoretically, an arbitrarily high extinction ratio can be obtained by increasing the total length of the grating. Realistically, however, the extinction ratio typically saturates around 40 dB beyond a certain filter length [5, 25, 26]. While it has been reported that the extinction ratio can be reduced by the light propagating in the cladding or substrate as well as the light with a different polarization [22, 24], we believe (as the experiments indicated) the primary mechanism limiting the extinction ratio is the forward scattering caused by the phase errors induced from fabrication imperfections.

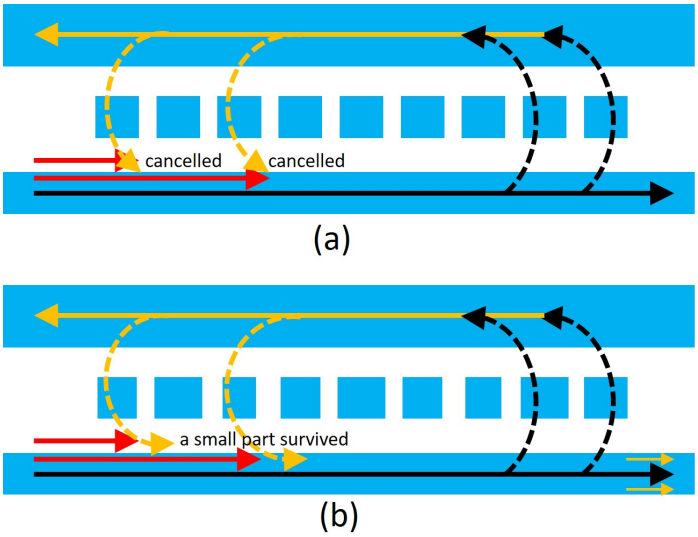

Figure 4.7: A sketch to illustrate the influence of the small phase errors introduced by imperfect fabrication. In (a), the multi-order reflections are cancelled out as they are completely out of phase to the light undergoing no scattering. In (b), a small part of multi-order reflections can survive in the presence of small phase errors, leading to the saturation of the extinction ratio when gratings become sufficiently long.

To understand this, we first think of a Bragg reflector without any fabrication imperfection. As shown in figure 4.7 (a), in this ideal reflector, the injected light propagating in the forward direction is continuously reflected by the grating units into the backward-propagating mode. At the Bragg wavelength, the periodicity of the grating units ensures that all partial reflections are in phase and interfere constructively. Although the reflected light propagating in the backward direction needs to travel through the grating and is therefore subject to secondary grating diffraction, the resulting

contributions to the forward-propagating light will actually be out of phase with the original light coming from the input, thereby helping the input light to decay exponentially. However, in real life, even a tiny fabrication imperfection can cause a phase error and create deviations in the phase relationships of all contributing field components. Such a phase error will, therefore, scatter the reflected light and allow a tiny amount of light to travel towards the through port. And, as the length of the grating increases, more and more contributions (with phase errors) will play a role and accumulate to set a certain saturation level, limiting the achievable extinction ratio. This is the case shown in figure 4.7 (b).

To surpass this limitation and achieve higher extinction ratio, an effective way is to remove the reflected light before it can propagate through many grating units [32]. We can easily implement this strategy with the cascaded GACDC filters.

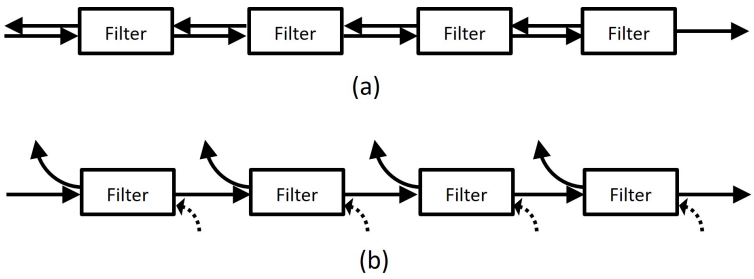

Figure 4.8: A sketch to illustrate the difference between (a) the inefficient cascading, where the filter in each stage is a 2-port device such as the simple Bragg reflector and (b) the efficient cascading, where the filter in each stage is a 4-port device as in the case of a GACDC.

As shown in figure 4.8 (a), a simple Bragg reflector can not be efficiently cascaded. As a 2-port device, the reflected light in one stage will have to go through the grating units in the previous stages. In fact, cascaded Bragg reflector can not be differentiated from a long Bragg reflector, given no phase shifting is introduced at the connecting sections.

On the contrary, as a 4-port device, the GACDC filter offers the opportunity for efficient cascading in this sense. As shown in figure 4.8 (b), in a cascaded GACDC filter, the light coupled contra-directionally to the bus waveguides can be coupled out through the drop-ports. As such, they will not propagate to the grating units in previous stages. Consequently, fewer contributions to the forward-propagating light can be expected, and therefore a higher extinction ratio can be measured at the through port.

4.3 E-beam prototyping

As mentioned previously, we prototype the proposed GACDC filters with E-beam lithography. The fabrication is done by our colleagues Nina Turk and Yang Li using the cleanroom facilities at Ghent University.

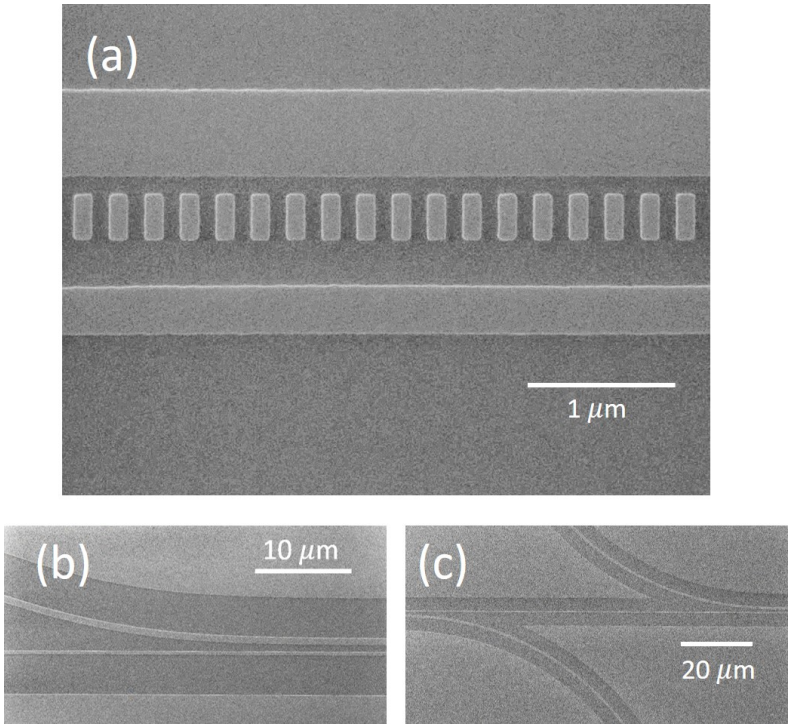

Figure 4.9: SEM pictures of (a) the coupler region which contains two waveguides and a grating in between, (b) the mode-transition region where waveguide b is approaching waveguide a, and (c) the mode-transition region in the cascaded GACDC filter.

In figure 4.9, we show the fabricated devices in the scanning electron microscopy (SEM) images. Measured from the SEM pictures, the fabricated devices have a width of waveguide a, w_a = 330 nm, a width of waveguide b, w_b = 585 nm. The grating has a width w_g = 320 nm, a period Λ = 244 nm and a duty cycle around 50%. To obtain a proper coupling strength κ (which can be calculated by equation 4.4), we set the spacing between the two waveguides to 750 nm and laterally shift the grating for 80 nm from the center to waveguide b. In the mode-transition regions on the two sides of each coupler, we designed bending tapers to bring the two

waveguides close and to separate them as shown in Figure 4.9 (b) where waveguide b is approaching waveguide a, and in figure 4.9 (c) which pictures the mode-transition regions of the cascaded GACDC filter.

4.4 Measurement results

In the experiments, we use a vertical coupling setup to characterize the fabricated devices.

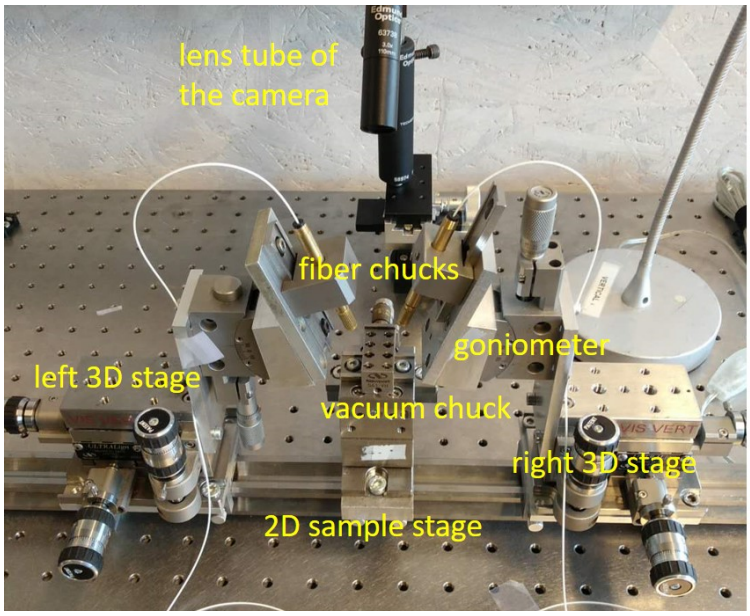

Figure 4.10: A photography picture of the vertical coupling setup used in the characterization of the on-chip GACDC filters.

As shown in figure 4.10, the vertical coupling setup contains two cleaved single mode fibers (780HP) installed on two 3-D translation stages through the fiber chucks and the goniometers. In the regular operation, the fibers are held near-vertically as the standard on-chip grating coupler typically works with a 10-degree diffraction angle with respect to the normal of the chip to avoid back reflection. In between of the two 3-D fiber stages, there is a 2-D sample stage which holds the chip by a vacuum chuck. One of the fibers is used as the input fiber and is connected to a laser through a polarization rotator (PR), which can be used to rotate the polarization and to optimize the transmission as the standard grating couplers are designed for

a specific polarization. Light is coupled into and out of the chip through the on-chip grating couplers. The alignment between the fiber and the grating coupler on the photonic chip is done under the oblique view provided by a CMOS camera. To obtain the transmission spectra with a sub-nanometer resolution (0.3 nm) in the wavelength range that is interesting to us, we use an ultra-narrow linewidth Continuous Wave (CW) Ti: Sapphire laser (M2lasers, tuning range 710-975 nm) as the light source. After propagating through the on-chip device, the transmitted light is coupled out of the waveguide through the other fiber and is sent to a power meter (HP 8153A) for quantitative measurement.

4.4.1 Filters with single stage GACDC

To study the dependence of the extinction ratio to the total grating length L, we first measured the transmission spectra for the single-stage GACDC filters with various filter lengths, $L = 150$, 300, 600, 1000, 2000 and 3000 μm. We plot the transmitted power as a function of wavelength in figure 4.11 (a).

It can be observed that the two notches centered around 772.0 and 783.6 nm correspond to the self-reflection and cross-reflection band. A third dip centered at 769.2 nm could be explained by the contra-directional coupling between the forward-propagating mode (with effective refractive index n_a) in waveguide a and a high order TM-like backward-propagating mode (with effective refractive index n_b^*) in waveguide b. These three wavelengths are in agreement with λ_a, λ_D and λ_{D^*} in figure 4.6, with the small discrepancy induced by the uncertainties in the etch depth. Given the input power of around 3 dBm, the average insertion loss is estimated to be 18.8 dB resulting from the loss of fiber-to-chip coupling as the grating couplers are not optimized.

It is noteworthy that in these experiments, as tuning the Ti: Sapphire laser is quite-time consuming (a few seconds per point), we only measured the spectra in the wavelength range from 768 nm to 787 nm, where we can see most of the interesting spectral contents. In an earlier experiment, we characterized another sample (and with a different design) with a broadband supercontinuum source and an optical spectrum analyzer (OSA). The transmission spectrum is shown in figure 4.12. In the spectrum, three drops can be observed as expected. While there is a flat spectral response on the long-wavelength side of the cross-reflection stop, one can also observe the drops of transmission in the wavelength range below 770 nm. These drops come from the fact that in this wavelength range, the gratings start to couple

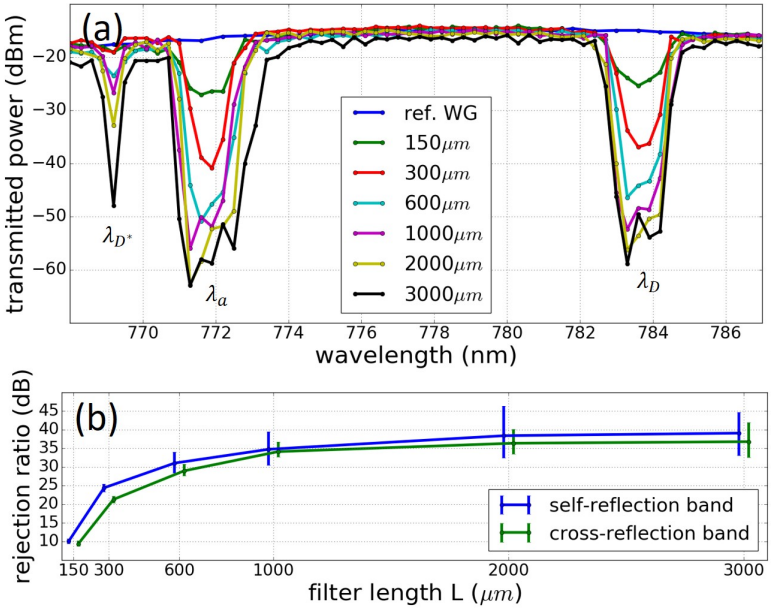

Figure 4.11: (a) Measured transmission spectra of a reference rib waveguide and GACDC filters with $L = 150$, 300, 600, 1000, 2000, and 3000 μm; (b) the calculated average extinction ratio in both stop bands plotted as a function of the filter length L. In (b), the two curves are shifted horizontally ± 20 μm for better visualization.

the light into the radiation modes in the buried oxide cladding.

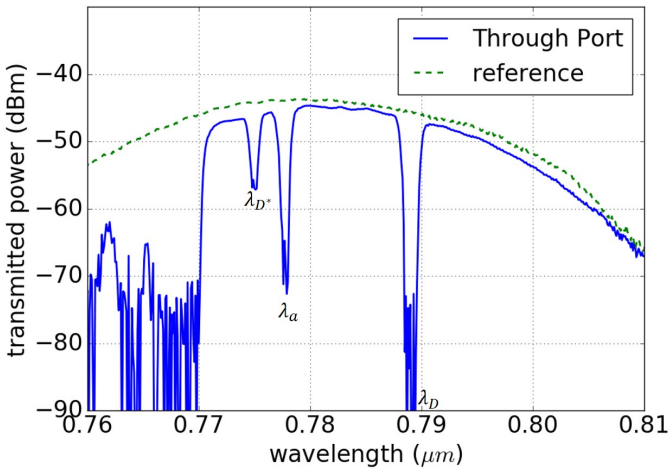

Figure 4.12: Transmission spectra measured at the through port of a GACDC device with a supercontinuum source and an optical spectrum analyzer in a wide wavelength range.

4.4.2 Saturation of the rejection ratio

In order to better reveal the trend of the saturation, we need to estimate the average extinction ratio as the spectral response inside the stop bands is not smooth, especially for the devices with a large filter length. This is done by averaging the transmitted power measured around the center wavelengths of the stopbands and normalize it to the averaged transmitted power measured outside the stop bands. The calculated average extinction ratio is presented in figure 4.11 (b) for both the self-reflection and cross-reflection stop bands as a function of the filter length L. The error bars show the maximum and minimum extinction ratio inside the stopbands. From the curves, we can see the trend of saturation. While the average extinction ratio of the cross-reflection band is lower than that of the self-reflection band, they both increase with the total grating length L. As expected, the increment decreases for large filter length, and the extinction ratio almost stops increasing and saturates to around 40 dB for L larger than 2000 μm.

4.4.3 Filters with cascaded GACDC

In the experiments with the cascaded GACDC filters, we consider a set of cascaded GACDC filters that have the same total filter length ($L = 2000\ \mu$m) but with a different number of stages (4, 8, 10 and 16). With these devices, we want to show that the cascaded GACDC filters have a higher extinction ratio in comparison to the single-stage version.

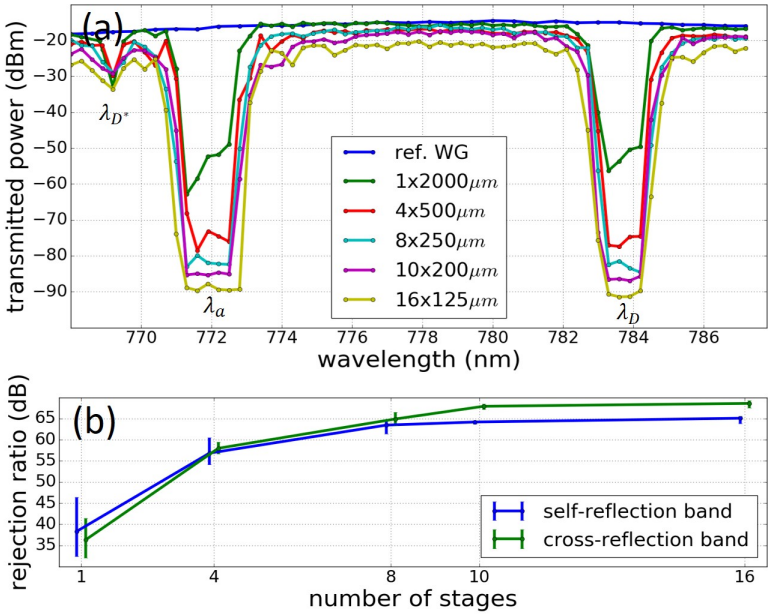

Figure 4.13: (a) Measured transmission spectra of a reference rib waveguide, a single-stage GACDC filter with $L = 2000\ \mu$m, and cascade GACDC filters with the same total length, but a different number of stages (4, 8, 10, and 16); (b) the calculated average extinction ratio in both stop bands plotted as a function of the number of stages. In (b), the two curves are shifted horizontally ± 0.1 for better visualization.

Again, we measured the transmission spectra and show them in figure 4.13 (a) with the reference spectrum obtained with a rib waveguide. To better compare with the single-stage version, we also include in the figure a spectrum measured from a single-stage GACDC filter with $L = 2000\ \mu$m. Likewise, we plot the average extinction ratio in figure 4.13 (b) as a function of the number of stages.

In the cross-reflection band, we can see that the cascaded GACDC filters provide a considerably higher extinction ratio when compared to the single-

stage version. The increased extinction ratio comes from the effective cascading. While the phase errors introduced by the fabrication imperfections are still there, most of the reflections are coupled out from the drop-ports before they can interact with the grating units in the previous stages. As the number of stages increases, the reflections are removed more frequently and thoroughly, allowing the filter to suffer less from the phase errors and therefore have a higher extinction ratio. The spectra shown in 4.13 (a) and the trend plotted in 4.13 (b) agree with our expectations. From a 16-stage cascaded GACDC filter, we measured the highest average extinction ratio of up to 68.5 dB in the cross-reflection band with a bandwidth less than 3 nm. This is an improvement of $\sim$30 dB when compared to what is achieved by the single-stage GACDC filter with the same filter length.

4.5 Discussion

While we have demonstrated that the cascaded GACDC filter can achieve an extinction ratio much higher than the single-stage version, there are still some details that need to be further discussed.

4.5.1 New limitations

Firstly, we noticed that there is a new saturation level for the achievable extinction ratio. In the experiments, we tried to decrease the input power and observed the decreasing of the transmitted power for the same amount in the stop bands. This tells us the new saturation level can not be attributed to the noise floor of the power meter. The major cause of the new saturation level, we suspect, is the remaining light that is not removed from the drop ports. While most of the reflections are coupled out from the drop port grating couplers, still a small portion can survive and be coupled back into waveguide a. This small portion of reflections, propagating in waveguide a, is subject to the secondary grating diffraction, and therefore make a contribution to the forward-propagating light that can reach the through port. Likewise, the light reflected by the grating coupler can also propagate back into the mainstream waveguide after one or multiple times of coupling, and in the end, contribute to the saturation. In order to achieve even higher extinction ratio, the reflected light should be coupled out more thoroughly. This can be done by utilizing transition taper that is optimized to suppress the co-directional coupling further. For the same purpose, one can replace the standard grating couplers at the drop ports to the lower reflection ones

as proposed in [33].

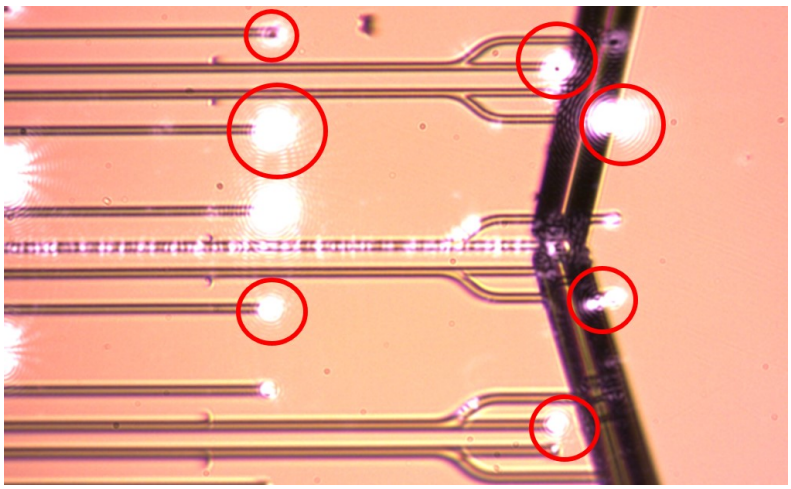

Figure 4.14: A picture of the photonic chip taken at the output side during the measurement. While the light is coupled into the middle shining device, the other output grating couplers of the neighboring devices (marked in the red circles) are also lit up, indicating the leaking of the input light in the SiN slab.

Moreover, the light leaked into the 150 nm thick SiN slab could cause problems when we want to pursue a higher extinction ratio. The leakage has been observed in the experiments when the grating couplers of the neighboring devices are lit up by the light that is launched solely into one input grating coupler as shown in figure 4.14. The light leaked into the slab can travel around in the photonic chip and be scattered by the neighboring devices or be reflected by the edge of the chip, setting stray light. Although this is not the limitation for the moment, we will face it when we want to approach even higher extinction ratio. A potential solution for this could be to surround the individual device with on-chip absorbing structures or materials.

4.5.2 Position of the cross-reflection stop band

Secondly, as we can see from the spectra in figure 4.11 and 4.13, the position of the cross-reflection stopband is not exactly as we designed. The displacements are observed from multiple test runs and can be attributed to the fabrication unpredictability including the uncertainty of height of the SiN layer, the deviation of the etch depth and the variation of the waveguide width. The dependence of the displacement to these geometry changes

has been investigated together with the master student Zuyang Liu in her master program. The dependencies are summarized in table 4.1.

$\delta\lambda_D/\delta$height	0.63
$\delta\lambda_D/\delta$etch	0.30
$\delta\lambda_D/\delta$width	0.08

Table 4.1: Ratio between the displacement of the spectral position of the cross-reflection stop band $\delta\lambda_D$ and the change in the SiN layer height around the nominal value 300 nm, in the etch depth around the nominal value 150 nm and in the width of the waveguide around the designed value.

From the table, we can see that the most important influence comes from the variation in the thickness of the SiN layer. For example, a deviation of 10 nm from the nominal value can already lead to about 6 nm displacement of the position of the cross-reflection stopband. The uncertainly in the etch depth also plays a role, while the influence brought by the changes of the waveguide width is of the least importance. Such dependencies tell us, to have the band position at the desired wavelength, the fabrication variations should be taken into account. Ideally, one can carefully measure the full thickness of the SiN layer and accurately control the etch depth. In practice, one can also do a test run and use the feedback to make compensations in the design for the next run. Another solution is to introduce tuning mechanisms to tune the stop band to the desired wavelength actively.

4.5.3 Improved extinction ratio in the self-reflection band

Another interesting phenomenon observed in the measured spectra is that the extinction ratio of the self-reflection band is also increased. While the extinction ratio of the cross-reflection band is lower than that of the self-reflection band in the case of a single-stage GACDC filter, the situation is reversed in the cascaded GACDC filter. This means the extinction ratio in the self-reflection band does not improve as much as in the cross-reflection band. Two possible mechanisms can explain this improvement.

The first mechanism is related to the co-directional coupling that happens in the mode-transition regions, where waveguide b is approaching to or moving away from waveguide a. From the simulation, we found that although the large phase mismatch suppresses the co-directional coupling, there is still some coupling between the two forward-propagating modes. As shown in figure 4.15, we simulated the field distribution when light propagates through the taper and calculated the coupling coefficients with

FIMMPROP [34]. When light propagates from the left hand side (LHS) to the right hand side (RHS), 96.68% of the power stays in waveguide a, while the rest is co-directionally coupled into waveguide b.

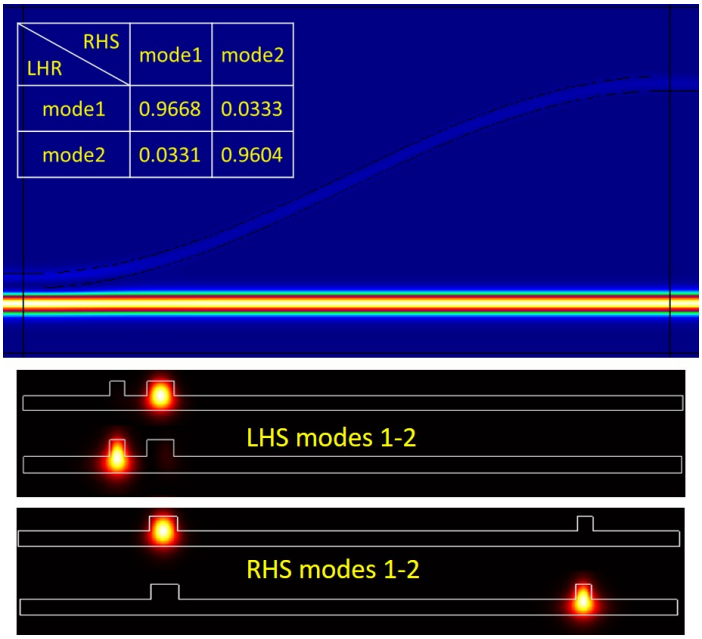

Figure 4.15: Simulated field distribution in the taper region, with the calculated coupling coefficients shown in the inset table. The modes concerned are shown in the cross-section on the two sides.

This equals to a loss of -0.15 dB per taper. Such a small loss is negligible for the single-stage GACDC filter as it only has two tapers. However, for a cascaded GACDC filter with many stages, the total loss experienced by the light propagating directly from the input port to the through port becomes non-negligible. For instance, in the 16-stage cascaded GACDC filter, light traveling through all 32 tapers will experience a total loss of around -4.8 dB. This is the major contribution to the passband loss of around -5.6 dB estimated from the measured spectra in 4.13 (a). For light with wavelengths inside the self-reflection band, the situation is even worse. As an example, in the worst case, light reflected at almost the end of the grating will propagate backward in waveguide a to almost the beginning of the grating where it is partly reflected due to a phase error there, reversing its direction and propagating towards the through port. This light, while making it to the through port, has to travel through most of the tapers multiple times and therefore is significantly attenuated. More generally, inside the self-

reflection band, most of light has to travel through tapers multiple times if they want to reach the through port and contribute to the saturation. Consequently, for the cascaded GACDC filters with many stages, the extinction ratio inside the self-reflection band is increased.

The second mechanism plays a role in the coupler regions, where the two waveguides are parallel. As waveguide a has a small width W_a = 330 nm and is placed only 750 nm away from waveguide b, the fundamental TE-like mode in waveguide a is loosely confined and slightly pulled to waveguide b. This means that even though the intra-waveguide reflection happens mostly in waveguide a, a small amount of light can also be scattered into waveguide b and can propagate in the backward direction. With this part of light coupled out from the drop ports, we removed the possibility that they could be scattered back again into waveguide a and propagate to the through port. To some extent, this also helps to increase the extinction ratio inside the self-reflection band.

4.6 Conclusion

To summarize, we have introduced the on-chip GACDC filters with the cross-reflection band in the NIR range. The filters are fabricated on a silicon nitride rib waveguide platform. Experimentally, we observed that the average extinction ratio saturates to less than 40 dB for single stage GACDC filters with the filter length beyond 2000 μm. We also demonstrated that cascading of the GACDCs helps to obtain an extinction ratio beyond this saturation level. The result measured from a 16-stage cascaded GACDC filter shows a stop band centered at the inter-waveguide contra-directional coupling wavelength λ_D = 783.6 nm with a bandwidth of less than 3 nm and an average extinction ratio up to 68.5 dB. In conclusion, by coupling the rejected light into the bus waveguides, the proposed cascaded GACDC filters can provide a stop-band with a very high extinction ratio and an unlimited FSR on the red side of it. These properties make the on-chip GACDC filters suitable and promising for pump rejection in applications such as on-chip Raman spectroscopy.

References

[1] Xiaomin Nie, Nina Turk, Yang Li, Zuyang Liu, and Roel Baets. *High extinction ratio on-chip pump-rejection filter based on cascaded grating-assisted contra-directional couplers in silicon nitride rib waveguides*. Optics letters, 44(9):2310–2313, 2019.

[2] Xiaomin Nie, Nina Turk, Zuyang Liu, and Roel Baets. *Grating assisted contra-directional filters with high rejection ratio in silicon nitride rib waveguides*. 21th European Conference on Integrated Optics (ECIO 2019), page p.T.Po2.11, 2019.

[3] Katrien De Vos, Irene Bartolozzi, Etienne Schacht, Peter Bienstman, and Roel Baets. *Silicon-on-Insulator microring resonator for sensitive and label-free biosensing*. Optics express, 15(12):7610–7615, 2007.

[4] Folkert Horst, William MJ Green, Solomon Assefa, Steven M Shank, Yurii A Vlasov, and Bert Jan Offrein. *Cascaded Mach-Zehnder wavelength filters in silicon photonics for low loss and flat pass-band WDM (de-) multiplexing*. Optics express, 21(10):11652–11658, 2013.

[5] Xu Wang, Wei Shi, Raha Vafaei, Nicolas AF Jaeger, and Lukas Chrostowski. *Uniform and sampled Bragg gratings in SOI strip waveguides with sidewall corrugations*. IEEE Photonics Technology Letters, 23(5):290–292, 2011.

[6] Wim Bogaerts, Peter De Heyn, Thomas Van Vaerenbergh, Katrien De Vos, Shankar Kumar Selvaraja, Tom Claes, Pieter Dumon, Peter Bienstman, Dries Van Thourhout, and Roel Baets. *Silicon microring resonators*. Laser & Photonics Reviews, 6(1):47–73, 2012.

[7] Wim Bogaerts, Pieter Dumon, Dries Van Thourhout, Dirk Taillaert, Patrick Jaenen, Johan Wouters, Stephan Beckx, Vincent Wiaux, and Roel G Baets. *Compact wavelength-selective functions in silicon-on-insulator photonic wires*. IEEE Journal of Selected Topics in Quantum Electronics, 12(6):1394–1401, 2006.

[8] Ashim Dhakal, Ananth Z Subramanian, Pieter Wuytens, Frédéric Peyskens, Nicolas Le Thomas, and Roel Baets. *Evanescent excitation and collection of spontaneous Raman spectra using silicon nitride nanophotonic waveguides*. Optics letters, 39(13):4025–4028, 2014.

[9] Magdalena S Nawrocka, Tao Liu, Xuan Wang, and Roberto R Panepucci. *Tunable silicon microring resonator with wide free spectral range*. Applied physics letters, 89(7):071110, 2006.

[10] Kazuhiro Oda, Norio Takato, and Hiromu Toba. *A wide-FSR waveguide double-ring resonator for optical FDM transmission systems*. Journal of lightwave technology, 9(6):728–736, 1991.

[11] DH Geuzebroek, EJ Klein, H Kelderman, FS Tan, DJW Klunder, and A Driessen. *Thermally tuneable, wide FSR switch based on microring resonators*. In Proc. Symp. IEEE/LEOS Benelux Chapter, pages 155–158, 2002.

[12] Robert Boeck, Michael Caverley, Lukas Chrostowski, and Nicolas AF Jaeger. *Grating-assisted silicon-on-insulator racetrack resonator reflector*. Optics express, 23(20):25509–25522, 2015.

[13] Darius Urbonas, Armandas Balčytis, Martynas Gabalis, Konstantinas Vaškevičius, Greta Naujokaitė, Saulius Juodkazis, and Raimondas Petruškevičius. *Ultra-wide free spectral range, enhanced sensitivity, and removed mode splitting SOI optical ring resonator with dispersive metal nanodisks*. Optics letters, 40(13):2977–2980, 2015.

[14] Ang Li and Wim Bogaerts. *Experimental demonstration of a single silicon ring resonator with an ultra-wide FSR and tuning range*. Optics letters, 42(23):4986–4989, 2017.

[15] Raman Kashyap. *Fiber bragg gratings*. Academic press, 2009.

[16] Amnon Yariv and Pochi Yeh. *Photonics: optical electronics in modern communications (the oxford series in electrical and computer engineering)*. Oxford University Press, Inc, 231:232, 2006.

[17] Ivano Giuntoni, David Stolarek, Andrzej Gajda, Georg Winzer, Jürgen Bruns, Bernd Tillack, Klaus Petermann, and Lars Zimmermann. *Integrated drop-filter for dispersion compensation based on SOI rib waveguides*. In 2010 Conference on Optical Fiber Communication (OFC/NFOEC), collocated National Fiber Optic Engineers Conference, pages 1–3. IEEE, 2010.

[18] Xu Wang, Yun Wang, Jonas Flueckiger, Richard Bojko, Amy Liu, Adam Reid, James Pond, Nicolas AF Jaeger, and Lukas Chrostowski. *Precise control of the coupling coefficient through destructive interference in silicon waveguide Bragg gratings*. Optics letters, 39(19):5519–5522, 2014.

[19] Min Qiu, Mikael Mulot, Marcin Swillo, Srinivasan Anand, Bozena Jaskorzynska, Anders Karlsson, Martin Kamp, and Alfred Forchel. *Photonic crystal optical filter based on contra-directional waveguide coupling*. Applied Physics Letters, 83(25):5121–5123, 2003.

[20] DTH Tan, K Ikeda, and Y Fainman. *Coupled chirped vertical gratings for on-chip group velocity dispersion engineering*. Applied Physics Letters, 95(14):141109, 2009.

[21] W Shi, X Wang, W Zhang, L Chrostowski, and NAF Jaeger. *Contradirectional couplers in silicon-on-insulator rib waveguides*. Optics letters, 36(20):3999–4001, 2011.

[22] Nicholas C Harris, Davide Grassani, Angelica Simbula, Mihir Pant, Matteo Galli, Tom Baehr-Jones, Michael Hochberg, Dirk Englund, Daniele Bajoni, and Christophe Galland. *Integrated source of spectrally filtered correlated photons for large-scale quantum photonic systems*. Physical Review X, 4(4):041047, 2014.

[23] Jun Rong Ong, Ranjeet Kumar, and Shayan Mookherjea. *Ultra-high-contrast and tunable-bandwidth filter using cascaded high-order silicon microring filters*. IEEE Photonics Technology Letters, 25(16):1543–1546, 2013.

[24] Mateusz Piekarek, Damien Bonneau, Shigehito Miki, Taro Yamashita, Mikio Fujiwara, Masahide Sasaki, Hirotaka Terai, Michael G Tanner, Chandra M Natarajan, Robert H Hadfield, et al. *High-extinction ratio integrated photonic filters for silicon quantum photonics*. Optics letters, 42(4):815–818, 2017.

[25] J Wang, I Glesk, and LR Chen. *Subwavelength grating Bragg grating filters in silicon-on-insulator*. Electronics Letters, 51(9):712–714, 2015.

[26] Diego Pérez-Galacho, Carlos Alonso-Ramos, Florent Mazeas, Xavier Le Roux, Dorian Oser, Weiwei Zhang, Delphine Marris-Morini, Laurent Labonté, Sébastien Tanzilli, Eric Cassan, et al. *Optical pump-rejection filter based on silicon sub-wavelength engineered photonic structures*. Optics letters, 42(8):1468–1471, 2017.

[27] Shankar Kumar Selvaraja, Patrick Jaenen, Wim Bogaerts, Dries Van Thourhout, Pieter Dumon, and Roel Baets. *Fabrication of photonic wire and crystal circuits in silicon-on-insulator using 193-nm optical lithography*. Journal of Lightwave Technology, 27(18):4076–4083, 2009.

[28] Roger H French and Hoang V Tran. *Immersion lithography: photomask and wafer-level materials*. Annual Review of Materials Research, 39, 2009.

[29] Pochi Yeh and HF Taylor. *Contradirectional frequency-selective couplers for guided-wave optics*. Applied optics, 19(16):2848–2855, 1980.

[30] Photon Design. *Fimmwave, mode solvers for optical waveguides*. `https://www.photond.com/products/fimmwave.htm`. Accessed: 2019-09-09.

[31] AZ Subramanian, Pieter Neutens, Ashim Dhakal, Roelof Jansen, Tom Claes, Xavier Rottenberg, Frédéric Peyskens, Shankar Selvaraja, Philippe Helin, Bert Du Bois, et al. *Low-loss singlemode PECVD silicon nitride photonic wire waveguides for 532–900 nm wavelength window fabricated within a CMOS pilot line*. IEEE Photonics Journal, 5(6):2202809–2202809, 2013.

[32] Dorian Oser, Florent Mazeas, X Le Roux, Diego Pérez-Galacho, Olivier Alibart, Sebastien Tanzilli, Laurent Labonté, Delphine Marris-Morini, Laurent Vivien, Eric Cassan, et al. *Coherency-broken Bragg filters: surpassing on-chip rejection limitations*. arXiv preprint arXiv:1806.08833, 2018.

[33] Yanlu Li, Diedrik Vermeulen, Yannick De Koninck, Gunay Yurtsever, Günther Roelkens, and Roel Baets. *Compact grating couplers on silicon-on-insulator with reduced backreflection*. Optics letters, 37(21):4356–4358, 2012.

[34] Photon Design. *Fimmprop, optical propagation software - 3D field analysis*. `https://www.photond.com/products/fimmprop.htm`. Accessed: 2019-09-09.

5

Temperature-insensitive Filter

In this chapter, we introduce a new type of temperature-insensitive filter that takes care of both the thermo-optic effect and thermal expansion effect. The concept is patented [1], and the prototyping design is made by former colleagues in our group. In this Ph.D. project, we mainly contribute to the experimental characterization of the fabricated prototype, which is the major topic of this chapter.

Contents

5.1 Introduction

Optical wavelength filters in integrated photonic platforms are usually sensitive to ambient temperature variations. The spectral response tends to drift with temperature, resulting in incorrect wavelength readings. This is especially the case for integrated optical filters implemented in an SOI platform, where the silicon has a large thermo-optic coefficient (TOC) [2]. The thermal drift has two sources: the change of the refractive index of the material due to the thermo-optic effect and thermal expansion of devices. The former describes the temperature-dependence of the refractive index of a material [3] and is often the dominant source. Nevertheless, for accurate measurements, the thermal expansion can not be neglected and should also be compensated. Therefore, for spectroscopic applications or other applications where an absolute determination of optical wavelength is desired, it is required to have a fixed reference wavelength or perform active temperature tracking.

In the past, quite some efforts have been made to provide solutions for overcoming the temperature sensitivity.

- An often proposed solution is to cover the waveguide with a cladding material that has a TOC with an opposite sign. It has been studied that polymers typically have a negative TOC, whereas the TOC of silicon is positive [4, 5]. As such, polymers are often used as the cladding material to compensate for the thermo-optic effect of the silicon waveguide [6–9]. However, these polymer-based approaches often suffer from issues related to chemical instability, higher waveguide losses, long-term reliability, and CMOS incompatibility. A better overcladding material for making athermal silicon waveguides could be titanium dioxide (TiO_2) [10]. It has been reported that TiO_2 is chemically stable as the optical cladding material and can be deposited on silicon as part of the CMOS fabrication process in the future [11].

- Thermally self-compensating optical filters provide another solution [12–14]. It has been reported that a specially designed Mach-Zehnder interferometer (MZI) can be robust against temperature fluctuations. In these approaches, the temperature dependence in the two arms of the MZI is designed to be different and, therefore, can cancel out each other if the appropriate arm lengths are chosen. The difference can be introduced by using different polarization states in the two arms [13] or by designing different waveguide widths [14–16]. These

approaches also have inadequacies in that they are usually sensitive to the fabrication imperfections.

- One can also solve the problem with active thermal compensation. The temperature of the photonic devices can be controlled and kept stable by using external metal heaters [17], using local heating of silicon itself [18, 19] and using a Peltier element that allows for cooling and heating of the chip [20, 21]. These solutions are all active and require large space, high power dissipation, and sophisticated control systems. Also, it could be challenging to reach sufficient stability for spectroscopic applications.

In this chapter, we will propose a new type of wavelength filter that operates athermally. It is substantially temperature-insensitive as both the thermo-optic effect and thermal expansion effect are taken into consideration and are compensated for sufficiently. Furthermore, it can act as a passband filter of which the output can be used as a reference wavelength for on-chip spectroscopic applications.

5.2 Working principle of the temperature-insensitive filter

In figure 5.1, we show a 3D sketch of the proposed temperature-insensitive filter. As illustrated, the proposed filter can be effectively seen as a free-space grating-based filter (with the propagating medium being air). As a result, it could be temperature insensitive if we ignore the thermal expansion effect, which is also compensated for, as will be detailed later.

In operation, the light is first coupled into the photonic chip through a standard on-chip fiber grating coupler. On the chip, the light is guided in a wire waveguide, propagating to a second grating coupler where it is coupled out into the air under a specially designed out-coupling angle. The light propagates in the air until it hits a reflective surface, which can be a small piece of a bare silicon wafer with gold deposited on it. Such a reflective surface will reflect the light back to the chip, landing on the on-chip Littrow grating. The Littrow grating will diffract the light back into the second grating coupler for a specific wavelength, which is filtered in this way.

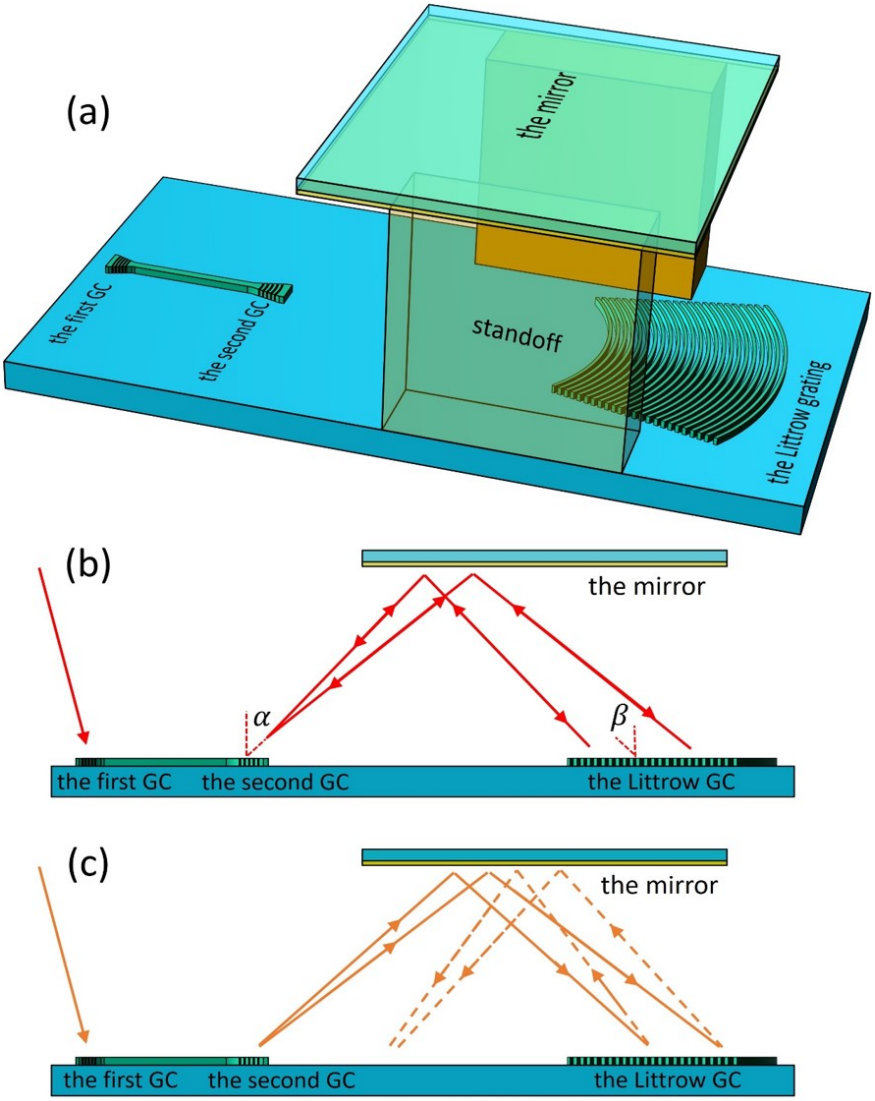

Figure 5.1: (a) A 3D sketch of the proposed temperature-insensitive filter. (b) A side view of the device (the standoff is not drawn) showing the path of the light with a proper wavelength. The light can be reflected and refocused to the second grating coupler after multiple reflections. (c) When considering a different wavelength, the light will end at a different location instead of the second grating coupler.

5.2.1 Littrow grating

The free space propagation starts from the the second grating coupler. For a certain wavelength, the second grating coupler couples the light out (considering the first-order diffraction) at an angle α defined by:

$$n_a \sin\alpha = n_{eff} + \frac{\lambda}{\Lambda}, \tag{5.1}$$

where n_a is the refractive index of the air, n_{eff} is the effective refractive index of the wire waveguide, λ is the wavelength considered and Λ is the period of the second grating coupler.

The Littrow grating diffracts the incident light back along the direction of incidence (considering the first order diffraction), this is expressed by the Littrow condition:

$$n_a(\sin\alpha + \sin\beta) = \frac{\lambda}{D}, \tag{5.2}$$

where β is the reflection angle, and should be equal to the incident angle α. D is the period of the Littrow grating at the position where the center beam of the light lands.

As the light beam coupled out from the second grating coupler will naturally diverge, it contains a plurality of directions. These different directions will land on the Littrow grating at a slightly different location. To ensure the whole light beam can be reflected under the Littrow condition, the Littrow grating has to be chirped, i.e., has a varying grating period at different locations.

The landing location s can be calculated according to:

$$s = 2h\tan\alpha, \tag{5.3}$$

where h is the height of the metal mirror with respect to the chip. Combining the equation 5.2 and 5.3, the chirped period as a function of landing position s can be then calculated with:

$$D(s) = \frac{\lambda}{2n_a(\lambda, T)}\sqrt{1 + (\frac{2h}{s})^2} \tag{5.4}$$

In this way, the reflected light beam will have the same phase front as the incident beam. After propagating towards and being redirected by the mirror, the reflected light beam will automatically be refocused on the second grating coupler and coupled back into the wire waveguide. This situation is depicted in 5.1 (b).

For light signals with a substantially different wavelength, the Littrow condition is not satisfied, deviating the reflection angle β from the incidence angle α. As a result, instead of returning to the second grating coupler, these light signals will end up at a different location rather than the position of the second grating coupler as depicted in 5.1 (c). Therefore, the light can not be coupled into the wire waveguide. Such a spatial separation effect allows for rejection of the wavelengths in the stop-band.

5.2.2 Temperature insensitivity

The temperature insensitivity is achieved with the compensation of two effects: the thermo-optic effect and the thermal expansion.

Firstly, the thermo-optic effect describes the change of the effective refractive index induced by the temperature variation. For a fixed wavelength, due to the change in effective refractive index, the out-coupling angle α of the second grating coupler will change according to equation 5.1, leading to a change of the landing location on the Littrow grating. The chirping of the Littrow grating ensures that this will not affect the operation as long as the thermo-optic effect for the off-chip propagation is negligibly small. This holds for air with TOC around 10^{-6} /K which is two orders of magnitude smaller to that of silicon. In such a case, we can see from equation 5.3 that the chirp rate does not change with temperature and is completely determined by h, the height of the mirror and λ, the center wavelength of the pass-band.

On the other hand, we still need to compensate for thermal expansion. When the photonic chip is considered to be a silicon-based chip, all dimensions of the chip expand with a thermal coefficient of ϑ_{si}. This means a new position s_{new} after thermal expansion can be related to the old position s_{old} as:

$$s_{new} = s_{old}(1 + \vartheta_{Si}\Delta T). \tag{5.5}$$

The grating period D also expands as the temperature changes, which can be expressed as:

$$D_{new} = D_{old}(1 + \vartheta_{Si}\Delta T). \tag{5.6}$$

Assuming the mirror is supported by the standoff which has a thermal expansion coefficient of ϑ_{so}, the height of the mirror also changes as:

$$h_{new} = h_{old}(1 + \vartheta_{so}\Delta T) \tag{5.7}$$

By combining these expansions, we see a light ray coupled out from the second grating coupler under an angle of α will land on the Littrow grating

at s_{new} given by $2h_{new}\tan\alpha$. Due to thermal expansion, the grating period one can find at this new position was initially at s_{old} and has also expanded as

$$D_{new}(s_{new}) = \frac{\lambda_{old}}{2}\sqrt{1+(\frac{2h_{old}}{s_{new}(1-\vartheta_{Si}\Delta T)})^2}(1+\vartheta_{Si}\Delta T) \tag{5.8}$$

With this expression, one can calculate the new wavelength that fulfills the Littrow condition at this new position.

$$\begin{aligned}\lambda_{new} &= 2D_{new}\sin\alpha \\ &= \lambda_{old}\sin\alpha\sqrt{1+(\frac{2h_{old}}{2h_{new}\tan\alpha(1-\vartheta_{Si}\Delta T)})^2}(1+\vartheta_{Si}\Delta T)\end{aligned} \tag{5.9}$$

Considering first-order expansion, equation 5.9 can be approximated to

$$\frac{\lambda_{new}}{\lambda_{old}} = 1+[\vartheta_{Si}+\cos^2\alpha(\vartheta_{Si}-\vartheta_{so})]\Delta T. \tag{5.10}$$

In order to compensate the wavelength shift due to thermal expansion, the right-hand side of equation 5.10 should equal to 1. This will give the relation between the thermal expansion coefficients of the silicon and the standoff.

$$\vartheta_{so} = \vartheta_{Si}\frac{1+\cos^2\alpha}{\cos^2\alpha} \tag{5.11}$$

Equation 5.10 tells us that the thermal expansion can be compensated by the standoff with a proper thermal expansion coefficient. For instance, in the case where α is set to 45 degrees, this results in the condition $\vartheta_{so} = 3\vartheta_{Si}$, i.e., the standoff should expand three times faster than silicon.

5.3 Designs in the prototype

The prototype of the temperature-insensitive filters, operating at the center wavelength of 1550 nm was designed by the former Post-Docs in our group (Eva Ryckeboer, Thijs Spuesens and Abdul Rahim), and are fabricated by Imec in an SOI passive run (EP5524 EP19 PSV).

The GDS view of the design is shown in figure 5.2. As marked by the red frame and presented in the zoom-in on the right side, there are two clusters of grating couplers connected by wire waveguides sitting below the Littrow gratings. Instead of having only one waveguide that connects a first grating coupler and a second grating coupler, we have multiple copies. This allows us to have multiple choices in using one waveguide to couple the light into the chip and using another as the receiving channel. By separating the input and output channel, we can avoid the situation where the back reflections of input light at the grating couplers conceal the weak signal that we want to measure.

In the design, the first grating couplers, used to couple the light from the optical fibers to the photonic chip, are the standard grating couplers operating at around 10-degree diffraction angle with respect to the normal of the chip. The second grating couplers are designed to couple the light out from the photonic chip at the diffraction angle α of around 45 degrees. Two Littrow gratings respectively have 1500 and 3000 periods, all chirping from 1.347 μm to 0.967 μm. The distances between the center second grating coupler and the center of the first and the second Littrow gratings are 2 mm and 4 mm, meaning the proper height of the mirror should be 1 and 2 mm, correspondingly. It is worth to mention that, in the current design, the Littrow grating only serves the purpose of refocusing light to a predetermined spot. No effort was made to make it with a high efficiency.

5.4 Experimental characterization

With the fabricated device, we first couple the light into the chip from a first grating coupler. The light will propagate in the corresponding waveguide towards the second grating coupler which couples the light out at the diffraction angle α. In order to reflect the light back to the chip at the location where the Littrow gratings sit, we need to position a reflective surface above the chip, facing down. This can be a mirror made from a piece of silicon bare wafer with gold deposited on one side. The reflected light landing on the Littrow gratings will be reflected by the Littrow gratings, reversing the propagating direction and going back to the mirror. After reflecting again by the mirror, the light will return to the chip, creating a reflected spot in the vicinity of the second grating coupler.

The initial characterization was conducted together with Anton Vasiliev, a colleague in the photonics research group. We first wanted to check if we can find this reflected spot. While coupling light into the chip with the op-

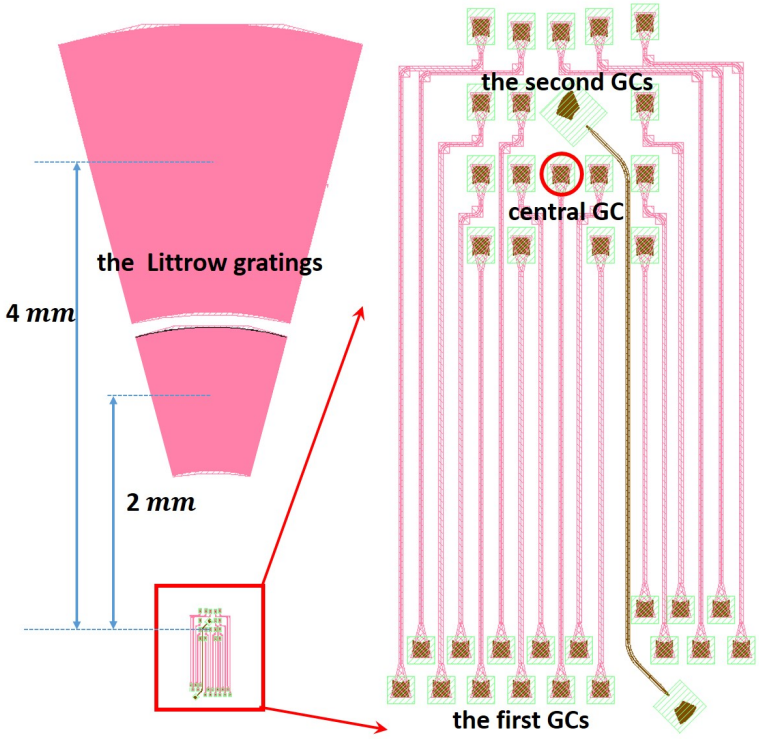

Figure 5.2: The GDS view of the first design of the temperature-insensitive filter. On the right side is a zoom-in of the grating couplers and the wire waveguides connecting them. On the left, there are two Littrow gratings, with the center at the distance 2 and 4 mm from the center second grating coupler.

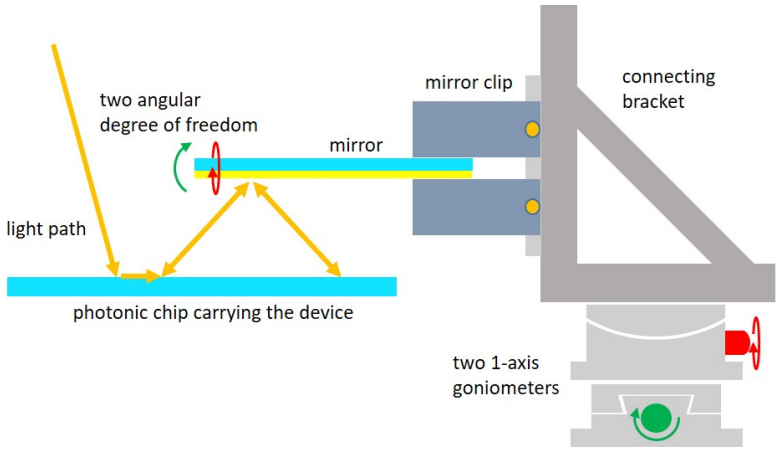

Figure 5.3: The sketch of a temporary solution for mirror positioning. The mirror is clipped by two pieces of metal installed on two 1-axis goniometers. The mirror and the photonic chip are exaggerated and not of scale.

tical fiber and the on-chip grating coupler is straightforward, to position a mirror in parallel to the photonic chip at a proper distance is tricky. As shown in the sketch in 5.3, we use a clip (constructed with two pieces of metal mounted on a rail) to hold the mirror. To give the mirror two angular degrees of freedom, we attach the clip through a connecting bracket to two 1-axis goniometers (GNL10, Thorlabs) that are installed in an orthogonal way. The clip and the two goniometers are then mounted on a 3-axis translation stage (not drawn in the sketch) to allow 3-dimension linear movements. Also not depicted in the sketch, the photonic chip is held by a thermo-electric heater to allow precise temperature control.

The light emitted from a tunable laser (Santec TSL-550) first goes through a fiber-based polarization rotator to allow optimized polarization for the light coupling into the device. The fiber-to-chip alignment is performed with the help of an infrared (IR) camera (Xenics XEVA-2837) above the chip, which provides a top view.

When the input fiber is aligned to the first grating coupler, we can see the scattered light from the corresponding second grating coupler. The mirror is positioned to cover the Littrow gratings while leaving the first and second grating couplers exposed to the camera. After adjusting the height of the mirror and rotating the two goniometers, we managed to observe the reflected spot in the view of the IR camera. In figure 5.4, we show a camera view that contains three observable features. The bottom one marked

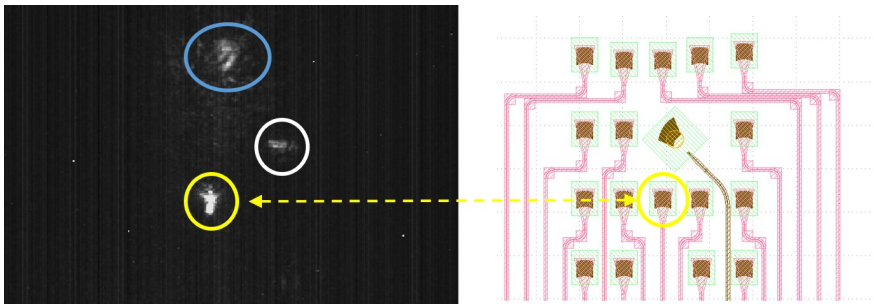

Figure 5.4: The camera view showing the scattered light from the second grating coupler (in the yellow circle), the reflected spot (in the white circle) and the reflection coming from the substrate (in the blue circle).

by the yellow circle is the light scattered into the camera from the second grating coupler. The one in the white circle is the reflected spot, as it moves when we slightly rotate the goniometers or change the wavelength. As for the top one marked with the blue circle, we suspect it to be the scattered light coming from the input light reflected from the substrate.

5.4.1 Measure the spectral response

Once we can see the reflected spot, we need to quantitatively measure the reflected spot and see how it varies as the wavelength changes. There are two approaches to do this.

5.4.1.1 Measurement with one optical fiber and the IR camera

In the first approach, we can directly measure the reflected spot in the pictures captured by the IR camera. As the reflected spot is reflected on the surface of the photonic chip at the angle of around 45 degrees, we mount the IR camera also at 45 degrees to efficiently collect the light. We take pictures for different input wavelength and record the shifting of the reflected spot towards the first grating coupler. By integrating the pixel responses in a small area at a fixed position in the camera view, we can get the spectral response of the device.

In figure 5.5, we show three pictures obtained from the obliquely mounted camera. In the figure, we can see that as the wavelength changes, the reflected spot shifts downwards, sweeping through the integration window that has a certain dimension at a fixed position. Marked in the white frame

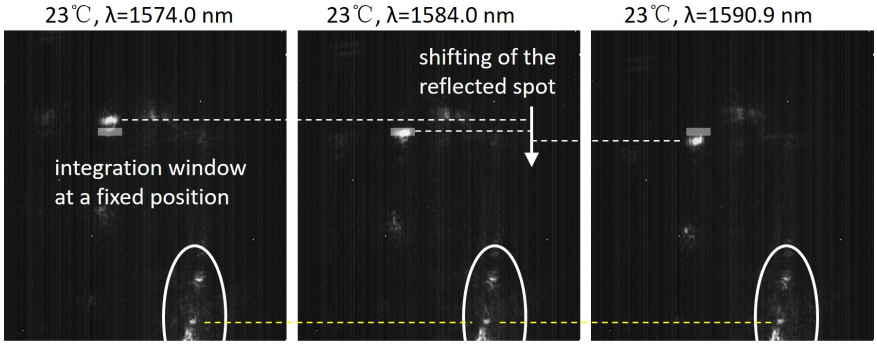

Figure 5.5: Camera pictures showing that the reflected spot moves as wavelength changes. For different wavelength, we see the reflected spot sweeps through the integration window (at a fixed position).

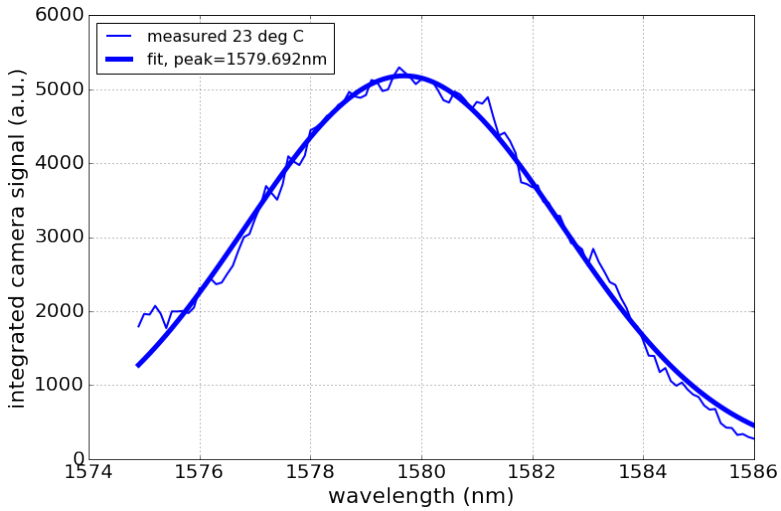

Figure 5.6: Spectral response measured with the IR camera. The integrated camera signal changes as the reflected spot sweeping through the fixed integration window.

is the scattered light coming from the second grating coupler, which stays still as the wavelength varies. To measure the spectral response, we need to take a series of pictures for the reflected spot at different wavelengths. The signal strength is the sum of the pixel responses inside the fixed integration box (as shown in figure 5.5 with the dimension of 2 pixels $\times$ 15 pixels). The reflected spot moves as the wavelength changes, resulting in a varying integrated camera signal as a function of the wavelength. The direction of the movement, i.e., the spot moves away from the Littrow grating as the wavelength increases, corresponds with the theoretical prediction. The obtained spectrum measured at the temperature of 23 degree Celsius is shown in figure 5.7. With the Gaussian fitting, we can find the peak at around 1580 nm.

5.4.1.2 Measurement with two optical fibers

In the second approach, we can tune the goniometers and steer the reflected spot to one of the second grating couplers. As such, the reflected light can be coupled into the corresponding waveguide and propagate to the corresponding first grating coupler. From this grating coupler, we can use another optical fiber to collect the light and send it to a power meter to quantitatively measure the optical power. As the input wavelength varies, the reflected spot will shift and move away from the receiving second grating coupler, decreasing the optical power that can be measured by the power meter. Since only for a particular wavelength, the reflected spot can land precisely at the location of the receiving second grating coupler, the measured power spectrum should have a peak centered around this wavelength. Such a spectrum measured at 25 degree Celsius is shown in figure 5.7, where a pass-band peak can be observed with the center wavelength fitted around 1586 nm.

5.4.2 Measure temperature sensitivity with non-optimized mirror positioning

After demonstrating that we can measure the spectrum, the next step is to measure how it changes with the temperature variations. However, things can go wrong if the mirror is not at the correct height or is tilted considerably. In fact, with the current setup, it is practically difficult to know the distance between the mirror and photonic chip accurately, let alone to keep them in parallel. While being in a non-optimized situation, it is still interesting to see how the spectral response varies with temperature changes.

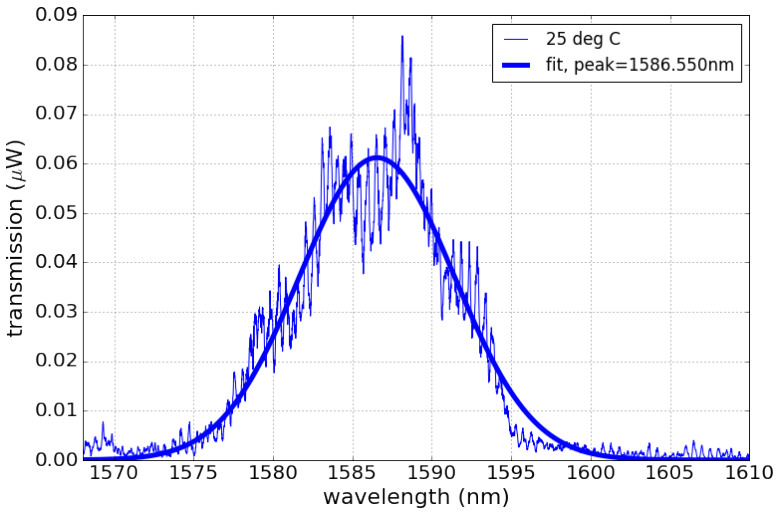

Figure 5.7: The optical power collected by a second optical fiber plotted as the function of wavelength.

With the Peltier heater, we can change the temperature of the photonic chip. However, as we heat up or cool down the device, the sample holder (an aluminum block) will expand or shrink, raising or lowering the photonic chip with respect to the mirror that is fixed by the clip. The changing of mirror height as such is an undesired side-effect and should be eliminated. For this purpose, we need to glue the mirror to the photonic chip, after which we can measure the spectra under different temperature.

5.4.2.1 Measurement with one optical fiber and the IR camera

In one experiment, we measure with the obliquely mounted IR camera. We first glue two pieces of glass (that is transparent for UV light) at the two sides of the Littrow gratings with UV glue. The thickness is around 0.5 mm for both pieces. The glue cures upon exposure to UV light. These two pieces of glass will be the standoff that holds the mirror as shown in figure 5.1 (a). After that, we align the input fiber and inject the laser light into one of the first grating couplers. After the alignment, we position the mirror, trying to make it as parallel as possible to the chip. We apply the glue to fill the gap and cure it. During the process, we are careful not to cover the Littrow gratings with the glue. When the glue is fully cured, the mirror can be released from the clip as it now adheres to the photonic

chip. With the thermoelectric heater, we set the temperature to 17, 23, and 35 degree Celsius and take a series of pictures for the reflected spot at each temperature. With these pictures, we can extract the spectral response with the approach mentioned above at different temperatures. The results are shown in figure 5.8, in which we can see the shifting of the peak as temperature changes. Linear fitting indicates the rate of spectral shift is around -100 pm/K.

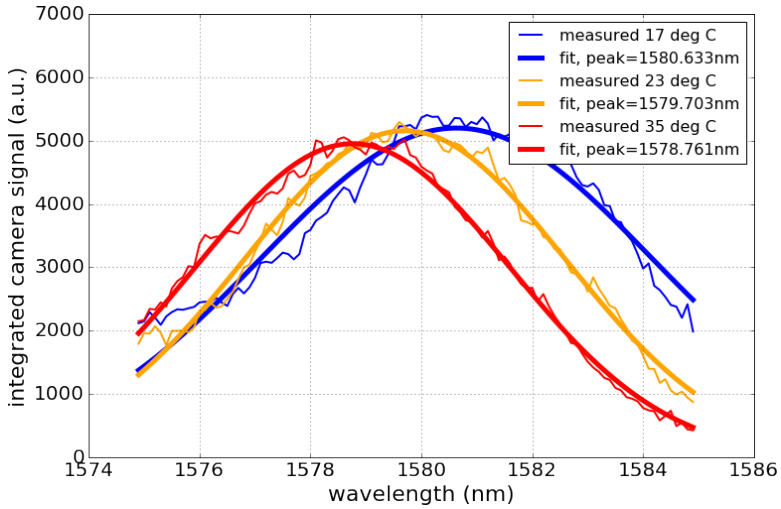

Figure 5.8: The integrated camera signal as the function of wavelength obtained with the IR camera at the temperature of 17, 23 and 35 degree Celsius.

5.4.2.2 Measurement with two optical fibers

In another experiment, we use two optical fibers to collect the signal. Similarly, we first glue on the two sides of the Littrow gratings two pieces of glass, which act as the standoff. Next, we do the alignment for the input fiber, position the mirror, and steer the reflected spot to the receiving second grating coupler. As such, we can align the second optical fiber to the grating coupler that is connected to the receiving second grating coupler. We can, therefore, collect the light and read the signal strength with a power meter. After the alignment, we apply the UV glue to fill the gap between the glass and the mirror. When the glue is fully cured, we see that the spacing between the chip and the mirror is roughly around 0.7 mm, and the tilting is more or less around 9 degrees.

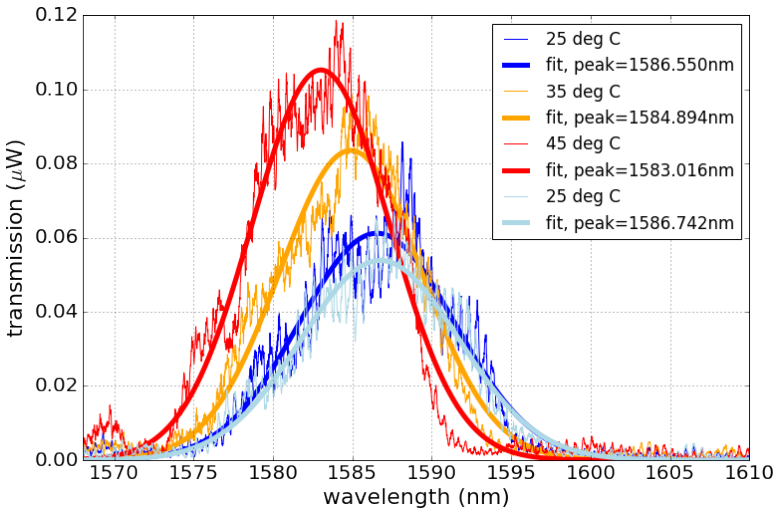

Figure 5.9: The spectra measured with the two-fiber approach at 25, 35, 45 and 25 degree Celsius, successively.

With the mirror glued to the photonic chip, we change the temperature with the thermoelectric heater beneath the chip and scan the tunable laser to measure the spectral response. We first measure the spectrum at 25 degree Celsius and then heat the chip to measure at 35 and 45 degree Celsius. After that, we cool the heater and measure again at 25 degree Celsius to confirm the measurement. In figure 5.9, we show the measured spectra. The shifting of the peak can be observed. With the linear fitting of the peak positions as a function of temperature, we found the rate of spectral shifting around -180 pm/K.

Temperature sensitivity

The preliminary measurement results indicate that the temperature-induced spectral shift of our device is much larger than expected. Although we can measure the reflected spot, it should be noticed that in these experiments, the mirror is not appropriately positioned and the standoff (i.e., the combination of thick glue and the glass plate) is not with the correct thermal expansion coefficient. The spacing between the mirror and the photonic chip ($\sim$ 0.7 mm) is smaller than the desired value of 1 mm. The consequence is that the reflected spot is only observable in the view of the IR camera for light with the wavelength around 1580 nm. This is already far away from

the designed center wavelength of 1550 nm. In the experiments, in order to see the reflected spot in the view of the IR camera, the improper spacing is actually compensated by a large tilt ($\sim$ 9 degree) of the mirror. All these deviations join together and lead to the increased temperature sensitivity.

5.4.3 Measure temperature sensitivity with a mirror "bridge"

As a result of what we learned from the previous experiments, and in order to have the desired small temperature sensitivity, we have to measure with the mirror positioned approximately correctly, i.e., the spacing between the photonic chip and the mirror is close to the design value (1 mm), and the two are in parallel. To this end, we want to fabricate a mirror "bridge", which, as shown in figure 5.1, is a mirror supported by two standoffs. NBK-7 glass can be a good standoff as its thermal expansion coefficient (7.1×10^{-6}/K) is around three times the thermal expansion coefficient of silicon (2.6×10^{-6}/K). A piece of the NBK-7 glass plate is purchased and has an initial thickness of 1030 μm. We first thin down the glass wafer targeting at the thickness of slightly less than 1 mm. Next, we cut it into small squares. Two pieces with the same proper thickness are selected and glued (with the glue layer thickness < 1 μm) to a piece of gold deposited bare silicon wafer. As shown in figure 5.10 (a), we managed to make a mirror "bridge", with which the mirror can be held near parallel to the photonic chip with an average height of around 997 μm. The actual fabrication is done by our colleague, Muhammad Muneeb, in our cleanroom.

5.4.3.1 Measurement with one optical fiber and the IR camera

When we put the mirror "bridge" on the photonic chip, the mirror is sort of in a fixed position, and there is no freedom to adjust its tilt. In this case, the reflected spot might not happen to just land on a second grating coupler. Therefore, we first try to measure with the approach using the obliquely mounted camera. In the experiments, we first align the input fiber to the input first grating coupler. Next we carefully put the mirror "bridge" (facing down) on the photonic chip as shown in figure 5.10 (b) and (c). The mirror "bridge" is designed to guarantee that when its edge is more or less aligned to the edge of the photonic chip, the standoff will not cover the Littrow gratings.

Once the mirror "bridge" is in position, the reflected spot shows up in the view of the camera. Figure 5.11 shows the pictures obtained from the IR

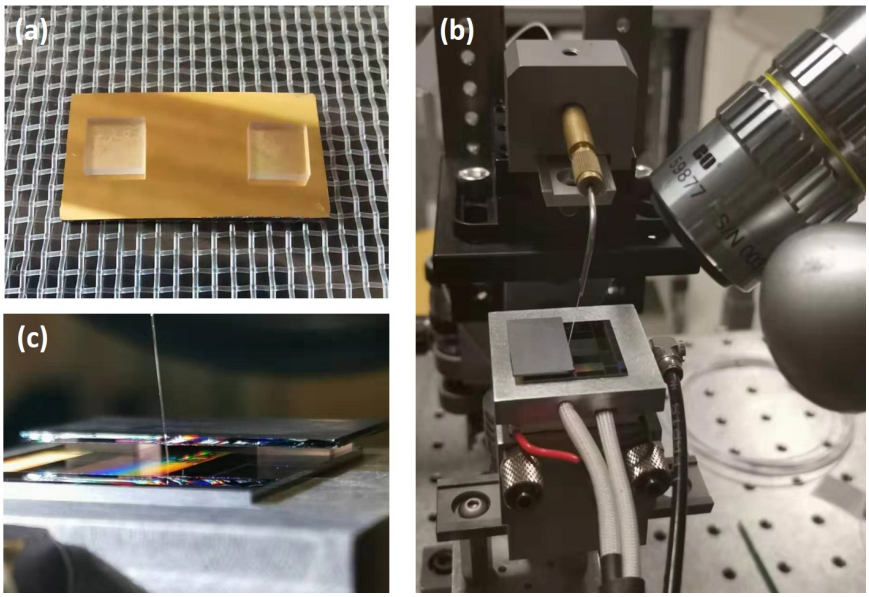

Figure 5.10: (a) The fabricated mirror "bridge" (facing up) with two piece of NBK-7 glass as the standoff glued on a piece of gold deposited bare silicon wafer. (b) A picture of the aligned setup: the lens is mounted on the IR camera for collecting the light. (c) A zoom-in of the fiber and the chip with the mirror "bridge"standing on it.

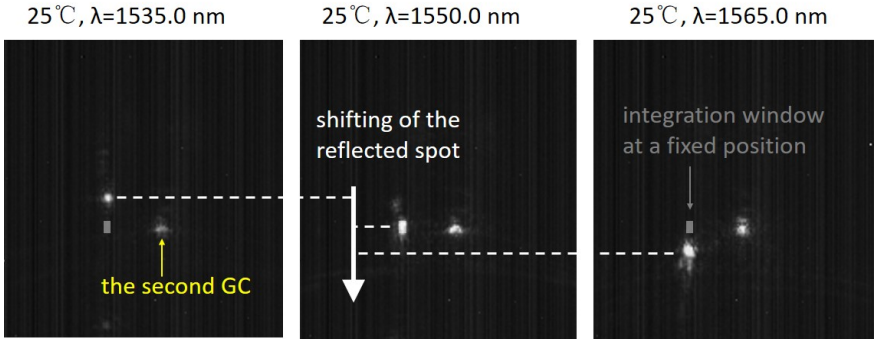

Figure 5.11: Camera pictures showing that the reflected spot sweeps through the integration window (at a fixed position) as the input wavelength changes.

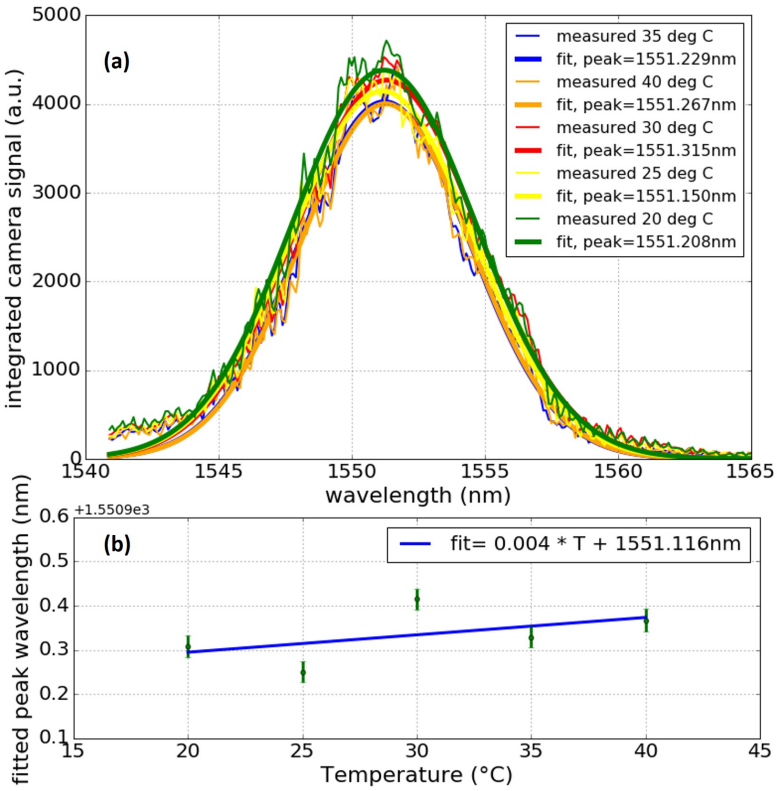

Figure 5.12: (a) The spectra from integrated camera signal at the temperature of 20, 25, 30, 35 and 40 degree Celsius. (b) Linear fitting of the peak positions for different temperature. The error bars show the 1-sigma errors of peak positions.

camera with different input wavelengths. Again we can observe the shifting of the reflected spot when input wavelength changes in the range around 1550.0 nm. We define an integration window with the dimension of (4 pixels $\times$ 7 pixels) at the fixed position aligned to the reflected spot in the picture obtained for 1550.0 nm input wavelength at the temperature of 25 degree Celsius. Using the same integration window, we measure the spectral response of the device at different temperatures.

In figure 5.12 (a), we show the measured spectra, which almost have the same peak position at around the wavelength of 1551.2 nm in the temperature range from 20 to 40 degree Celsius. We extract the peak positions with Gaussian fitting. The peak positions are displayed in the legend in figure 5.12 (a) and are plotted in figure 5.12 (b) with linear fitting indicating the temperature sensitively is only 4 pm/k. Compared to previous results, this

looks promising and encourages us to think that the proposed temperature-insensitive filter should work once the mirror is positioned properly and the thermal expansion coefficient of the standoff is correct.

5.4.3.2 Measurement with two optical fibers

Furthermore, we want to see if we can measure the same result with the two-fiber approach. The setup is shown in figure 5.13 (a), where two optical fibers are used to couple the light into the chip and to collect the returned signal. With the input fiber aligned to the input first grating coupler as marked in figure 5.13 (d), we can see the light scattered from the emitting second grating coupler. Next, we carefully put the mirror "bridge" onto the photonic chip, as shown in 5.13 (c). We can immediately observe the reflected spot landing on the receiving second grating coupler as marked in 5.13 (d). One can see that the emitting and the receiving second grating couplers are symmetric about the center grating coupler. This is because the Littrow grating are designed as an array of circular grating lines.

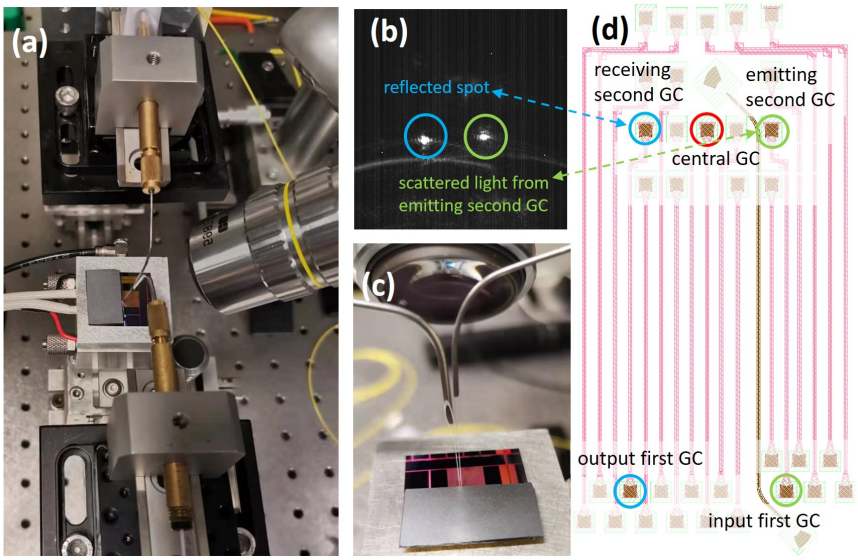

Figure 5.13: (a) A picture of the aligned setup: two fibers are aligned to the corresponding first grating couplers as indicated in (d). (b) The view of the IR camera showing the scattered light from the emitting second grating coupler and the reflected spot landing on the receiving second grating coupler. (c) A zoom-in of the two fibers and the chip with the mirror "bridge" standing on it. (d) The GDS view of the grating couplers.

We can see from figure 5.13 (b) that the reflected spot almost lands on a receiving second grating coupler as marked in 5.13 (d). As a result, the reflected spot can be coupled into the receiving grating coupler and therefore can be collected by a second fiber aligned to the output first grating coupler as also marked in 5.13 (d).

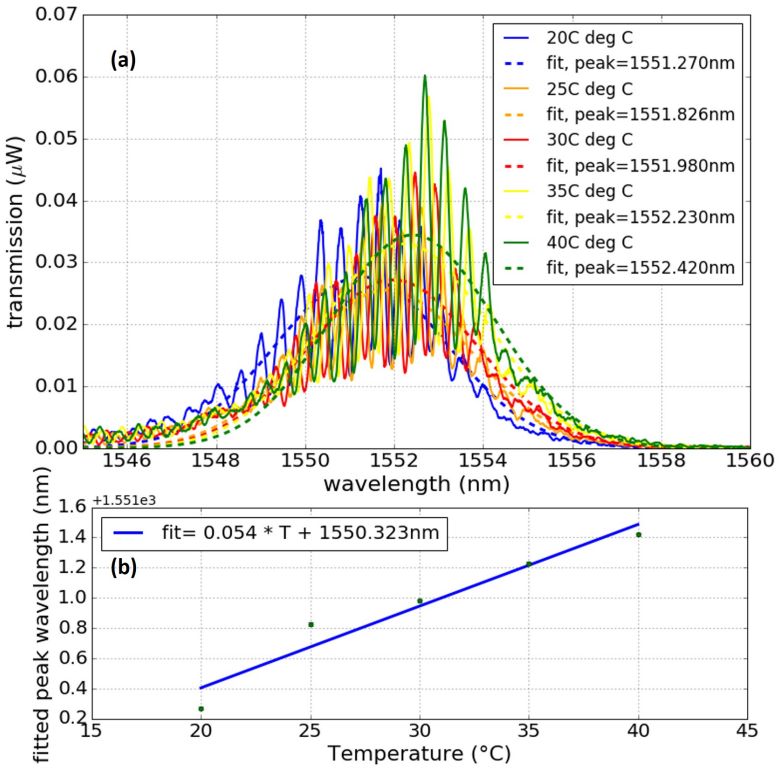

Figure 5.14: (a) Transmission spectra measured at the temperature of 20, 25, 30, 35 and 40 degree Celsius. (b) Linear fitting of the peak positions for different temperature. The error bars show the 1-sigma errors of peak positions.

With the input laser power of 1 mW, we scan the wavelength and measured the transmitted power at different temperature. From the measured spectra, we can fit the peak position and estimate the temperature sensitivity. The results are shown in figure 5.14. There are two things beyond our expectation. Firstly, the measured spectra are superpositioned by spectral fringes with a large modulation depth, as one can clearly see in figure 5.14 (a). Secondly, it is surprising to see that the center wavelength of the passband drifts with the temperature at a rate of around 54 pm/K, as shown in the linear fitting in figure 5.14 (b).

Spectral fringes

The spectral fringes superposed on the transmission spectra may have two possible origins. Firstly, it could be of the Fabry-Perot (FP) type generated by the interference of the strong reflections from different locations in the circuit. In our case, in order to explain the strong fringes, we need to find the "FP cavity" formed by two interfaces with strong reflection. By calculating the Fourier transform of the measured spectra, we can determine the optical path length of the "FP cavity" to be around 2.67 mm. Such an "FP cavity" could be in the air with the same physical length or in silicon with the physical length determined also by the group index. However, after searching, we failed to find two reflection interfaces that meet the requirements.

It is therefore attractive to think that the fringes are of the MZI-type. In this case, there should be two parallel light paths with the optical path difference of around 5.34 mm. Such parallel paths should be related to the mirror. By comparing the 2-fiber results obtained from the glued mirror and the mirror bridge, we found that as the mirror becomes more parallel to the photonic chip, the modulation depth of the fringes increases. It turns out that there are indeed two light paths that could explain the fringes. We have mentioned the first light path along which the light first goes to the mirror from the emitting second grating coupler, then propagates to the first Littrow grating, where it is reflected back to the mirror again and finally ends at the receiving second grating coupler. The second light path also starts from the emitting second grating coupler and goes to the mirror and then the Littrow grating. While we emphasized the part of the light that is reflected by the Littrow grating to propagate back along the incident direction, there are some light (in fact a large portion) could be reflected to propagate in the forward direction as in the case of being reflected by a mirror. The light will propagate to the mirror again, which reflects it to the second Littrow grating.

The second Littrow grating will then do the same job as the first Littrow grating and reflect the light back to the mirror along the incident direction as shown in figure 5.16 (a). This makes sense as the second Littrow grating is designed to work with a mirror held at a height of 2 mm as shown in figure 5.16 (b). Geometry tells us the landing locations on the second Littrow grating are the same in both cases as shown in 5.16 (a) and (b). As a result, the light can return to the receiving second grating coupler. The optical path difference can be calculated as $\frac{4}{\cos\alpha}$, assuming the group index of 1 for the air. We characterized the reference structure of the second grating coupler.

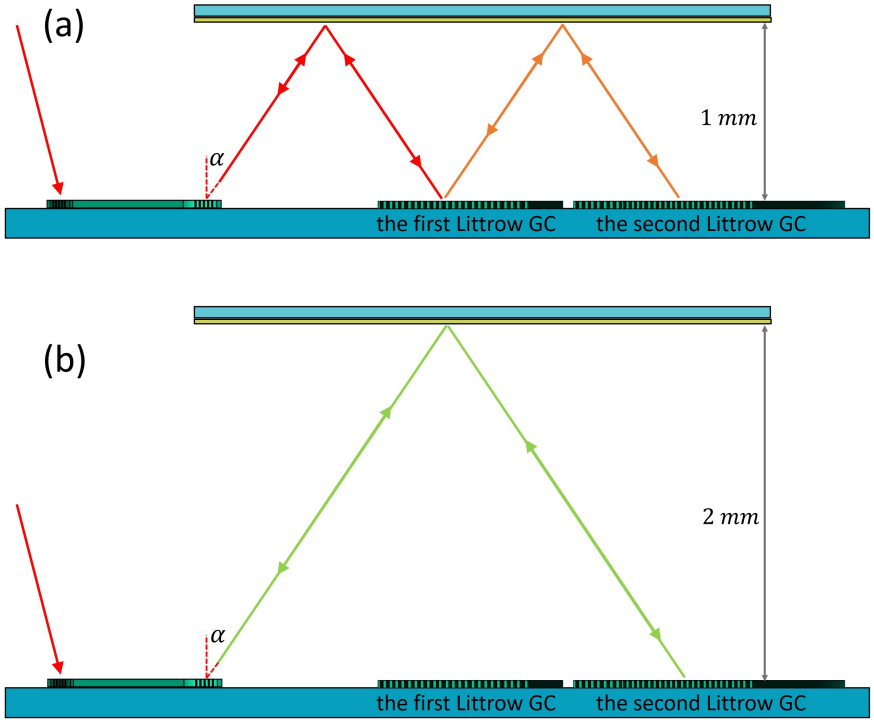

Figure 5.15: (a) An illustration of the second light path. The orange part is the additional path compared to the first light path. (b) An illustration of the light path when holding the mirror at 2 mm above the photonic chip.

The out-coupling angle α at the wavelength of 1550 nm is around 41.5 degrees, which leads to the OPD of 5.34 mm, in agreement with expectation. As the conclusion, we should be able to remove the strong fringes by covering the second Littrow grating.

Temperature sensitivity

There is also an unexpected temperature sensitivity. We think the problem should originate from the fact that the mirror is still not exactly in parallel to the photonic chip and the hypothesis that the temperature sensitivity is affected by the degree of parallelism. There is experimental evidence supporting this opinion.

In the experiments, when we put the mirror bridge onto the aligned photonic

chip, the reflected spot jumps out in the view of the IR camera. We found that slight changes in the position of the mirror can lead to variations of the location of the reflected spot. This is shown in figure 5.16.

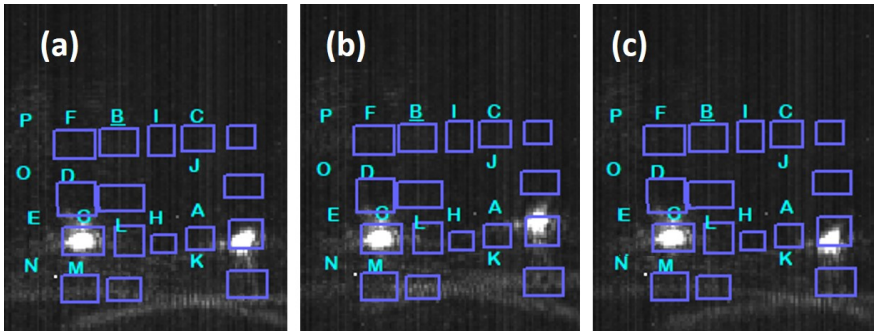

Figure 5.16: Three pictures obtain from the IR camera with input wavelength of 1552.5 nm. In each picture, the fixed blue frames roughly mark the position of the second grating couplers, the spot on the left side is the emitting spot and the right one is the reflected spot. The measured transmitted power is -43.0 dBm in (a), -51.1 dBm in (b) and -43.5 dBm in (c).

In these three pictures, the blue frames roughly marked the location of the second grating couplers and could reference the shifting of the reflected spot as they are fixed in the pictures. The input wavelength 1552.5 nm and the temperature is set to 30 degree Celsius. We can see that while the emitting spot (the one on the left side in each picture) stays still, the reflected spot (on the right side) shifts slightly, leading to different transmitted power (-43.0 dBm, -51.1 dBm and -43.5 dBm, respectively). The shifting supports the idea that the mirror is not strictly parallel to the photonic chip.

For different positions of the mirror bridge, we measured the transmission spectra to see if the temperature sensitivities are different. In these measurements, we covered the second Littrow grating with a small piece of thin foil. As discussed before and as will be confirmed by the following experimental results, by doing so, we can get rid of the strong fringes. Furthermore, we place a small weight on top of the mirror bridge to make it more stable when sitting on the photonic chip. After the measurements, again, we extract the peak wavelengths of the measured transmission spectra with Gaussian fitting and estimate the temperature sensitivity by fitting the peak wavelengths as a function of temperature with a linear equation. Different temperature sensitivities can be observed in different cases. For example, it could be around 23 pm/K as shown in 5.17 (a) for the case in figure 5.16 (a). In the worst case, the peak wavelength is around 1558 nm,

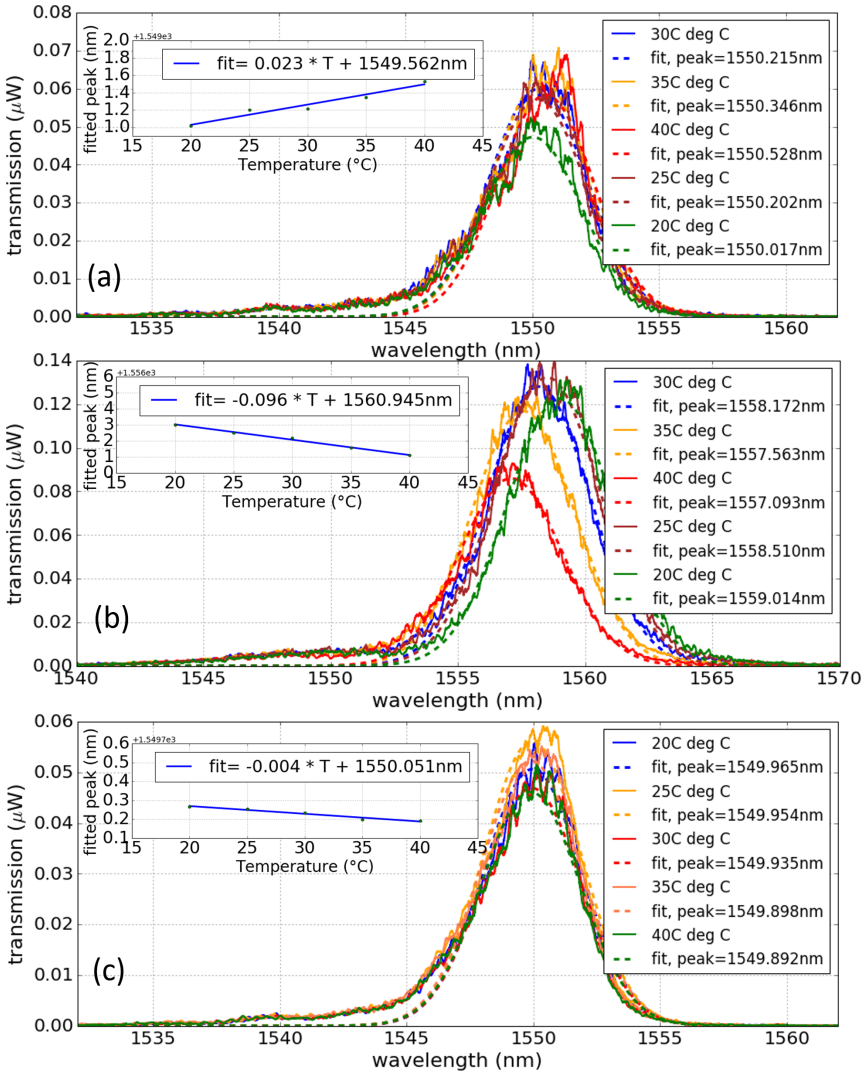

Figure 5.17: Measured spectra for the three cases as shown in 5.16. The insets show the linear fitting of the peak positions at different temperature. The error bars show the 1-sigma errors of peak positions. The temperature sensitivity is 23 pm/K in (a), -96 pm/K in (b) and -4 pm/K in (c).

leading to a drifting rate of -96 pm/K, as shown in 5.17 (b) corresponding to the case in figure 5.16 (b). We also managed to get a rather insensitive situation where the drifting rate is -4 pm/K with the center wavelength of the passband around 1550 nm as shown in 5.17 (c) corresponding to the case in figure 5.16 (c).

These measurement results, on the one hand, indicate that the proposed filter can, in essence, work as a temperature-insensitive filter. On the other hand, they also evidence that there is a critical factor influencing the temperature sensitivity. So far, we know that the mirror is not strictly in parallel to the photonic chip. We can deduce that, by slightly moving the mirror bridge, we are also changing the actual mirror height seen by the light beam, and somehow the drift rate is sensitive to this height for a given small tilting angle. However, to what extent these two factors (height and tilting angle) influence the temperature sensitivity remains a question. While not included in this thesis due to time limitation, for future work, it would be useful to develop a model that can quantitatively describe the influence, which might also give a clue what are the tolerable deviations for the desired temperature insensitivity.

5.5 Conclusion

In this chapter, we presented work on an integrated temperature-insensitive filter. We explained how this filter can compensate for the spectral drifts induced by both the thermo-optical effect and the thermal expansion effect. We demonstrated various experiments conducted for characterizing the fabricated prototype. In the preliminary experiments, we measured a negative drift rate of more than -100 pm/K, which we conclude is due to the non-optimized mirror position. After that, we made a mirror "bridge" of which the standoff has the desired thermal expansion coefficient, and the mirror position is close to optimum. In the experiments, we noticed different temperature sensitivities could be obtained by slightly moving the mirror "bridge". Although with low reproducibility, the best result we obtained is a drift rate of -4 pm/K. We believe that, with further improvements in the packaging approach for the external mirror, the filter should work stably and could be useful for providing an athermal on-chip wavelength reference for on-chip spectroscopic applications.

References

[1] Roel Baets, Eva Ryckeboer, Abdul Rahim, Anton Vasiliev, and Xiaomin Nie. *Temperature insensitive filter*. WO2019129798 (A1), 2019.

[2] Yatendra Pal Varshni. *Temperature dependence of the energy gap in semiconductors*. physica, 34(1):149–154, 1967.

[3] Hiroshi Nishihara, Masamitsu Haruna, and Toshiaki Suhara. *Optical integrated circuits*. New York, pages 7–8, 1989.

[4] Gorachand Ghosh. *Handbook of optical constants of solids: Handbook of thermo-optic coefficients of optical materials with applications*. Academic Press, 1998.

[5] John M Jewell. *Model for the thermo-optic behavior of sodium borate and sodium aluminosilicate glasses*. Journal of non-crystalline solids, 146:145–153, 1992.

[6] Vivek Raghunathan, N Ye Winnie, Juejun Hu, Tomoyuki Izuhara, Jurgen Michel, and Lionel Kimerling. *Athermal operation of silicon waveguides: spectral, second order and footprint dependencies*. Optics express, 18(17):17631–17639, 2010.

[7] Jong-Moo Lee, Duk-Jun Kim, Hokyun Ahn, Sang-Ho Park, and Gyungock Kim. *Temperature dependence of silicon nanophotonic ring resonator with a polymeric overlayer*. Journal of Lightwave Technology, 25(8):2236–2243, 2007.

[8] Jie Teng, Pieter Dumon, Wim Bogaerts, Hongbo Zhang, Xigao Jian, Xiuyou Han, Mingshan Zhao, Geert Morthier, and Roel Baets. *Athermal Silicon-on-insulator ring resonators by overlaying a polymer cladding on narrowed waveguides*. Optics express, 17(17):14627–14633, 2009.

[9] Payam Alipour, Ehsan Shah Hosseini, Ali Asghar Eftekhar, Babak Momeni, and Ali Adibi. *Temperature-insensitive silicon microdisk resonators using polymeric cladding layers*. In 2009 Conference on Lasers and Electro-Optics and 2009 Conference on Quantum electronics and Laser Science Conference, pages 1–2. IEEE, 2009.

[10] Stevan S Djordjevic, Kuanping Shang, Binbin Guan, Stanley TS Cheung, Ling Liao, Juthika Basak, Hai-Feng Liu, and SJB Yoo. *CMOS-compatible, athermal silicon ring modulators clad with titanium dioxide*. Optics Express, 21(12):13958–13968, 2013.

[11] Kuanping Shang, Stevan S Djordjevic, Jun Li, Ling Liao, Juthika Basak, Hai-Feng Liu, and SJB Yoo. *CMOS-compatible titanium dioxide deposition for athermalization of silicon photonic waveguides*. In CLEO: Science and Innovations, pages CF2I–5. Optical Society of America, 2013.

[12] Biswajeet Guha, Bernardo BC Kyotoku, and Michal Lipson. *CMOS-compatible athermal silicon microring resonators*. Optics express, 18(4):3487–3493, 2010.

[13] Sarvagya Dwivedi, Herbert D'heer, and Wim Bogaerts. *A compact all-silicon temperature insensitive filter for WDM and bio-sensing applications*. IEEE Photonics Technology Letters, 25(22):2167–2170, 2013.

[14] Mutsunori Uenuma and Teruaki Motooka. *Temperature-independent silicon waveguide optical filter*. Optics letters, 34(5):599–601, 2009.

[15] Biswajeet Guha, Alexander Gondarenko, and Michal Lipson. *Minimizing temperature sensitivity of silicon Mach-Zehnder interferometers*. Optics express, 18(3):1879–1887, 2010.

[16] Antonio Ribeiro, Sarvagya DwIVEDI, and Wim Bogaerts. *A thermally tunable but athermal silicon MZI filter*. In 18th European Conference on Integrated Optics 2016 (ECIO), 2016.

[17] R Amatya, CW Holzwarth, HI Smith, and RJ Ram. *Efficient thermal tuning for second-order silicon nitride microring resonators*. In 2007 Photonics in Switching, pages 149–150. IEEE, 2007.

[18] Sasikanth Manipatruni, Rajeev K Dokania, Bradley Schmidt, Nicolás Sherwood-Droz, Carl B Poitras, Alyssa B Apsel, and Michal Lipson. *Wide temperature range operation of micrometer-scale silicon electro-optic modulators*. Optics letters, 33(19):2185–2187, 2008.

[19] Michael R Watts, William A Zortman, Douglas C Trotter, Gregory N Nielson, David L Luck, and Ralph W Young. *Adiabatic resonant microrings (ARMs) with directly integrated thermal microphotonics*. In 2009 Conference on Lasers and Electro-Optics and 2009 Conference

on Quantum electronics and Laser Science Conference, pages 1–2. IEEE, 2009.

[20] DDL Wijngaards, SH Kong, M Bartek, and RF Wolffenbuttel. *Design and fabrication of on-chip integrated polySiGe and polySi Peltier devices*. Sensors and Actuators A: Physical, 85(1-3):316–323, 2000.

[21] AW Sloman, Paul Buggs, James Molloy, and Douglas Stewart. *A microcontroller-based driver to stabilize the temperature of an optical stage to within 1 mK in the range, using a Peltier heat pump and a thermistor sensor*. Measurement Science and Technology, 7(11):1653, 1996.

6

Conclusions and Perspectives

6.1 Conclusion

In this thesis, we discussed three topics: a new concept for an on-chip integrated stationary Fourier transform spectrometer (FTS), an on-chip pump rejection filter, and an on-chip temperature-insensitive filter. Firstly, we demonstrated that the proposed on-chip stationary FTS could provide moderately high resolution over a broad wavelength range within a minimal footprint. These characteristics not only make it promising as an integrated FTS but also allow it to be further integrated into various lab-on-a-chip systems. Next, to further pave the way for full integration of on-chip spectroscopic systems, we explored the on-chip pump rejection filter and the on-chip temperature-insensitive filter. The former is of particular interest for on-chip Raman spectroscopy as it has an unlimited free spectral range (FSR) on the long wavelength side of the stop/passband, and could provide an ultra-high extinction ratio. The latter offers temperature-insensitive wavelength reference that helps calibrate the on-chip spectrometer and could be useful for on-chip spectroscopic applications where an absolute determination of optical wavelength is desired. In the following paragraphs, we briefly summarize the conclusions and the achievements obtained during this Ph.D. project.

Firstly, we introduced the principles and provided the design details of the proposed on-chip integrated stationary FTS. There are two different approaches to realize this new type of on-chip FTS, both sharing the same characteristic that the interferogram is generated by two co-propagative waveguide modes with different phase velocities. The underlying principles indicated that the proposed on-chip FTS should enjoy the advantages of having a broad operational bandwidth, a moderately high resolution, and a small footprint. We experimentally characterized the prototype devices fabricated on a silicon nitride (SiN) rib waveguide platform. Considering monochromatic input signals, we demonstrated that our on-chip FTS could reconstruct spectral lines in a wide wavelength range (780-984 nm) with a FWHM down to 2 nm. While a higher resolution could readily be achieved by increasing the length of the device, there are practical limitations to the operational bandwidth set by the dispersive nature of the waveguide modes and the single-mode conditions of the waveguides. We also tested the prototype device with a broadband signal. We were able to reconstruct the spectral peak at the correct center wavelength, although the spectrum has a poor SNR and the spectral peak is broadened noticeably. We carried out investigations and concluded that the problem is that the interferogram recorded with the current prototype devices only included a small portion of the centerburst. In order to obtain better SNR and to avoid broadening, we should make sure that, in future designs, the centerburst of the interferogram is covered as completely as possible in the recording window.

In addition, we reported work on the on-chip pump rejection filter. Based on the grating assisted contra-directional coupler (GACDC), the proposed filter provides an unlimited FSR on the red side of its stop-band. Different from the simple Bragg reflector, the GACDC filter could couple the rejected light into a bus waveguide instead of reflecting it back to the input port. Another essential feature of the on-chip filter is the rejection ratio. Typically, the rejection ratio saturates to around 40 dB for grating-based on-chip filters. We revealed that the primary causes are the random phase errors introduced by fabrication imperfections. This insight had led to the idea of cascading the GACDC filter. By cascading multiple stages, the filtered light could be dropped out in each stage and thus avoid being subject to the scattering induced by the phase defects in previous stages. We fabricated the proposed filters on a SiN rib waveguide platform with e-beam lithography for fast prototyping. Experimentally, we measured an ultra-high extinction ratio of 68.5 dB in the 3 nm wide stop-band centered at the wavelength of 783.6 nm from a 16-stage cascaded GACDC filter with a total filter length of 2000 μm. The extinction ratio is improved by around 30 dB when compared to the less-than-40-dB saturation level measured

from the single stage GACDC filters. In conclusion, while there is still room for improvement, we demonstrated that the on-chip GACDC filters are suitable and promising for pump rejection in applications such as the on-chip Raman spectroscopy.

Finally, we explored the proposed on-chip temperature-insensitive filter that is designed to compensate for the spectral drifts induced by both the thermo-optical effect and the thermal expansion effect. We explained the working principle and demonstrated the various experiments conducted for characterizing the fabricated prototype. In the preliminary experiments, we measured a negative drift rate of more than -100 pm/K. The cause of the unexpected results is the non-optimized mirror position. We realized it is critical to have the mirror in parallel to the photonic chip at the correct height. Therefore, we made a mirror "bridge" of which the standoff has the desired thermal expansion coefficient, and the mirror position is close to optimum. We tried to measure the temperature sensitivity with the improved mirror position. In the experiments, we noticed different temperature sensitivities could be obtained by slightly moving the mirror "bridge". Although with poor reproducibility, the best result we obtained is a drift rate of -4 pm/K. We believe that with some further improvements, the filter should work stably and could be useful for providing an athermal on-chip wavelength reference for on-chip spectroscopic applications.

6.2 Perspectives

While we have demonstrated the promising performance of the proposed on-chip co-propagative stationary FTS, there is still room for further improvement. The current measuring approach enabled by a sophisticated scanning system complicates the operation and makes the measurement time-consuming. In the future, we envisage a fully integrated version where the proposed on-chip FTS could be directly fabricated on a CMOS image sensor wafer so that we could capture the entire interferogram in one snapshot. The co-integration with CMOS image sensors also opens the possibility of massive multiplexing. As each on-chip FTS device exhibits a small footprint that is long and narrow, we could put an array of devices together side by side. As such, we could potentially build a hyperspectral imager with high spectral resolution. In fact, we have made such designs that will be fabricated directly on top of the imager wafer by IMCE. However, due to some internal delays, we won't be able to receive the chip within the time frame of this Ph.D. project. Further work will be contin-

ued by our colleagues in the photonics research group. Besides, we could still improve the performance from the design point of view. Firstly, as already discussed in Chapter 3, to better reconstruct the spectrum for the broadband input signals, we can set an initial phase delay to the light going into the narrow waveguide. To implement this, we could introduce an additional propagation path to the taper that goes to the narrow waveguide. Secondly, as the current operational bandwidth is mainly limited by the dispersive nature of the waveguide modes and the single-mode condition of the waveguides, we should seek for new types of waveguides that have a wider single-mode range and support guided modes with confinement factors that are less wavelength dependent.

The extinction ratio obtained from the cascaded GACDC filter is currently around 68.5 dB. As detailed in chapter 4, to still increase the extinction ratio, we need to clean the reflected light more thoroughly in each stage. For this purpose, on the one hand, we need to optimize the transition taper to suppress the co-directional coupling further; on the other hand, we should replace the standard grating couplers at the drop-ports to the lower reflection ones. Eventually, the limiting factor will be the stray light background set by the light leaked into the slab, traveling around in the chip and being scattered by the neighboring devices or being reflected by the edge of the chip. At this point, we could potentially surround the individual device with on-chip light-absorbing structures or materials in order to approach an even higher extinction ratio.

Also for the on-chip temperature-insensitive filter, further work is needed. Currently, the mirror "bridge" merely rests on the photonic chip without adhesion. This allows us to move it around and to reuse it on different photonic chips. However, this turned out to lead to unreproducible results with respect to temperature sensitivity. In order to increase the reproducibility, one approach is to explore a solution that could more accurately fix the mirror in parallel to the chip at the desired height. It would also be beneficial to build a model that could analyze the non-optimized situation and estimate the tolerable deviations.